Aus der Medizinischen Klinik mit Schwerpunkt Rheumatologie
und Klinische Immunologie der Medizinischen Fakultät
Charité – Universitätsmedizin Berlin

DISSERTATION

Entwicklung neuer Bildgebungsverfahren zur Diagnose von chronisch entzündlichen Erkrankungen im Tiermodell

zur Erlangung des akademischen Grades
Doctor rerum medicinalium (Dr. rer. medic.)

vorgelegt der Medizinischen Fakultät
Charité – Universitätsmedizin Berlin

von

Daniel Bremer

aus Berlin

Datum der Promotion: 07.12.2018

Inhaltsverzeichnis

1 Zusammenfassung **3**

1.1 Abstrakt . . . 3

1.2 Einführung . . . 5

1.3 Methodik . . . 7

1.3.1 Mausmodell der experimentellen autoimmunen Enzephalomyelitis und Uveoretinitis . . . 7

1.3.2 Transgene Reportermausstämme . . . 7

1.3.3 Hirnstamm-Präparation . . . 8

1.3.4 Positionierung der Retina . . . 9

1.3.5 Zwei-Photonen-Mikroskopie . . . 10

1.4 Ergebnisse . . . 11

1.4.1 Immunzellinfiltration in der EAU . . . 11

1.4.2 Gliale Aktivierung und Bewegungsmuster . . . 13

1.4.3 Neuronale Dysfunktion in der EAE und EAU . . . 15

1.5 Diskussion . . . 18

1.6 Literaturverzeichnis . . . 21

2 Eidesstattliche Versicherung **23**

3 Ausgewählte Publikationen **26**

4 Lebenslauf **67**

5 Komplette Publikationsliste **69**

6 Danksagung **71**

1 Zusammenfassung

1.1 Abstrakt

Die Verhinderung von Pathogenesen und Entwicklung gezielter therapeutischer Behandlungsstrategien sind die Hauptziele der modernen Biomedizin. Daher ist es unabdingbar Zell- und Gewebefunktionen im naturgetreuen Kontext, den lebenden Organismus, beobachten zu können. Zu diesem Zweck werden Tiermodelle eingesetzt, die unter anderem verschiedene Aspekte chronisch entzündlicher Erkrankungen des Zentralnervensystems (ZNS) simulieren. Dabei ist der Zugang zum Cortex, Hirnstamm oder Rückenmark meist nur durch invasive und oft terminale Eingriffe möglich, wodurch wiederholte Aufnahmen in einem Individuum in verschiedenen Stadien der Erkrankung nicht möglich sind. Die Retina hingegen ist der einzige Bestandteil des ZNS, welcher durch optische Methoden nichtinvasiv abgebildet werden kann. Dabei können Veränderungen in der Retina auch Prozesse in anderen Regionen des ZNS widerspiegeln und somit indirekt charakterisiert werden. In diesem Sinne ist in dieser Arbeit eine neuartige Methode entwickelt worden, mit dessen Hilfe die Retina von lebenden Mäusen longitudinal untersucht werden kann. Sie basiert auf der Zwei-Photonen-Mikroskopie, wodurch zelluläre Infiltration und Interaktion *in vivo* beobachtet werden können. Erprobt wurde die neue Methode am Mausmodell der experimentellen autoimmunen Uveoretinitis (EAU), bei der autoreaktive T-Zellen die Blut-Retina-Schranke überwinden und eine Gewebeschädigung durch Rekrutierung von weiteren peripheren Leukozyten einleiten. Dabei stellte sich in der vorliegenden Arbeit heraus, dass der Prozess der Retinainfiltration von $CD4^+$ T-Zellen und $LysM^+$ Phagozyten vom Sehnervkopf aus beginnt und sich radial zum äußeren Rand hin ausbreitet. Zudem konnte eine morphologische Veränderung und Ansammlung der $CX3CR1^+$ Mikrogliazellen vor allem an beschädigten Blutgefäßen festgestellt werden. Des Weiteren konnten aktivierte und hochmotile $CX3CR1^+$ Zellen im perivaskulären Raum beobachtet werden. Interessanterweise bewegt sich die Mehrheit dieser Zellen in Mäusen mit EAU in Richtung des Sehnervkopfs, im Gegensatz zu den Zellen in den gesunden Kontrollen. Funktionelle Calciummessungen in der Retina während der EAU zeigen, dass bis zu 28 Tage nach Immunisierung keine signifikant schädigende Erhöhung des intrazellulären Calciums in den Ganglienzellen eintritt. Dank der neu entwickelten Methode können nun immunrelevante Prozesse mit zellulärer Auflösung über den gesamten Krankheitsverlauf chronisch entzündlicher Erkrankungen evaluiert werden.

Abstract

Preventing pathogenesis and developing selective therapeutic strategies are the main goals in modern biomedicine. Therefore, it is absolutely necessary to probe cellular and tissue functions in the living organism. Animal models can be used to study different aspects of chronic inflammatory diseases taking place in the central nervous system (CNS). Imaging the brain stem, spinal cord or cortex needs invasive and often terminal surgery. Thus, longitudinal measurements in one and the same animal at several time points during the whole time course of disease are not possible. The retina is the only part of the CNS that can be imaged non-invasively by optical methods. Changes in the retina may reflect pathogenesis from other parts of the CNS as earlier studies have shown e.g. in patients with multiple sclerosis in which thinning of the retinal nerve fiber layer is one of the first symptoms.

In the here presented work a new method has been developed to observe the retina from living mice longitudinally. The method is based on the two-photon-absorption, thereby near infrared radiation is used to excite fluorescent proteins or dyes. This allows imaging of cellular infiltration, migration and function of fluorescently labelled leukocytes *in vivo*. The new approach was tested in the animal model for experimental autoimmune uveoretinitis (EAU) where T cells overcome the blood-retinal-barrier to inflict retinal inflammation followed by recruitment of peripheral leukocytes that induce tissue damage.

The process of $CD4^+$ T cell infiltration starts from the optic nerve head towards the retinal periphery followed by $LysM^+$ phagocyte infiltration in a radial manner. The $CX3CR1^+$ microglia show a change from a more probing state towards an activated phenotype and accumulate mainly around disrupted blood vessels. A small population of activated and highly motile $CX3CR1^+$ cells could only be observed in the perivasculature. Interestingly, most of this motile cells are moving towards the optic nerve head in mice affected by EAU compared to healthy controls. Unexpectedly, functional calcium measurements during the course of EAU up to 28 days after immunisation showed no significant increase in intracellular calcium levels as an indicator for cellular apoptosis in the ganglion cell layer.

The newly developed approach allows longitudinal retinal imaging of cellular infiltration, migration and function over time repeatedly over the whole course of chronic inflammatory diseases. This method is not only limited to ocular diseases but also can be used to observe indirectly pathogenic processes of the CNS.

1.2 Einführung

Die Retina ist ein Bestandteil des zentralen Nervensystems (ZNS) und kann als solches in Autoimmunerkrankungen schwer geschädigt werden. Das wohl bekannteste Beispiel dafür ist die Multiple Sklerose, bei der eines der ersten klinischen Symptome der vorübergehende Verlust der Sehkraft ist [1–3]. Im Falle der Neuromyelitis Optica kann sich sogar eine dauerhafte Blindheit entwickeln [4, 5]. In beiden Erkrankungen konnte als Ursache der Blindheit mit der optischen Kohärenztomographie eine Abnahme der retinalen Nervenfaserschicht und der Ganglienzellschicht beobachtet werden [6, 7]. Ob aber der Rückgang des neuronalen Gewebes zuschulden einer direkten Immunattacke retinaler Bestandteile oder durch Schädigung des optischen Sehnervs bedingt ist bleibt bisher unklar.
Ein weiteres Beispiel ist die autoimmune Uveitis, bei der autoreaktive T-Zellen die Blut-Retina-Schranke überwinden, die Retina infiltrieren und eine Entzündung auslösen. Dadurch kommt es zur Rekrutierung von peripheren Leukozyten, welche Gewebeschäden insbesondere an den Photorezeptorzellen hervorrufen [8, 9]. Wie aber die genauen Mechanismen und Dynamiken der Immunzellinfiltration und der Funktionsschädigung der neuronalen Retina ablaufen, konnte bisher mangels geeigneter Methoden nicht ausreichend untersucht werden.

Um die Dynamiken von Autoimmunerkrankungen im naturgetreuen Kontext, den lebenden Organismus, erforschen zu können, müssen neuartige Verfahren entwickelt werden, die den Zugriff auf die relevanten Organe von Versuchstieren erlauben. Die Freilegung des ZNS kann meist nur durch aufwändige und invasive Eingriffe realisiert werden, wodurch wiederholte Aufnahmen in einem Individuum zu verschiedenen Stadien der Erkrankung nicht möglich sind. Das Auge hingegen erlaubt, aufgrund seiner lichtsammelnden Eigenschaften und mittels Einsatz optischer Bildgebungsverfahren, einen direkten nichtinvasiven Zugriff auf die Morphologie und Funktion der Retina.
Ziel dieser Arbeit ist es nun ein geeignetes Untersuchungsverfahren zu entwickeln, mit dessen Hilfe Veränderungen in der Retina von Versuchstieren nichtinvasiv untersucht werden können, wodurch wiederholte Aufnahmen in einem Individuum über den gesamten Krankheitsverlauf chronisch entzündlicher Erkrankungen ermöglicht werden. Dafür eignen sich insbesondere Methoden der Fluoreszenzmikroskopie, da hier fluoreszierende Proteine und Farbstoffe die selektive Markierung und Beobachtung von Zellsubgruppen, Antikörpern und Gewebestrukturen im Tiermodell ermöglichen. Einen Spezialfall der Fluoreszenzmikroskopie stellt die Zwei-Photonen-Mikroskopie dar, bei der dreidimensionale Strukturen in Tiefen von

über einem Millimeter punktweise mit nahinfraroter Strahlung abgetastet werden können. Sie erlaubt den einzigartigen Zugriff auf Informationen über zelluläre Dynamiken im lebenden Organismus weit über die Grenzen zellulärer Zusammensetzung und morphologischer Gewebeveränderungen, wie es mit statischer Histologie üblich ist. Bis heute findet diese Technologie vielfältige Anwendung zur Untersuchung grundlegender physiologischer Prozesse und pathologischer Mechanismen in verschiedensten Organen und Krankheitsmodellen [10, 11]. Im Falle der retinalen Bildgebung ist die Zwei-Photonen-Mikroskopie besonders gut geeignet, da hier eine mögliche Aktivierung und Schädigung der Photorezeptoren durch die Anregung mit nahinfraroter Strahlung vermieden und funktionelle Messungen ermöglicht werden können. Zudem bietet das Auge eine hohe Transmission im sichtbaren und nahinfraroten Spektralbereich, wodurch eine effektive Anregung und Detektion von Fluorophoren erlaubt wird.

Ob die neuentwickelte Methode der retinalen Bildgebung in der Lage ist, Veränderungen innerhalb eines Versuchtieres während der verschiedenen Stadien einer autoimmunen Erkrankung festzustellen und zu analysieren, soll anhand eines Mausmodells der experimentellen autoimmunen Uveoretintis (EAU) erprobt werden. In diesem Modell ist die Retina das direkte Ziel einer Immunattacke und somit sehr gut geeignet, um die neue Methode zu evaluieren. In den folgenden Kapiteln werden die wesentlichen Methoden und Ergebnisse der *in vivo* Untersuchungen vorgestellt und diskutiert. Zudem werden ausgewählte Ergebnisse einer bereits erprobten Methode zur Analyse der neuronalen Funktion im Hirnstamm am Mausmodell der experimentellen autoimmunen Enzephalomyelits (EAE) dargestellt und mit den longitudinalen Ergebnissen der EAU verglichen.
Teilergebnisse der vorliegenden Arbeit wurden zur Veröffentlichung angenommen: Acta Neuropathologica 2015 und Frontiers in Immunology 2016.

1.3 Methodik

In diesem Kapitel wird die Induzierung der verwendeten Mausmodelle im Zusammenhang mit den für die Fluoreszenzmikroskopie wichtigen Eigenschaften der Reportermausstämme erläutert. Zudem werden die operativen und die bildgebenden Methoden im Hirnstamm und in der Retina lebender Mäuse erklärt. Die Tierversuche sind durch das zuständige Amt für Tierschutz (G0081/10, G0093/15, LaGeSo – Landesamt für Gesundheit und Soziales) genehmigt und wurden nach aktuellen Bestimmungen durchgeführt.

1.3.1 Mausmodell der experimentellen autoimmunen Enzephalomyelitis und Uveoretinitis

Die Immunisierung der Versuchstiere erfolgt nach den Mausmodellen der experimentellen autoimmunen Enzephalomyelits (EAE) und der experimentellen autoimmunen Uveoretinitis (EAU). Als Zielantigen der Immunantwort in der EAE wird die Aminosäuresequenz 35-55 des Myelin-Oligodendrozyten-Glykoproteins (MOG) verwendet. Die applizierte Dosis beträgt 150 µg pro Versuchstier und wird subkutan in die Schwanzwurzel injiziert. Die genaue physiologische Funktion von MOG ist bisher unbekannt. Man kann aber davon ausgehen, dass MOG_{35-55} die Funktion eines Adhesionsmoleküls in den Myelinscheiden der Neuronen übernimmt [12]. Das MOG_{35-55} ist in Freunds Adjuvans (CFA) gelöst. CFA enthält Paraffinöl und das wärmebehandelte Mykobakterium tuberculosis, wodurch eine verstärkte Immunantwort ausgelöst wird. Das Eindringen der Lymphozyten in das ZNS wird durch den Einsatz von Pertussis Toxin (PTX) ermöglicht. Dieses wird intraperitoneal am Tag der Immunisierung und 48 Stunden später mit einer Dosis von jeweils 200 ng injiziert [13].
Analog zu diesem Verfahren erfolgt die Induzierung der EAU. Lediglich das Zielantigen wird mit 200 – 300 µg der Aminosäuresequenz 1-20 des Interphotorezeptor retinolbindenden Proteins (IRBP) ausgetauscht. IRBP ist ein Transportprotein, welches freies Vitamin A bindet und für den Transport zwischen den Photorezeptorzellen und dem Pigmentepithel der Retina verantwortlich ist [14]. Die Applikation der beiden Tiermodelle unterscheidet sich somit lediglich im Zielprotein.

1.3.2 Transgene Reportermausstämme

Die verwendeten Mausstämme haben zur besseren Vergleichbarkeit alle den gleichen genetischen Hintergrund der Zuchtlinie C57BL/6. Es werden vier verschiedene transgene Maus-

stämme eingesetzt, wodurch die charakteristischen Eigenschaften beider Autoimmunerkrankungen untersucht werden können. Der CD4$^+$eYFP-Mausstamm wird zur Detektion von T-Zellen benutzt, welche mit dem gelb fluoreszierenden Protein eYFP markiert sind [15]. Der CX3CR1$^+$eGFP-Mausstamm enthält das grün fluoreszierende Protein eGFP und wird zur Detektion von Mikrogliazellen, Monozyten und Makrophagen eingesetzt [16].
Der CerTN L15-Mausstamm exprimiert einen Calciumindikator, der auf den Förster-Resonanz-Energietransfer (FRET) basiert. Dieser erlaubt die Messung der Calciumkonzentration in Neuronen und besteht aus zwei Fluorophoren, welche ein Donor- und Akzeptorpaar bilden (Cerulean und Citrine). Je geringer der Abstand zwischen den beiden Fluorophoren, desto höher ist die Wahrscheinlichkeit, dass der angeregte Donor seine Energie an den Akzeptor überträgt. Die Fluorophore sind an Troponin C gebunden, ein Protein das sich bei Anwesenheit von Calciumionen zusammenfaltet. Bei niedrigen Konzentrationen von unter 100 nM dominiert das Signal von Cerulean. Bei höheren Konzentration von Calcium nimmt das Signal von Cerulean ab und das von Citrine zu. Aus den relativen Signalstärken kann somit die relative Calziumkonzentration abgeleitet werden [17]. Die Abklingzeit des TN L15-Konstrukts liegt im Bereich von einigen 100 ms und ist daher nur geeignet, um langanhaltende Veränderungen von intrazellulären Calcium zu messen, wie sie bei der Schädigung oder Dysfunktion von Nervenzellen auftreten [18].
Zusätzlich sind die Tiere des CerTN L15-Mausstamms mit einem weiteren Mausstamm gekreuzt worden, bei dem die LysM$^+$ Zellen das rot fluoreszierenden Protein tdRFP exprimieren. Dadurch können vor allem periphere Phagozyten wie Makrophagen, Monozyten und Granulozyten detektiert werden [19].

1.3.3 Hirnstamm-Präparation

Die Versuchstiere befinden sich während des gesamten Eingriffs in tiefer Inhalationsnarkose unter 2 % Isofluran. Die Tiefe der Narkose wird durch die Messung des CO_2-Gehalts in der Ausatemluft der Maus und durch ein Elektrokardiogramm mittels Ableitung nach Einthoven überwacht. Der Mauskopf wird in einer vornübergebeugten Position gebracht, wodurch ein Spalt zwischen dem ersten Halswirbel und dem Hinterhauptbein des Schädels entsteht. Danach wird die Muskulatur über dem Trapezmuskel vorsichtig beiseite geschoben und die Muskelschicht direkt über der Dura entfernt. Die freigelegte Region wird mit isotonischer Ringerlösung umspült, um Austrocknung und Verunreinigungen zu vermeiden. Nun kann ein

Immersionsobjektiv in die Lösung getaucht und eine geeignete Region mit Hilfe eines Okulars eingestellt werden. Im Anschluss daran wird die Region mit der Zwei-Photonen-Bildgebung aufgenommen (siehe Abschnitt 1.3.5).

1.3.4 Positionierung der Retina

Die longitudinale Bildgebung in der Retina der Maus erfolgt mit Hilfe eines Titanimplantats. Das Implantat kann in eine mechanische Halterung eingespannt werden, welche im Rahmen dieser Arbeit in enger Kooperation mit der Firma Luigs&Neumann GmbH entwickelt worden ist. Die Halterung ist beheizt und in vier Freiheitsgraden motorisiert. Somit kann die gesamte Maus und daher auch das Mausauge relativ zum Mikroskopobjektiv positioniert und über Zeiträume von mehr als 20 Minuten gemessen werden.
Die Befestigung des Implantats erfolgt unter tiefer Narkose durch eine Ketamin-Xylazin-Injektion. Anschließend wird die Haut über der Schädeldecke der Maus zusammen mit dem Pericranium entfernt. Danach wird ein wie in der Zahnmedizin übliches Ätz- und Bondingverfahren eingesetzt (OptiBond FL Primer und Adhesiver, Kerr). Dadurch entsteht eine stabile Oberflächenstruktur, an der das Implantat mittels Zweikomponenten-Zahnzement (Nexus, Kerr) optimal befestigt werden kann. Um das Stressniveau der Tiere möglichst niedrig zu halten und in Bezug auf die Wundheilzeit erfolgt die Immunisierung der Tiere zwei Wochen nach der Operation.

Die Retinae der Tiere werden am Tag 7, 11, 14, 21 und 28 nach der Immunisierung mittels der Zwei-Photonen-Mikroskopie aufgenommen. Während der Messungen befinden sich die Tiere in tiefer Beatmungsnarkose unter 2 % Isofluran. Die Tiere atmen dabei selbstständig. Damit der Laserstrahl auf die Retina fokussiert werden kann, wird vor jeder Messung die Pupille mit einer sterilen Augentropfenlösung (2 % Phenylephrin und 0,4 % Tropicamid) aufgeweitet. Während der Messung muss die Austrocknung des Mausauges vermieden werden, da sich sonst die Augenlinse und die Hornhaut milchig-weiß trüben würden und eine effektive Transmission des Laserstrahls bis zur Retina verhindert werden würde. Dazu wird eine transparente und viskose Augensalbe (Vidisic, Bausch&Lomb) zwischen Hornhaut und Mikroskopobjektiv aufgetragen. Im Anschluss wird das Versuchstier mit der Positioniereinheit so ausgerichtet, dass die Strukturen der Retina in der Fokusebene des Mikroskops liegen.
Um eine gute Vergleichbarkeit und Evaluierung der *in vivo* Messdaten zu gewährleisten, wird immer der gleiche Bildausschnitt mit gleicher Orientierung der Retina zwischen den

einzelnen Messtagen eingestellt. Eine Färbung der Blutgefäße dient dabei als Orientierung und erfolgt durch die intravenöse Injektion von 50 µl FITC-Dextran bzw. Sulforhodamin 101. Die Injektion erfolgt unmittelbar vor jeder Messung.

1.3.5 Zwei-Photonen-Mikroskopie

Die Bildgebung in der Retina und im Hirnstamm von lebenden Mäusen erfolgt mit einem modifizierten Zwei-Photonen-Mikroskop (TriM Scope II, LaVision BioTec GmbH). Dieses besitzt einen Titan-Saphir-Laser (Chameleon Ultra II, Coherent) zur Erzeugung von ultrakurzen Laserpulsen im Femtosekundenbereich. In Kombination mit einem Optisch-Parametrischen-Oszillators können so verschiedenste Fluorophore in einem weiten Spektralbereich von 680 nm bis 1340 nm effektiv angeregt werden [20].
Die Anregung eines fluoreszierenden Moleküls erfolgt durch der nahezu simultanen Absorption zweier Photonen. Dafür sind extrem hohe Leistungsdichten in Raum und Zeit nötig, was nur in der wenigen Mikrometer großen Fokusebene des Mikroskopobjektives erreicht wird. Eine räumliche Darstellung der zu untersuchenden Strukturen wird durch eine Abtastung der Strukturen durch den Laserstrahl mittels zwei beweglichen Galvanospiegeln erreicht. Dabei wird das emittierte Licht der Fluorophore durch dichroitische Spiegel spektral voneinander getrennt und durch Photovervielfacher (PMT) über die Zeit detektiert. Im Anschluss einer jeden Abtastung erstellt der Computer eine zweidimensionale Rekonstruktion der Strukturen aus dem zeitlichen Fluoreszenzsignal [21].
Zur Detektion werden vier Kanäle eingesetzt. Cerulean wird bei 850 nm angeregt und im Spektralbereich von (466±30) nm simultan mit Citrine bei (525±25) nm und (593±20) nm detektiert. Blutgefäße der Retina sind entweder mit Sulforhodamin 101, angeregt bei 900 nm und detektiert bei (593±20) nm oder mit FITC-Dextran, angeregt bei 800 nm und detektiert bei (525±25) nm, markiert. eGFP und eYFP werden bei 900 nm angeregt und bei (525±25) nm detektiert. Das Signal von tdRFP hingegen wird bei 1100 nm angeregt und bei (593±20) nm gemessen.

Für die Hirnstamm-Messungen wird ein kommerzielles 20x-Wasser-Immersionsobjektiv mit einer numerischen Apertur (NA) von 0,95 und einem Arbeitsabstand (AA) von einem Millimeter verwendet. Bei den Retina-Messungen hingegen wurde in Zusammenarbeit mit der Firma LaVision BioTec GmbH ein speziell für die Anwendung im Mausauge entwickeltes 4x-Multi-Immersionsobjektiv mit einer NA von 0,28 und einen Arbeitsabstand von 6 mm

charakterisiert und eingesetzt.

Um eine mögliche Photoschädigung zu vermeiden, wird bei den Hirnstamm-Messungen eine mittlere Laserleistung von maximal 8 mW und bei den Retina-Messungen von 50 mW verwendet. Die höhere mittlere Leistung im Auge ist bedingt durch die geringere NA des Objektives, wodurch eine geringere Leistungsdichte im Fokus erreicht wird. Hinzu kommt ein Vergrößerungseffekt des Fokus entlang der optischen Achse, hervorgerufen durch die optischen Eigenschaften der Mauslinse. Die Messzeit für ein Sichtfeld von 1400 µm×1400 µm und einer digitalen Auflösung von 994 Pixel×994 Pixel beträgt etwa zwei Sekunden. Um Zellbewegungen in den verschiedenen Schichten der Retina beobachten zu können sind 300 µm tiefe Volumen pro Minute über einen Gesamtzeitraum von 20 Minuten aufgenommen worden.

1.4 Ergebnisse

Das folgende Kapitel beschreibt die Messergebnisse der neuentwickelten Messmethode zur longitudinalen Bildgebung der Retina, welche im Rahmen dieser Arbeit entstanden sind. Dazu zählt unter anderem die wiederholten *in vivo* Aufnahmen der Retinae im Mausmodell der EAU am Tag 7, 11, 14, 21 und 28 nach Immunisierung mittels der Zwei-Photonen-Mikroskopie. Zum besseren Vergleich der Ergebnisse der funktionellen Calciummessungen sind die Aufnahmen des Hirnstamms im Mausmodell der EAE zum Zeitpunkt der maximalen klinischen Symptome dargestellt.

1.4.1 Immunzellinfiltration in der EAU

Die Infiltration von peripheren Immunzellen in der Retina kann wiederholt in einem Individuum entlang des gesamten Krankheitsverlaufs der EAU bis zu 28 Tage nach Immunisierung beobachtet werden. Dabei sind die Anzahl der Immunzellen, die Zellbewegungen und deren Positionen mit der Analysesoftware TrackMate von ImageJ ausgewertet worden. In Übereinstimmung mit den funduskopischen Daten nimmt die Anzahl der $CD4^+$ T-Zellen über den Krankheitsverlauf in allen drei immunisierten Versuchstieren des $CD4^+$ Mausstamms zu [22]. Wie auch aus der Literatur bekannt [23] beginnt die Infiltration am Tag 14 nach Immunisierung (siehe Abbildung 1A und 1C) am Sehnervkopf und verteilt sich zu den späteren Zeitpunkten zunehmend in der Peripherie der Retina. Die $CD4^+$ T-Zellen weisen dabei keine gerichtete Bewegung innerhalb des Messzeitfensters von 20 Minuten auf. Die mittlere Geschwindigkeit der $CD4^+$ T-Zellen in der Retina von etwa $0{,}5\,\frac{\mu m}{min}$ (siehe Abbildung 1D) ist

deutlich geringer als die Geschwindigkeit von etwa 6 $\frac{\mu m}{min}$ von CD4$^+$ T-Zellen im Hirnstamm während der EAE [13]. Diese Ergebnisse implizieren, dass der Prozess der CD4$^+$ T-Zell-Infiltration ein stark gerichteter, aber sehr langsamer Prozess ist. Die Zellinfiltrate scheinen nach dem Durchgang durch die Blut-Retina-Schranke direkt am Eintrittsort zu verharren.

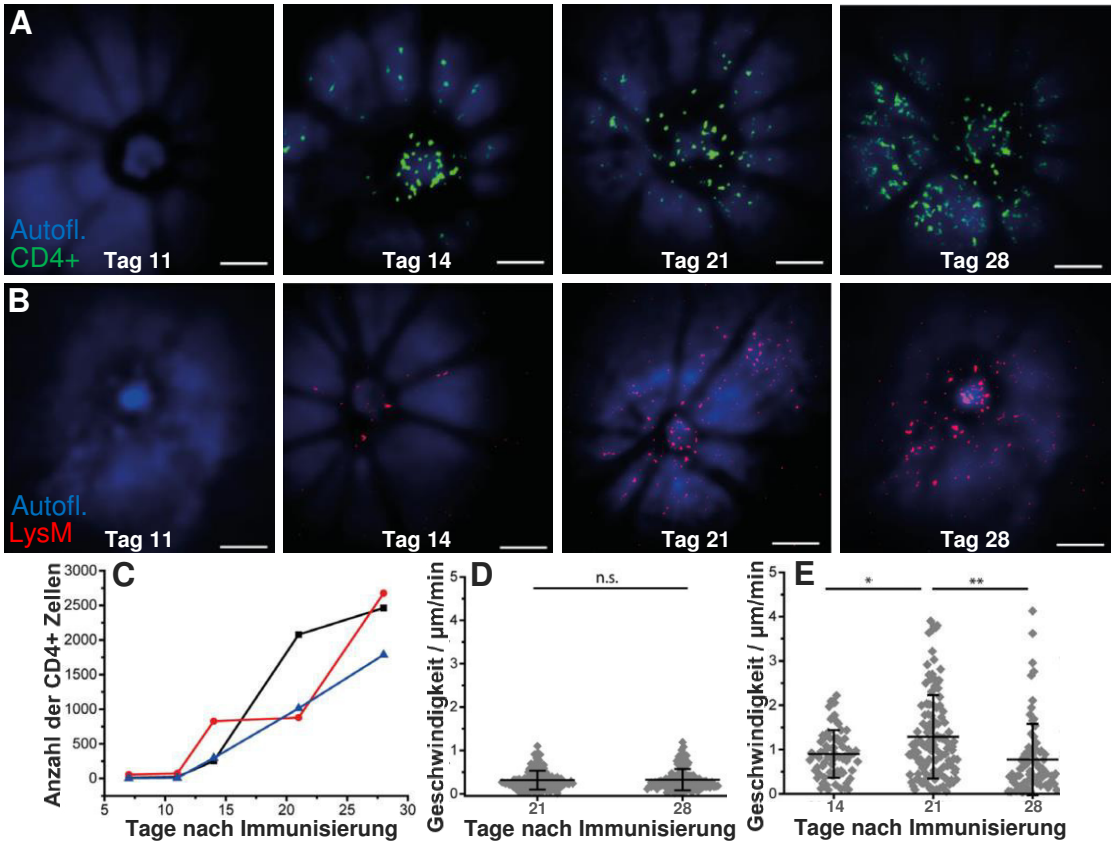

Abbildung 1: **(A, B)** Repräsentative dreidimensionale Projektionen (1400 µm×1400 µm×300 µm) der Retina im Krankheitsverlauf der EAU *in vivo*. Autofluoreszenz entsteht hauptsächlich durch Retinol im Pigmentepithelium. Blutgefäße und Sehnervkopf erscheinen als Schatten. eYFP: $\lambda_{\text{Anregung}} = 900\,\text{nm}$, $\lambda_{\text{Emission}} = (593 \pm 20)\,\text{nm}$, tdRFP: $\lambda_{\text{Anregung}} = 900\,\text{nm}$, $\lambda_{\text{Emission}} = (593 \pm 20)\,\text{nm}$, Autofluoreszenz: $\lambda_{\text{Emission}} = (525 \pm 25)\,\text{nm}$, Maßstab = 200 µm. Infiltration von **(A)** CD4$^+$ T-Zellen und **(B)** LysM$^+$ Phagozyten am Tag 11, 14, 21 und 28 nach Immunisierung. **(C)** Gesamtanzahl der CD4$^+$ T-Zellen pro Maus. Geschwindigkeit der **(D)** CD4$^+$ T-Zellen und **(E)** LysM$^+$ Phagozyten. Statistische Relevanz überprüft mit ANOVA (*$p < 0{,}01$ und **$p < 0{,}001$).

Analoge Messungen sind für vier weitere immunisierte Versuchstiere des LysM$^+$tdRFP-Mausstamms durchgeführt worden. Dabei zeigen die LysM$^+$ Zellen ein ähnliches Muster auf wie die CD4$^+$ T-Zellen. Die LysM$^+$ Zellen dringen am Tag 14 nach Immunisierung am Sehnervkopf und an den größeren venösen Blutgefäßen ein (siehe Abbildung 1B). Die Zellanzahl korreliert mit dem Krankheitsverlauf und steigt mit dem Fortschreiten der Krankheit an.

Verglichen mit späteren Zeitpunkten sind am Tag 14 im Verhältnis zu den $CD4^+$ T-Zellen deutlich weniger $LysM^+$ Zellen in der Retina vorhanden. Dies weist auf einen zeitlich versetzten Eintritt der $LysM^+$ Zellen hin. Somit wird die Hypothese einer T-Zell-initiierten Entzündung im Mausmodell der EAU bestätigt, welche dann in eine Immunantwort mit Infiltration von weiteren peripheren Immunzellen in die Retina übergeht [24]. Die mittlere Geschwindigkeit der $LysM^+$ Zellen beträgt etwa $1\,\frac{\mu m}{min}$ in der Retina und ist am Tag 21 geringfügig höher als am Tag 14 und Tag 28 (siehe Abbildung 1E). Die zurückgelegte Strecke der Zellen ist im Messzeitfenster von 20 Minuten gemessen worden und wurde im Anschluss für alle Zellen pro Messtag vektoriell aufsummiert. Dabei ergibt sich eine Gesamtstrecke von 117 µm am Tag 14 und 147 µm am Tag 21. Es ist somit eine zentrifugale Bewegung der Zellen weg vom Sehnervkopf zu sehen. Am Tag 28 hingegen zeigen die Zellen eine leichte zentripetale Bewegung mit einer Gesamtstrecke von 35 µm zum Sehnerv hin.
Im Gegensatz zum restlichen ZNS-Gewebe sind Signale der Frequenzverdopplung (SHG) von geordneten Kollagenfasern zu keinem Zeitpunkt in der Retina detektierbar. Die Fasern bilden typischerweise Verbindungswege im Gewebe und können als Transportstrukturen für Immunzellen im entzündeten Gehirn dienen [25].

1.4.2 Gliale Aktivierung und Bewegungsmuster

In der Abbildung 2A sind die dreidimensionalen Projektionen der longitudinalen Bildgebung des retinalen Mikroglianetzwerkes repräsentativ für eine gesunde und eine immunisierte Maus dargestellt. Der gesamte Krankheitsverlauf der EAU ist bis zum Tag 28 nach Immunisierung in drei Versuchstieren beobachtet und mit zwei gesunden Kontrollen verglichen worden.
Dabei zeigt sich mit dem Fortschreiten der Symptome eine Veränderung in der Morphology der $CX3CR1^+$ Zellen, von einer überwachenden zu einer phagozytischen Form. Die $CX3CR1^+$ Zellen der gesunden Kontrollen und der immunisierten Tiere am Tag 7 und Tag 11 weisen größtenteils kleine Zellkörper mit fein verzweigten Ausläufern auf. Ab Tag 14 nach Immunisierung hingegen werden amöboide Formen mit verkürzten Fortsätzen sichtbar, welche sich um den Sehnervkopf und teilweise um die Blutgefäße konzentrieren [22]. In den zeitaufgelösten Aufnahmen erkennt man ein Austreten des Farbstoffes aus den Blutgefäßen, was auf eine Störung der Blut-Retina-Schranke in der EAU hinweist. Zudem wird erkennbar, dass der Hauptteil der $CX3CR1^+$ Zellen sich langsam bzw. nahezu gar nicht innerhalb der Retina bewegt (siehe Abbildung 2C). Am Tag 14 nach Immunisierung ist die mittlere

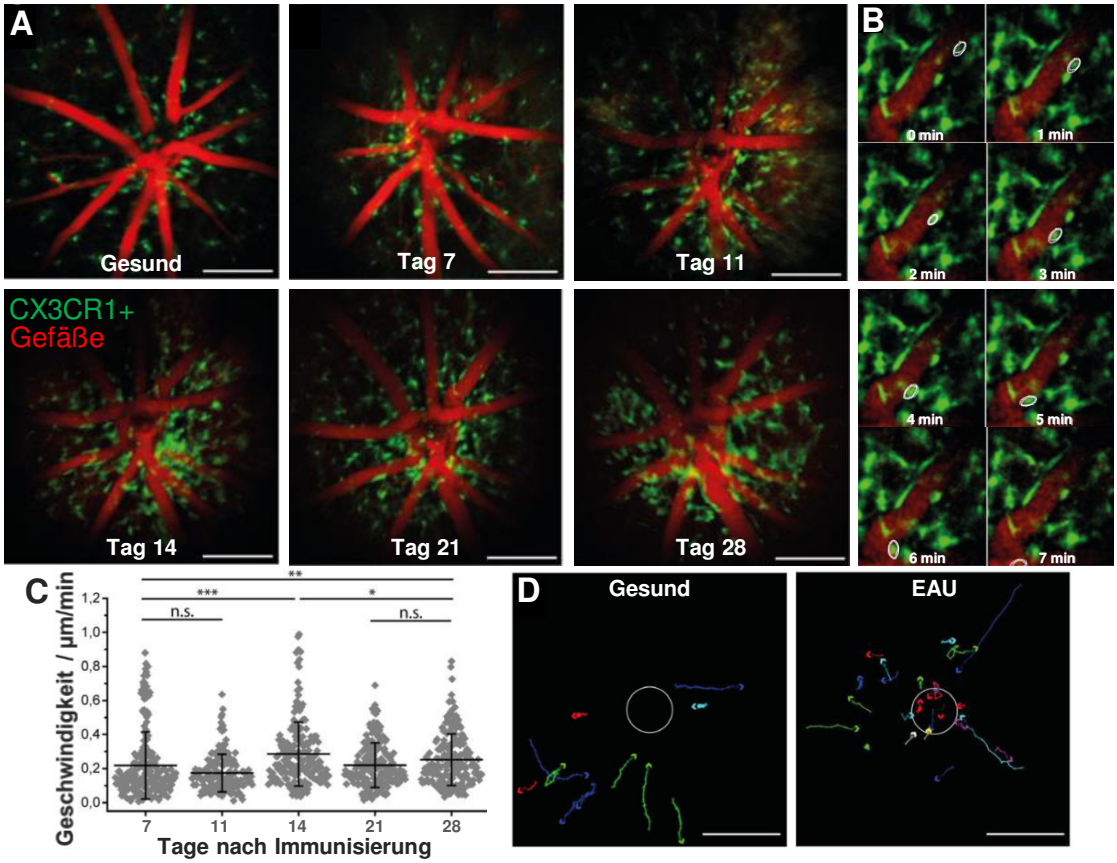

Abbildung 2: **(A)** Repräsentative drei dimensionale Projektion (1400 µm×1400 µm×300 µm) der Retina im Krankheitsverlauf der EAU und einer gesunden Kontrolle *in vivo*. Die Blutgefäße sind mit Sulforhodamin 101 gefärbt. eGFP: $\lambda_{\text{Anregung}} = 900\,\text{nm}$, $\lambda_{\text{Emission}} = (525 \pm 25)\,\text{nm}$, Sulforhodamin: $\lambda_{\text{Anregung}} = 900\,\text{nm}$, $\lambda_{\text{Emission}} = (593 \pm 20)\,\text{nm}$, Maßstab = 300 µm. **(B)** Zeitliche Nahaufnahme einer sich entlang den Blutgefäßen bewegenden CX3CR1$^+$ Zelle mit einer mittleren Geschwindigkeit von 30 $\frac{\mu\text{m}}{\text{min}}$ am Tag 21 nach Immunisierung. **(C)** Mittlere Geschwindigkeit der ruhenden CX3CR1$^+$ Zellen im Verlauf der EAU. Statistische Relevanz überprüft mit ANOVA (*$p < 0{,}1$, **$p < 0{,}01$ und ***$p < 0{,}001$). **(D)** Zurückgelegte Strecken aller sich schneller bewegenden CX3CR1$^+$ Zellen der drei immunisierten Tiere und der zwei gesunden Kontrollen für alle Messzeitpunkte.

Geschwindigkeit mit etwa 0,3 µm am höchsten und nimmt zu späteren Zeitpunkten wieder ab [22].

Ein kleiner Teil der CX3CR1$^+$ Zellen hingegen hat eine signifikant größere Geschwindigkeit. Um die Zellmigration verfolgen zu können, sind die Zellen manuell markiert worden (siehe Abbildung 2B). Sie bewegen sich ausschließlich im perivaskulären Raum entlang der großen Venen mit einer mittleren Geschwindigkeit von (9,6±2,6) $\frac{\mu\text{m}}{\text{min}}$ in den gesunden Kontrollen und mit (10,6±4,8) $\frac{\mu\text{m}}{\text{min}}$ in der EAU. Der zurückgelegte Weg aller markierten Zellen innerhalb der Retina ist in Abbildung 2D für die gesunden und die immunisierten Tiere dargestellt. Der Betrag der Strecken ist mit Bezug zum Sehnervkopf vektoriell aufsummiert worden. Es zeigt

sich, dass in den gesunden Tieren die CX3CR1$^+$ Zellen keine gerichtete Bewegung zum Sehnervkopf ausführen. In den Tieren mit EAU hingegen vollführen die Zellen eine zentripetale Bewegung hin zum Sehnervkopf. Dies suggeriert die Aktivierung einer Subpopulation von CX3CR1$^+$ Zellen in der Retina, welche durch den optischen Sehnerv Zugang zu weiteren Teilen des ZNS erhalten [22].

1.4.3 Neuronale Dysfunktion in der EAE und EAU

In früheren Veröffentlichungen konnte im Hirnstamm von CerTN L15-Mäusen mit EAE gezeigt werden, dass erhöhte Calciumkonzentrationen von mehr als einem Mikromol über einen Zeitraum von einer Stunde ein Indikator für neuronale Dysfunktion ist [13, 18]. In dieser Arbeit werden diese Ergebnisse bestätigt und erweitert, indem gezeigt wird das erhöhtes neuronales und axonales Calcium in Bereichen mit vermehrten Kontakt von LysM$^+$ Immunzellinfiltraten auftritt.

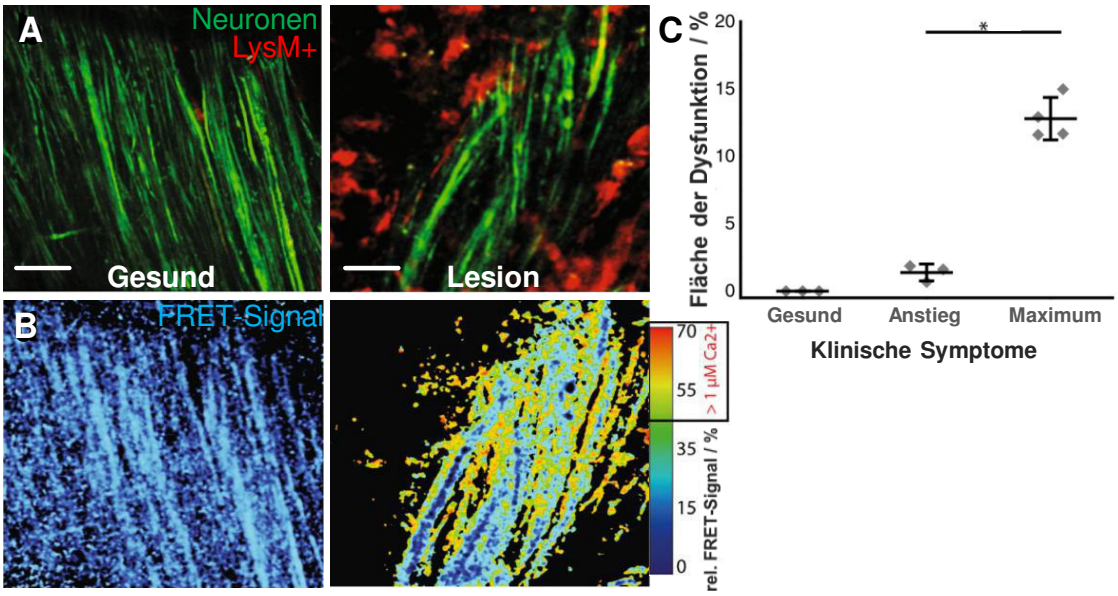

Abbildung 3: Repräsentative zweidimensionale Aufnahme (300 µm×300 µm) des Hirnstamms im Maximum der EAE *in vivo*. **(A)** Intensitätsbilder einer gesunden (links) und einer immunisierten Maus (rechts). Cerulean+Citrine: $\lambda_{Anregung} = 850\,\text{nm}$, $\lambda_{Emission} = (466 \pm 30)\,\text{nm}$, $(525 \pm 25)\,\text{nm}$ und $(593 \pm 20)\,\text{nm}$, tdRFP: $\lambda_{Anregung} = 1100\,\text{nm}$, $\lambda_{Emission} = (593 \pm 20)\,\text{nm}$, Maßstab = 50 µm. Infiltration von LysM$^+$ Zellen im Maximum der EAE. **(B)** Berechnete und anschließend maskierte Darstellung der relativen Calciumkonzentration aus den Intensitätssignalen einer gesunden (links) und einer immunisierten Maus (rechts). **(C)** Gegenüberstellung der Mittelwerte der relativen Calciumkonzentration aus drei bis zwölf akuten Läsionen pro Versuchstier. Der Flächenanteil der erhöhten Calciumkonzentration korreliert mit den klinischen Symptomen der EAE. Statistische Relevanz überprüft mit ANOVA (*$p < 0{,}001$).

Dafür ist der Hirnstamm von drei gesunden und vier mit MOG_{35-55} immunisierten Tieren im Maximum der klinischen EAE-Symptome aufgenommen worden. Die Ergebnisse sind in der Abbildung 3 exemplarisch dargestellt. Die Abbildung 3A zeigt das Intensitätssignal der fluoreszierenden Neuronen und der $LysM^+$ Phagozyten. In der Abbildung 3B sind die daraus berechneten relativen Calciumkonzentrationen dargestellt, wie in Abschnitt 1.3.2 erläutert. Der relative Flächenanteil der neuronalen Dysfunktion ist als Mittelwert von drei bis zwölf akuten Läsionen pro Versuchstier in der Abbildung 3C dargestellt. Man erkennt, dass der Anteil der Dysfunktion mit den klinischen Symptomen in der EAE korreliert und die Läsionen zeitgleich mit den Symptomen auftreten [26].

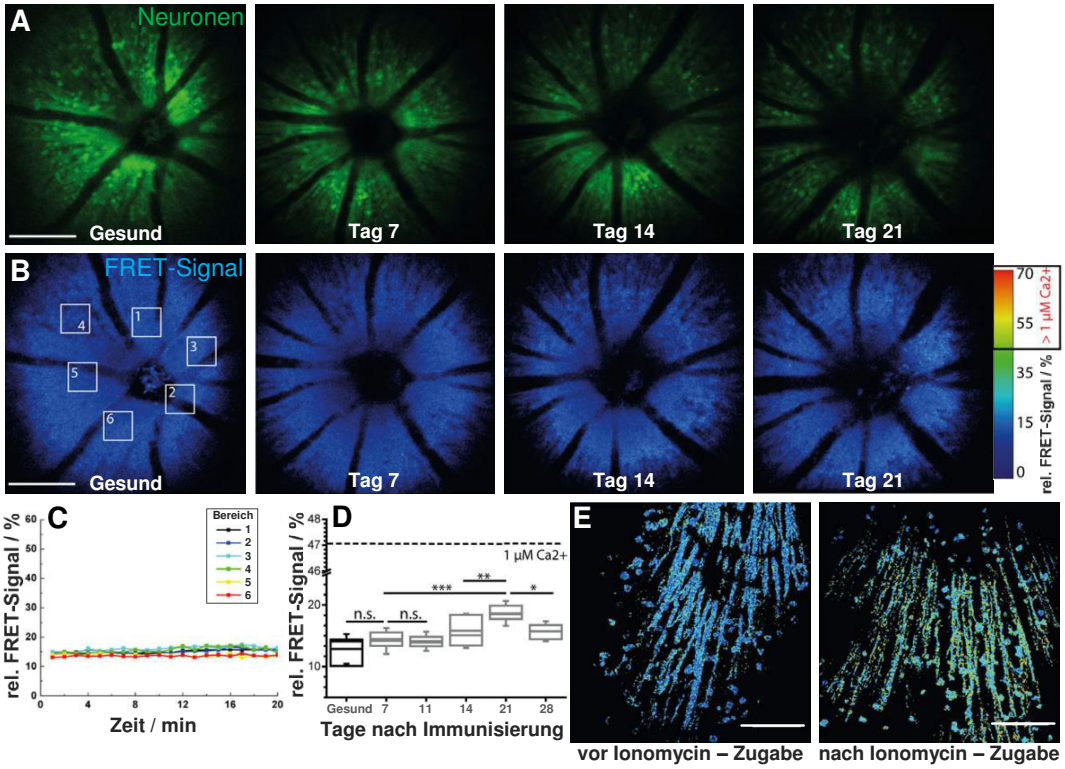

Abbildung 4: Repräsentative drei dimensionale Projektion (1400 µm×1400 µm×300 µm) der Retina im Krankheitsverlauf der EAU. **(A)** Intensitätsbilder des aufsummierten Signals von Cerulean und Citrine in den neuronalen Fasern der Retina. Cerulean+Citrine: $\lambda_{Anregung} = 850\,\text{nm}$, $\lambda_{Emission} = (466 \pm 30)\,\text{nm}$, $(525 \pm 25)\,\text{nm}$ und $(593 \pm 20)\,\text{nm}$, Maßstab = 300 µm. **(B)** Berechnete und anschließend maskierte Darstellung der relativen Calciumkonzentration aus den Intensitätssignalen. **(C)** Das FRET-Signal bleibt über den jeweiligen Messzeitraum von 20 Minuten konstant bei etwa 14 %. **(D)** Zusammenfassung der Mittelwerte der relativen Calciumkonzentration von drei immunisierten und vier gesunden Versuchstieren. Am Tag 21 ist eine Erhöhung der Konzentration messbar, jedoch bleiben alle Werte weit unter dem Grenzwert der neuronalen Dysfunktion von 47 %. Statistische Relevanz überprüft mit ANOVA (*$p < 0{,}05$, **$p < 0{,}01$ und ***$p < 0{,}001$). **(E)** FRET-Signal einer explantierten Retina vor (links) und nach (rechts) Zugabe von 40 µM Ionomycin *in vitro* führt zu einer messbaren Einlagerung von Calciumionen.

Weitere Versuchstiere des CerTN L15-Mausstamms immunisiert mit $IRBP_{1-20}$ sind mit der longitudinalen Bildgebungsmethode wiederholt in der Retina untersucht worden. Die Ergebnisse sind in der Abbildung 4 zusammengestellt. Die erste Reihe zeigt exemplarisch die dreidimensionalen Projektionen der Intensitätssignale der fluoreszierenden Neuronen für eine gesunde und eine immunisierte Maus über den Krankheitsverlauf der EAU. Die zweite Reihe zeigt analog dazu das aus der Intensität berechnete FRET-Signal zur Bestimmung der relativen Calciumkonzentration. Die Retinae sind wiederholt über einen Zeitraum von 20 Minuten pro Messtag aufgenommen worden. Der zeitliche Verlauf der Calciumkonzentration ist für sechs verschiedene Regionen innerhalb der Retina berechnet worden (siehe Abbildung 4C). In allen Bereichen bleibt das Calciumniveau nahezu konstant bei 14 % innerhalb des Messzeitfensters und erhöht sich zu keinem Zeitpunkt während der Messung. Daher wird die Funktionalität der Retina durch die eingesetzte Laserstrahlung nicht beeinflusst.
Insgesamt sind die Aufnahmen von neuronalem Calcium im CerTN L15-Mausstamm in drei mit EAU immunisierten Tieren und vier gesunden Kontrollen durchgeführt worden. Die Mittelwerte der Konzentration für die einzelnen Messzeitpunkte sind in der Abbildung 4D dargestellt. Es zeigt sich eine geringe, aber signifikante Erhöhung in der Calciumkonzentration von 18 % am Tag 21 nach Immunisierung im Vergleich zu früheren Krankheitsstadien. Am Tag 28 nimmt der Wert wieder ab. Davon abgesehen erreichen die Werte der Calciumkonzentration nicht die für eine pathologisch neuronale Dysfunktion typischen Werte von über 47 % entsprechend 1 µM, welche im Hirnstamm von Mäusen mit EAE unter ähnlichen inflammatorischen Bedingungen auftreten [26]. Somit sind die Ganglienzell- und Nervenfaserschicht von der Inflammation im Mausmodell der EAU bis zu 28 Tage nach Immunisierung nicht betroffen und spielen im Mausmodell der EAU eine eher untergeordnete Rolle.
Zudem konnte mit der Hilfe von *in vitro* Untersuchungen von explantierten Retinae im Rahmen dieser Arbeit gezeigt werden, dass Ganglienzellen und deren Axone des CerTN L15-Mausstamms, welche den Thy1-Promoter exprimieren [27] auch das TN L15-Konstrukt verschlüsseln (siehe Abbildung 4E). Zusätzlich ist die Funktionalität des TN L15-Konstrukt in der Retina mittels Applikation von 40 µM Ionomycin überprüft worden. Dabei konnte ein relatives FRET-Signal von bis zu 70 % (entspricht 3 µM neuronales Calcium) in explantierten Retinae von gesunden CerTN L15-Mäusen berechnet werden.

1.5 Diskussion

Neuroinflammatorische Prozesse können im Mensch und Tier von Stunden über mehreren Tagen bis hin Monaten andauern, wobei typische Messzeitfenster in der intravitalen Mikroskopie auf wenige Stunden begrenzt sind. Daher herrscht großer Bedarf an Technologien, welche wiederholte Aufnahmen in ein und demselben Versuchstier erlauben. Das Potential der retinalen Zwei-Photonen-Bildgebung wurde bereits durch frühere Publikationen aufgezeigt [28, 29]. In der vorliegenden Arbeit konnte erstmalig über eine Zeitspanne von bis zu 20 Minuten wiederholt die Dynamik von Zellen, die Infiltration ins Gewebe und Gewebefunktionen in einem Versuchstier über einen Zeitraum von 28 Tagen aufgenommen werden. Erstmals können so, durch eine kombinierte morphologische und funktionelle Bildgebung, in Zukunft neuroprotektive Therapien auf ihre Effektivität hin *in vivo* untersucht werden. Zudem erlaubt die nicht-invasive retinale Bildgebung die Reduzierung der benötigten Versuchstieranzahl ganz nach dem 3V-Prinzip von Russell und Burch, Vermeidung, Verringerung und Verfeinerung. Trotz kleiner Versuchstiergruppen können statistisch relevante Aussagen weiterhin getroffen werden, da die Varianz in der individuellen Immunantworten zwischen den einzelnen Tieren direkt berücksichtigt werden kann.

Im Mausmodell der EAU konnte wie auch in früheren Veröffentlichungen bestätigt werden, dass die $CD4^+$ T-Zellen vor den $LysM^+$ Zellen die Retina infiltrieren und die Inflammationskaskade auslösen. Neben der Infiltration durch die beschädigte Blut-Retina-Schranke beginnt sie typischerweise am Sehnervkopf, was ein Indiz für eine mögliche Zellmigration von inneren Teilen des ZNS über den Sehnerv darstellt. Interessanterweise sind die $CD4^+$ T-Zellen über den gesamten Verlauf der EAU deutlich langsamer als die $LysM^+$ Zellen. Berücksichtigt man das Fehlen von geordneten Kollagenfasern in der entzündeten Retina, dann scheint die Bewegung von $CD4^+$ T-Zellen stärker als die $LysM^+$ Zellen vom Fehlen der Kollagenfasern in der entzündeten Retina betroffen zu sein.
Unter vergleichbaren inflammatorischen Bedingungen konnten starke Unterschiede im Verhalten von $CD4^+$ T-Zellen und $LysM^+$ Phagozyten im Auge und im Hirnstamm festgestellt werden. Im Hirnstamm und Rückenmark bewegen sich die Effektorzellen kommend aus der Peripherie gerichtet und eher schnell mit $5\,\frac{\mu m}{min}$, besonders entlang neugebildeter Kollagenfasern ähnlich wie die Bewegung innerhalb sekundärer lymphatischer Organe [25]. Sie infiltrieren das in bestimmter Hinsicht immunpriviligierte Hirngewebe durch die Blut-Hirn- oder Blut-Liquor-Schranke und sammeln sich in den Läsionen [13, 25]. Im Auge zeigen

diese Zellen eine reduzierte Geschwindigkeit von etwa 1 $\frac{\mu m}{min}$. Innerhalb von Tagen zu Wochen bewegen sie sich stark gerichtet vom Sehnervkopf ausgehend zum äußeren Rand der Retina. In Übereinstimmung mit diesen Beobachtungen konnten Kollagenfasern zu keinem Zeitpunkt detektiert werden, obwohl frühere Veröffentlichungen zeigten, dass im ZNS und in lymphatischen Organen Kollagenfasern für eine gerichtete Bewegungen benötigt werden [25]. Welche Rolle andere Zellpopulationen, Zelllinien und Botenstoffe wie zum Beispiel CD8-Zellen, Th17-Zellen, CXCL12, GM-CSF oder TNF-α bei der Induktion der Autoimmunität und Interaktion mit retinalem Gewebe haben, bleiben offene Fragen, welche noch in Zukunft beantwortet werden müssen.

Hinsichtlich pathologischer Veränderungen konnte in der Retina während neuronaler Inflammation eine Veränderung des mikroglialen Netzwerkes von einer überwachenden zu einer phagozytischen Form nachgewiesen werden, ähnlich den Anzeichen einer Gliose im Hirnstamm und im Rückenmark früherer Veröffentlichungen [30]. Wahrscheinlich wegen fehlender Leitbahnen im retinalen Parenchym bewegen sich die phagozytischen CX3CR1$^+$ Zellen nur entlang des perivaskulären Raums im entzündeten Auge, was im Kontrast zu früheren Ergebnissen im Gehirn unter ähnlichen inflammatorischen Bedingungen steht. Welche Faktoren für die Bildung oder Blockade von Leitbahnen für Immunzellen in der Retina und im ZNS verantwortlich sind ist bisher noch unbekannt. Interessanterweise bewegen sich mehr CX3CR1$^+$ Zellen perivaskulär in Richtung des Sehnervkopfs während der Inflammation als in der gesunden Retina. Dies impliziert, dass Zellimmigration im Auge während einer neuronalen Inflammation ausgelöst wird und die Zellen über den Sehnervkopf auch in weitere Regionen des ZNS einwandern können. Somit scheint der Sehnerv als schnelle bidirektionale Leitbahn für Immunzellen zu fungieren.

Abgesehen von der starken Immunzellinfiltration und der Veränderung des mikroglialen Netzwerkes erreicht der Anstieg des neuronalen Calciums in der Retina von Mäusen mit EAU nicht das typische Niveau einer neuronalen Dysfunktion. Verglichen mit dem Hirnstamm von Mäusen mit EAE unter qualitativ ähnlichen Bedingungen einer stark dynamischen peripheren Immunzellinfiltration und Gliose wird eine neuronale Schädigung und letztendlich der programmierte Zelltod bereits in frühen Phasen der EAE erreicht [26, 30, 31]. Man kann natürlich nicht ausschließen, dass sich eine neuronale Dysfunktion unabhängig von der intrazellulären Calciumkonzentration entwickelt hat, was durch den CerTN L15-Reportermausstamm nicht nachgewiesen werden kann. Weitere wiederholte Aufnahmen mit

der retinalen Bildgebung in der chronischen Phase der EAU zwischen Tag 28 und 60 nach Immunisierung könnten mögliche Effekte einer verspäteten Apoptose der neuronalen Retina aufdecken. Dabei sollte berücksichtigt werden, dass nicht alle neuronalen Zellen in der Retina den Calciumsensor exprimieren, sondern hauptsächlich nur die Ganglienzellen und deren Axone [22]. Zudem ist das Ausmaß der neuronalen Schädigung zu inneren Bestandteilen des zentralen Nervensystems im Mausmodell der EAU unklar.

Die EAE ist das am häufigsten verwendete Mausmodell der MS, jedoch wird dieses meist nur akut untersucht und eine chronische Diskussion entfällt. Reversible und irreversible pathogene Effekte der T-Zellen, Makrophagen, aktivierten Mikroglia und aktivierten Astrozyten auf die neuronale Funktion in der Retina sind bisher nur wenig untersucht worden und ungewiss. Wenn die im Auge gezeigten Effekte weiter bestätigt werden können, bietet die hier vorgestellte nichtinvasive Bildgebung eine Möglichkeit therapeutische Behandlungsansätze der chronischen Neuroinflammation mit zellulärer Auflösung in einem Individuum zu erproben. Einerseits wird dieser Ansatz zu einem besseren Verständnis relevanter Pathomechanismen führen und andererseits zu einer drastischen Reduzierung benötigter Versuchstierzahlen.
Die neue retinale Bildgebungsmethode erlaubt nicht nur vielversprechende neue Ansätze in entzündlichen Erkrankungen, sondern auch in neurodegenerativen Erkrankungen und bietet darüber hinaus das Potential zur Frühdiagnose, bevor klinische Symptome sichtbar werden. Die retinale Pathogenese wurde kürzlich auch im Zusammenhang mit primär neurodegenerativen Erkrankungen wie Morbus Alzheimer, Morbus Parkinson und der amyotrophen Lateralsklerose gebracht [32, 33]. Des Weiteren könnten auch neue Erkenntnisse im Bereich vaskulärer Erkrankungen wie Diabetes Typ I gewonnen werden, bei denen es zu Veränderungen in den retinalen Blutgefäßen einschließlich Venen, Arterien und Kapillaren kommt [34, 35]. Auch bezüglich entzündlicher Erkrankungen wurde kürzlich in einem transgenen Tiermodell der EAU die Bildung von tertiären lymphatischen Organen in der Retina entdeckt [9]. All diese Beispiele zeigen über die konkreten Ergebnisse der vorliegenden Arbeit hinaus das Potential für die vorgestellte longitudinale Bildgebung, um Fragen aus der Grundlagen- und Therapieforschung in einem weiten biomedizinischen Gebiet beantworten zu können.

1.6 Literaturverzeichnis

[1] Chen, L. and Gordon, L. K. (2005) *Ocular manifestations of multiple sclerosis* In Current Opinion in Ophthalmology volume 16(5) pp. 315–320 Ovid Technologies (Wolters Kluwer Health).

[2] Pérez-Rico, C., Ayuso-Peralta, L., Rubio-Pérez, L., Roldán-Díaz, I., Arévalo-Serrano, J., Jiménez-Jurado, D., and Blanco, R. (2014) *Evaluation of Visual Structural and Functional Factors That Predict the Development of Multiple Sclerosis in Clinically Isolated Syndrome Patients* In Investigative Ophthalmology & Visual Science volume 55(10) p. 6127 Association for Research in Vision and Ophthalmology (ARVO).

[3] Sinnecker, T., Oberwahrenbrock, T., Metz, I., Zimmermann, H., Pfueller, C. F., Harms, L., Ruprecht, K., Ramien, C., Hahn, K., Brück, W., Niendorf, T., Paul, F., Brandt, A. U., Dörr, J., and Wuerfel, J. (2014) *Optic radiation damage in multiple sclerosis is associated with visual dysfunction and retinal thinning – an ultrahigh-field MR pilot study* In European Radiology volume 25(1) pp. 122–131 Springer Nature.

[4] Jarius, S., Wildemann, B., and Paul, F. (2014) *Neuromyelitis optica: clinical features, immunopathogenesis and treatment* In Clinical & Experimental Immunology volume 176(2) pp. 149–164 Wiley-Blackwell.

[5] Schneider, E., Zimmermann, H., Oberwahrenbrock, T., Kaufhold, F., Kadas, E. M., Petzold, A., Bilger, F., Borisow, N., Jarius, S., Wildemann, B., Ruprecht, K., Brandt, A. U., and Paul, F. (2013) *Optical Coherence Tomography Reveals Distinct Patterns of Retinal Damage in Neuromyelitis Optica and Multiple Sclerosis* In Ralf Andreas Linker, (ed.), PLoS ONE volume 8(6), p. e66151 Public Library of Science (PLoS).

[6] Bock, M., Brandt, A. U., Kuchenbecker, J., Dörr, J., Pfueller, C. F., Weinges-Evers, N., Gaede, G., Zimmermann, H., Bellmann-Strobl, J., Ohlraun, S., Zipp, F., and Paul, F. (2011) *Impairment of contrast visual acuity as a functional correlate of retinal nerve fibre layer thinning and total macular volume reduction in multiple sclerosis* In British Journal of Opthalmology volume 96(1) pp. 62–67 BMJ.

[7] Bennett, J., deSeze, J., Lana-Peixoto, M., Palace, J., Waldman, A., Schippling, S., Tenembaum, S., Banwell, B., Greenberg, B., Levy, M., Fujihara, K., Chan, K., Kim, H., Asgari, N., Sato, D., Saiz, A., Wuerfel, J., Zimmermann, H., Green, A., Villoslada, P., and and, F. P. (2015) *Neuromyelitis optica and multiple sclerosis: Seeing differences through optical coherence tomography* In Multiple Sclerosis Journal volume 21(6) pp. 678–688 SAGE Publications.

[8] Chen, X., Kezic, J. M., Forrester, J. V., Goldberg, G. L., Wicks, I. P., Bernard, C. C., and McMenamin, P. G. (2015) *In vivo multi-modal imaging of experimental autoimmune uveoretinitis in transgenic reporter mice reveals the dynamic nature of inflammatory changes during disease progression* In Journal of Neuroinflammation volume 12(1) p. 17 Springer Nature.

[9] Kielczewski, J. L., Horai, R., Jittayasothorn, Y., Chan, C.-C., and Caspi, R. R. dec 2015 *Tertiary Lymphoid Tissue Forms in Retinas of Mice with Spontaneous Autoimmune Uveitis and Has Consequences on Visual Function* In The Journal of Immunology volume 196(3) pp. 1013–1025 The American Association of Immunologists.

[10] Friedl, P. and Gilmour, D. (2009) *Collective cell migration in morphogenesis, regeneration and cancer* In Nature Reviews Molecular Cell Biology volume 10(7) pp. 445–457 Springer Nature.

[11] Matheu, M. P., Othy, S., Greenberg, M. L., Dong, T. X., Schuijs, M., Deswarte, K., Hammad, H., Lambrecht, B. N., Parker, I., and Cahalan, M. D. (2015) *Imaging regulatory T cell dynamics and CTLA4-mediated suppression of T cell priming* In Nature Communications volume 6 p. 6219 Springer Nature.

[12] Roth, M.-P., Malfroy, L., Offer, C., Sevin, J., Enault, G., Borot, N., Pontarotti, P., and Coppin, H. (1995) *The Human Myelin Oligodendrocyte Glycoprotein (MOG) Gene: Complete Nucleotide Sequence and Structural Characterization* In Genomics volume 28(2) pp. 241–250 Elsevier BV.

[13] Siffrin, V., Radbruch, H., Glumm, R., Niesner, R., Paterka, M., Herz, J., Leuenberger, T., Lehmann, S. M., Luenstedt, S., Rinnenthal, J. L., Laube, G., Luche, H., Lehnardt, S., Fehling, H.-J., Griesbeck, O., and Zipp, F. (2010) *In Vivo Imaging of Partially Reversible Th17 Cell-Induced Neuronal Dysfunction in the Course of Encephalomyelitis* In Immunity volume 33(3) pp. 424–436 Elsevier BV.

[14] Agarwal, R. K., Silver, P. B., and Caspi, R. R. (2012) *Rodent Models of Experimental Autoimmune Uveitis* In Methods in Molecular Biology pp. 443–469 Springer Nature.

[15] Srinivas, S., Watanabe, T., Lin, C.-S., William, C. M., Tanabe, Y., Jessell, T. M., and Costantini, F. (2001) *Cre reporter strains produced by targeted insertion of EYFP and ECFP into the ROSA26 locus* In BMC Developmental Biology volume 1 p. 4 Springer Nature.

[16] Jung, S., Aliberti, J., Graemmel, P., Sunshine, M. J., Kreutzberg, G. W., Sher, A., and Littman, D. R. (2000) *Analysis of Fractalkine Receptor CX3CR1 Function by Targeted Deletion and Green Fluorescent Protein Reporter Gene Insertion* In Molecular and Cellular Biology volume 20(11) pp. 4106–4114 American Society for Microbiology.

[17] Heim, N., Garaschuk, O., Friedrich, M. W., Mank, M., Milos, R. I., Kovalchuk, Y., Konnerth, A., and Griesbeck, O. (2007) *Improved calcium imaging in transgenic mice expressing a troponin C–based biosensor* In Nature Methods volume 4(2) pp. 127–129 Springer Nature.

[18] Rinnenthal, J. L., Börnchen, C., Radbruch, H., Andresen, V., Mossakowski, A., Siffrin, V., Seelemann, T., Spiecker, H., Moll, I., Herz, J., Hauser, A. E., Zipp, F., Behne, M. J., and Niesner, R. (2013) *Parallelized TCSPC for Dynamic Intravital Fluorescence Lifetime Imaging: Quantifying Neuronal Dysfunction in Neuroinflammation* In PLoS ONE volume 8(4) p. e60100 Public Library of Science (PLoS).

[19] Clausen, B., Burkhardt, C., Reith, W., Renkawitz, R., and Förster, I. (1999) *Conditional gene targeting in macrophages and granulocytes using LysMcre mice* In Transgenic Research volume 8(4) pp. 265–277 Springer Nature.

[20] Coherent Inc. https://cohrcdn.azureedge.net/assets/pdf/Femtosecond_lasers_for_life_science.pdf *Femtosecond Lasers for Life Sciences* 02 2017.

[21] Lakowicz, J. R. (1983) *Principles of Fluorescence Spectroscopy* Springer Nature.

[22] Bremer, D., Pache, F., Günther, R., Hornow, J., Andresen, V., Leben, R., Mothes, R., Zimmermann, H., Brandt, A. U., Paul, F., Hauser, A. E., Radbruch, H., and Niesner, R. (2016) *Longitudinal Intravital Imaging of the Retina Reveals Long-term Dynamics of Immune Infiltration and Its Effects on the Glial Network in Experimental Autoimmune Uveoretinitis, without Evident Signs of Neuronal Dysfunction in the Ganglion Cell Layer* In Frontiers in Immunology volume 7 Frontiers Media SA.

[23] Chen, J., Qian, H., Horai, R., Chan, C.-C., Falick, Y., and Caspi, R. R. aug 2013 *Comparative Analysis of Induced vs. Spontaneous Models of Autoimmune Uveitis Targeting the Interphotoreceptor Retinoid Binding Protein* In James T. Rosenbaum, (ed.), PLoS ONE volume 8(8), p. e72161 Public Library of Science (PLoS).

[24] Caspi, R. R. mar 2011 *Understanding Autoimmune Uveitis through Animal Models The Friedenwald Lecture* In Investigative Ophthalmology & Visual Science volume 52(3) p. 1873 Association for Research in Vision and Ophthalmology (ARVO).

[25] Herz, J., Paterka, M., Niesner, R. A., Brandt, A. U., Siffrin, V., Leuenberger, T., Birkenstock, J., Mossakowski, A., Glumm, R., Zipp, F., and Radbruch, H. (2011) *In vivo imaging of lymphocytes in the CNS reveals different behaviour of naïve T cells in health and autoimmunity* In Journal of Neuroinflammation volume 8(1) p. 131 Springer Nature.

[26] Mossakowski, A. A., Pohlan, J., Bremer, D., Lindquist, R., Millward, J. M., Bock, M., Pollok, K., Mothes, R., Viohl, L., Radbruch, M., Gerhard, J., Bellmann-Strobl, J., Behrens, J., Infante-Duarte, C., Mähler, A., Boschmann, M., Rinnenthal, J. L., Füchtemeier, M., Herz, J., Pache, F. C., Bardua, M., Priller, J., Hauser, A. E., Paul, F., Niesner, R., and Radbruch, H. (2015) *Tracking CNS and systemic sources of oxidative stress during the course of chronic neuroinflammation* In Acta Neuropathologica volume 130(6) pp. 799–814 Springer Nature.

[27] Thyagarajan, S., vanWyk, M., Lehmann, K., Lowel, S., Feng, G., and Wassle, H. (2010) *Visual Function in Mice with Photoreceptor Degeneration and Transgenic Expression of Channelrhodopsin 2 in Ganglion Cells* In JNeurosci volume 30(26) pp. 8745–8758 Society for Neuroscience.

[28] Palczewska, G., Dong, Z., Golczak, M., Hunter, J. J., Williams, D. R., Alexander, N. S., and Palczewski, K. (2014) *Noninvasive two-photon microscopy imaging of mouse retina and retinal pigment epithelium through the pupil of the eye* In Nature Medicine volume 20(7) pp. 785–789 Springer Nature.

[29] Stremplewski, P., Komar, K., Palczewski, K., Wojtkowski, M., and Palczewska, G. (2015) *Periscope for noninvasive two-photon imaging of murine retina in vivo* In Biomedical Optics Express volume 6(9) p. 3352 The Optical Society.

[30] Radbruch, H., Bremer, D., Guenther, R., Cseresnyes, Z., Lindquist, R., Hauser, A. E., and Niesner, R. (2016) *Ongoing Oxidative Stress Causes Subclinical Neuronal Dysfunction in the Recovery Phase of EAE* In Frontiers in Immunology volume 7 Frontiers Media SA.

[31] Breckwoldt, M. O., Pfister, F. M. J., Bradley, P. M., Marinković, P., Williams, P. R., Brill, M. S., Plomer, B., Schmalz, A., Clair, D. K. S., Naumann, R., Griesbeck, O., Schwarzländer, M., Godinho, L., Bareyre, F. M., Dick, T. P., Kerschensteiner, M., and Misgeld, T. (2014) *Multiparametric optical analysis of mitochondrial redox signals during neuronal physiology and pathology in vivo* In Nature Medicine volume 20(5) pp. 555–560 Springer Nature.

[32] Madeira, M. H., Ambrósio, A. F., and Santiago, A. R. oct 2015 *Glia-Mediated Retinal Neuroinflammation as a Biomarker in Alzheimer's Disease* In Ophthalmic Research volume 54(4) pp. 204–211 S. Karger AG.

[33] Roth, N. M., Saidha, S., Zimmermann, H., Brandt, A. U., Oberwahrenbrock, T., Maragakis, N. J., Tumani, H., Ludolph, A. C., Meyer, T., Calabresi, P. A., and Paul, F. (2013) *Optical coherence tomography does not support optic nerve involvement in amyotrophic lateral sclerosis* In european journal of neurology volume 20(8) pp. 1170–1176 Wiley-Blackwell.

[34] Sohn, E. H., vanDijk, H. W., Jiao, C., Kok, P. H. B., Jeong, W., Demirkaya, N., Garmager, A., Wit, F., Kucukevcilioglu, M., vanVelthoven, M. E. J., DeVries, J. H., Mullins, R. F., Kuehn, M. H., Schlingemann, R. O., Sonka, M., Verbraak, F. D., and Abràmoff, M. D. (2016) *Retinal neurodegeneration may precede microvascular changes characteristic of diabetic retinopathy in diabetes mellitus* In Medical Sciences volume 113(19) pp. E2655–E2664 Proceedings of the National Academy of Sciences.

[35] Albrecht, P., Blasberg, C., Lukas, S., Ringelstein, M., Müller, A.-K., Harmel, J., Kadas, E.-M., Finis, D., Guthoff, R., Aktas, O., Hartung, H.-P., Paul, F., Brandt, A. U., Berlit, P., Methner, A., and Kraemer, M. jul 2015 *Retinal pathology in idiopathic moyamoya angiopathy detected by optical coherence tomography* In American Academy of Neurology volume 85(6) pp. 521–527 Ovid Technologies (Wolters Kluwer Health).

2 Eidesstattliche Versicherung

„Ich, Daniel Bremer, versichere an Eides statt durch meine eigenhändige Unterschrift, dass ich die vorgelegte Dissertation mit dem Thema: Entwicklung neuer Bildgebungsverfahren zur Diagnose von chronisch entzündlichen Erkrankungen im Tiermodell selbstständig und ohne nicht offengelegte Hilfe Dritter verfasst und keine anderen als die angegebenen Quellen und Hilfsmittel genutzt habe.

Alle Stellen, die wörtlich oder dem Sinne nach auf Publikationen oder Vorträgen anderer Autoren beruhen, sind als solche in korrekter Zitierung (siehe „Uniform Requirements for Manuscripts (URM) "des ICMJE -*www.**icmje**.org*) kenntlich gemacht. Die Abschnitte zu Methodik (insbesondere praktische Arbeiten, Laborbestimmungen, statistische Aufarbeitung) und Resultaten (insbesondere Abbildungen, Graphiken und Tabellen) entsprechen den URM (s.o) und werden von mir verantwortet.

Meine Anteile an den ausgewählten Publikationen entsprechen denen, die in der untenstehenden gemeinsamen Erklärung mit der Betreuerin, angegeben sind. Sämtliche Publikationen, die aus dieser Dissertation hervorgegangen sind und bei denen ich Autor bin, entsprechen den URM (s.o) und werden von mir verantwortet.

Die Bedeutung dieser eidesstattlichen Versicherung und die strafrechtlichen Folgen einer unwahren eidesstattlichen Versicherung (§156,161 des Strafgesetzbuches) sind mir bekannt und bewusst."

Datum

Unterschrift

Anteilserklärung an den erfolgten Publikationen

Daniel Bremer hatte folgenden Anteil an den folgenden Publikationen:

Publikation 1: **Tracking CNS and systemic sources of oxidative stress during the course of chronic neuroinflammation**
Agata A. Mossakowski, Julian Pohlan, **Daniel Bremer**, Randall Lindquist, Jason M. Millward, Markus Bock, Karolin Pollok, Ronja Mothes, Leonard Viohl, Moritz Radbruch, Jenny Gerhard, Judith Bellmann-Strobl, Janina Behrens, Carmen Infante-Duarte, Anja Mähler, Michael Boschmann, Jan Leo Rinnenthal, Martina Füchtemeier, Josephine Herz, Florence C. Pache, Markus Bardua, Josef Priller, Anja E. Hauser, Friedemann Paul, Raluca Niesner, Helena Radbruch
Acta Neuropathologica, 2015
Beitrag im Einzelnen: Erhebung der Primärdaten (Fluoreszenzlebensdauermessungen in isolierten Zellpopulationen), Aufbereitung der Daten

Publikation 2: **Ongoing Oxidative Stress Causes Subclinical Neuronal Dysfunction in the Recovery Phase of EAE**
Helena Radbruch, **Daniel Bremer**, Robert Guenther, Zoltan Cseresnyes, Randall Lindquist, Anja E. Hauser, Raluca Niesner
Frontiers in Immunology, 2016
Beitrag im Einzelnen: Erhebung der Primärdaten (Fluoreszenzlebensdauermessungen im Hirnstamm), Auswertung der Daten, Weiterentwicklung der Auswertungssoftware, Beteiligung an der Verfassung des Manuskripts

Publikation 3: **Longitudinal Intravital Imaging of the Retina Reveals Long-term Dynamics of Immune Infiltration and Its Effcts in the Glial Network in Experimental Autoimmune Uveoretinitis, without Evident Signs of Neuronal Dysfunction in the Ganglion Cell Layer**
Daniel Bremer, Florence Pache, Robert Günther, Jürgen Hornow, Volker Andresen, Ruth Leben, Ronja Mothes, Hanna Zimmermann, Alexander U. Brandt, Friedemann Paul, Anja E. Hauser, Helena Radbruch and Raluca Niesner
Frontiers in Immunology, 2016
Beitrag im Einzelnen: Erhebung der Primärdaten (Longitudinale Bildgebung mittels Zwei-Photonen-Mikroskopie, Funduskopie, Histologische Untersuchungen und Färbungen), Aus-

wertung der Daten, Operative Befestigung des Titanimplantats, Charakterisierung des Gesamtsystems (Objektive, Positioniereinheiten, Beatmungsmasken, Bildgebung in der Retina), Anfertigung des Manuskripts

Unterschrift des Doktoranden/der Doktorandin

_____

Acta Neuropathol (2015) 130:799–814
DOI 10.1007/s00401-015-1497-x

ORIGINAL PAPER

Tracking CNS and systemic sources of oxidative stress during the course of chronic neuroinflammation

Agata A. Mossakowski[1,2,3] · Julian Pohlan[1,3,9] · Daniel Bremer[1] · Randall Lindquist[1] · Jason M. Millward[4] · Markus Bock[7] · Karolin Pollok[3,9] · Ronja Mothes[3,9] · Leonard Viohl[3,9] · Moritz Radbruch[1,3] · Jenny Gerhard[1] · Judith Bellmann-Strobl[2,7] · Janina Behrens[2] · Carmen Infante-Duarte[4] · Anja Mähler[7] · Michael Boschmann[7] · Jan Leo Rinnenthal[3] · Martina Füchtemeier[5] · Josephine Herz[6] · Florence C. Pache[1,2,9] · Markus Bardua[1] · Josef Priller[8] · Anja E. Hauser[1,9] · Friedemann Paul[2,7] · Raluca Niesner[1] · Helena Radbruch[3]

Received: 18 August 2015 / Revised: 15 October 2015 / Accepted: 15 October 2015 / Published online: 31 October 2015
© The Author(s) 2015. This article is published with open access at Springerlink.com

Abstract The functional dynamics and cellular sources of oxidative stress are central to understanding MS pathogenesis but remain elusive, due to the lack of appropriate detection methods. Here we employ NAD(P)H fluorescence lifetime imaging to detect functional NADPH oxidases (NOX enzymes) in vivo to identify inflammatory monocytes, activated microglia, and astrocytes expressing NOX1 as major cellular sources of oxidative stress in the central nervous system of mice affected by experimental autoimmune encephalomyelitis (EAE). This directly affects neuronal function in vivo, indicated by sustained elevated neuronal calcium. The systemic involvement of oxidative stress is mirrored by overactivation of NOX enzymes in peripheral CD11b$^+$ cells in later phases of both MS and EAE. This effect is antagonized by systemic intake of the NOX inhibitor and anti-oxidant epigallocatechin-3-gallate. Together, this persistent hyper-activation of oxidative enzymes suggests an "oxidative stress memory" both in the periphery and CNS compartments, in chronic neuroinflammation.

Keywords Multiple sclerosis · Oxidative stress · Neuronal dysfunction · Fluorescence lifetime microscopy · Intravital imaging · Oxidative stress memory

R. Niesner and H. Radbruch are equally contributing senior authors.

Electronic supplementary material The online version of this article (doi:10.1007/s00401-015-1497-x) contains supplementary material, which is available to authorized users.

✉ Raluca Niesner
niesner@drfz.de

✉ Helena Radbruch
helena.radbruch@charite.de

1 German Rheumatism Research Center, Berlin, Germany

2 Department of Neurology, NeuroCure Clinical Research Center, Clinical and Experimental Multiple Sclerosis Research Center, Charité-Universitätsmedizin Berlin, Berlin, Germany

3 Institut für Neuropathologie, Charité-Universitätsmedizin Berlin, Berlin, Germany

4 Institute for Medical Immunology, Charité-Universitätsmedizin Berlin, Berlin, Germany

5 DZNE-German Center for Neurodegenerative Diseases, Berlin, Germany

6 Department of Paediatrics I, Neonatology, University Hospital Essen, Essen 45122, Germany

7 Experimental and Clinical Research Center, Max Delbrueck Center for Molecular Medicine and Charité–Universitätsmedizin Berlin, Berlin, Germany

8 Department of Neuropsychiatry and Laboratory of Molecular Psychiatry, Charité-Universitätsmedizin Berlin, Cluster of Excellence NeuroCure and BIH, Berlin, Germany

9 Intravital Imaging and Immune Dynamics, Charité-Universitätsmedizin Berlin, Berlin, Germany

Introduction

Multiple sclerosis (MS) is a chronic inflammatory neurodegenerative disease characterized by multifocal infiltration of immune cells in the central nervous system (CNS). The first onset of inflammatory symptoms is called clinically isolated syndrome (CIS), and 30–70 % of CIS patients develop definitive MS [34]. In most patients MS has a

relapsing–remitting course (RRMS), which is conventionally considered to reflect mainly inflammatory processes. It can, however, subsequently evolve into a secondary progressive disease (SPMS), thought to reflect more of a degenerative process [27, 41], leading to lasting and irreversible neurological disability.

Reactive oxygen species (ROS) generated by invading and resident CNS macrophages have been implicated in mediating demyelination and axonal damage [13, 38, 55, 58, 60]. The term reactive oxygen species (ROS) refers to both free radicals and related molecules. There is evidence pointing to excessive ROS production as a major mechanism causing damage in MS, as oxidized DNA, lipids and proteins were reported in CNS lesions, cerebrospinal fluid and plasma of MS patients [17, 21, 31]. To prevent ROS-caused damage, cells have potent anti-oxidative mechanisms. However, defects in anti-oxidant mechanisms and excessive ROS production that overwhelms the endogenous anti-oxidant capacity lead to oxidative stress. The most abundant source of ROS leading to oxidative stress is the respiratory burst, which is mediated by the nicotinamide adenine dinucleotide phosphate (NADPH) oxidases [NOX1, NOX2 (phox), NOX3, NOX4, DUOX1, DUOX2] [5]. The NOX enzymes catalyze the oxidation of molecular oxygen to its highly reactive anion O_2^-. Recently, significant up-regulation of NOX2 as well as histological co-localization of cytosolic and membrane-bound NOX2 subunits have been described in MS, at lesion sites [13, 59]. Additionally, subunits of NOX2 are up-regulated in active lesions in experimental autoimmune encephalomyelitis (EAE), an animal model of MS [45]. Furthermore, other members of the NADPH oxidase family, including NOX1 and NOX4 have the capacity to cause oxidative stress in the CNS [11, 30, 36, 43, 49]. NOX1 subunits have been described in active lesions in MS tissue in microglia/macrophages as well as in astrocytes [13], and inhibition of NOX enzymes [9] and knockout of isotype-specific as well as isotype-common NOX subunits (gp91 [29], p47 [57]) decreased EAE severity and incidence. This suggests that NOX enzymes in general are major contributors to oxidative stress by catalyzing the production of ROS, thus leading to CNS tissue damage. However, up to now, neither the catalytic activity of NOX enzymes leading to oxidative stress nor their cellular sources could be tracked, in vivo in the CNS and in the periphery.

Given the increasingly recognized importance of oxidative stress in MS pathogenesis, anti-oxidant drugs are emerging as new therapeutic approaches [15]. One potential candidate is epigallocatechin-3-gallate (EGCG), a polyphenol present in green tea. We and others have shown that EGCG ameliorates EAE [2, 19, 22, 33, 61], and clinical trials testing the benefits of EGCG in MS patients are ongoing (NCT00525668, NCT00799890 and NCT01417312). There is in vitro data pointing to the inhibition of ROS production through EGCG [63]. It is known that EGCG competes with NADPH but not with NADH in binding to NADH-/NADPH-dependent enzymes [46]. However, the therapeutic effects of EGCG in vivo have not yet been analyzed on a cellular level.

Developed two decades ago, fluorescence lifetime imaging (FLIM) has proven to be a reliable, quantitative tool to probe cellular parameters [1, 12, 24, 25, 35, 53]. In particular, the possibility to quantify the endogenous fluorescence of NAD(P)H or of flavoproteins has made FLIM an especially versatile probe of metabolic function [26, 51, 52], as this marker-free approach allows for the acquisition of unaltered, real-time data. Despite its power as a quantitative technique, FLIM requires a high fluorescence signal and thus could not be applied to deep-tissue imaging until recently [4]—a limitation which is particularly relevant to intravital imaging of protected, hardly accessible organs like the CNS [44]. In our previous work, we demonstrated that, in the context of oxidative stress, the increase of fluorescence lifetime of NAD(P)H is specific for NADPH (and not NADH) binding to members of the NOX family, both in murine polymorphonuclear cells [37] and in plant cells (*Nicotiana tabacum*) (unpublished data). These results are supported by recent studies showing the same increase in NAD(P)H fluorescence lifetime, in a more general context [6]. When using NAD(P)H-FLIM, all NADH- and NADPH-dependent enzymes which participate in biochemical reactions within the cell are simultaneously detected (up to several hundred enzymes). Thus, the activation of NOX enzymes can be unequivocally detected only at sites where these enzymes preferentially bind the present coenzymes. The catalytic activity corresponding to such a situation implies an excessive ROS production, and thus oxidative stress, rather than a low, e.g., immunomodulatory, ROS production.

In the present study, we observe a spatio-temporal correlation between the catalysts of oxidative stress (activated NOX enzymes) and neuronal damage in the CNS of mice affected by EAE. Furthermore, we validate this technique in the CNS by identifying macrophages and activated microglia as major cellular sources of activated NOX enzymes, and thus of oxidative stress, in the brain stem of mice with EAE. Using this novel technique, we show for the first time that astrocytes are also major contributors in generating oxidative stress in the CNS during chronic EAE. Additionally, we offer insight into the systemic dimensions of both EAE and MS by quantifying the activity of NADPH oxidases in peripheral monocytes, from the first presentation of symptoms to the chronic phase of the disease. This marker-free approach allows the direct monitoring of the therapeutic mechanism of the anti-oxidative drug EGCG in humans at a cellular and even sub-cellular level.

Methods and materials

Two-photon laser-scanning microscopy (TPLSM)

FLIM experiments were performed using a specialized two-photon laser-scanning microscope based on a commercial scan head (TriMScope, LaVision BioTec, Bielefeld, Germany) [20, 44]. The detection of the fluorescence signals was accomplished either with photomultiplier tubes in the ranges 460 ± 30, 525 ± 25, 593 ± 20 nm or with a 16-channel parallelized TCSPC detector (FLIM-X_{16}, LaVision BioTec, Bielefeld, Germany) in the range 460 ± 30 nm. The excitation of NADH and NADPH was performed at 760 nm (detection at 460 ± 30 nm), of Cerulean (detection at 460 ± 30 nm), sulforhodamine 101 (detection at 593 ± 20 nm) and EGFP (detection at 525 ± 25 nm) at 850 nm and of tdRFP either at 930 nm or at 1110 nm (detection at 593 ± 20 nm). Citrine was detected at 525 ± 25 and 593 ± 20 nm.

For both intensity and fluorescence lifetime imaging we used an average maximum laser power of 8 mW to avoid photodamage. The experimental parameters for FLIM were 160 ps histogram bin (for NAD(P)H-FLIM) and 80 ps histogram bin (for FRET-FLIM) and maximum acquisition time for a 512 × 512 image was 5 s to record a fluorescence decay stack (Suppl. Fig. 3). The time window in which the fluorescence decays were acquired was set to 9 ns.

Data analysis

FLIM data analysis was performed using self-written software based on Levenberg–Marquardt algorithms for non-linear fitting as well as the phasor approach (Suppl. Fig. 6).

Statistical analysis and graphical presentation was carried out with GraphPad Prism 4 (Graphpad Software, USA) and OriginPro (OriginLab, USA). Results are shown as mean values from analyzed data in one mouse/human, in addition the mean ± SD summarize collective data from performed experiments.

Mice

All mice used were on a C57/Bl6 background. The *CerTN L15 x LysM tdRFP* mouse expresses a FRET-based calcium biosensor consisting of Cerulean (donor) and Citrine (acceptor) bound to troponin C, a calcium-sensitive protein present in certain subsets of neurons [18]. Mice carrying the CerTN L15 reporter were crossed to the LysM tdRFP mice, in which tdRFP [32] is expressed in $LysM^+$ cells [10], yielding progeny with both reporters. The $CX_3CR_1^{+/-}$ *EGFP* mouse [23] was used to detect microglia, whereas the $CD4^+$ *YFP* mouse strain was used to detect $CD4^+$ T cells [28, 50]. EAE induction protocol and EAE course of these mice can be found in Table 2, Supplemental Material.

Preparation of the brain stem window for intravital imaging

The preparation of the imaging field was similar to our previous description [47, 48]. For a detailed description, see Supplemental Material. In each imaged animal the whole area that was accessible by intravital imaging was scanned and all visible lesions of each animal were analyzed as well as at least one "normal appearing" imaging field. Animal experiments were approved by the appropriate state committees for animal welfare (G0198/11 and G0181/10, LAGeSo—Landesamt für Gesundheit und Soziales Berlin) and were performed in accordance with current guidelines and regulations.

Human samples

Venous blood samples were obtained with informed consent after the nature and possible consequences of the studies were explained. We included healthy controls, patients with untreated clinically isolated syndrome (CIS), patients with relapsing remitting MS (RRMS-GA) in a randomized double-blind clinical trial medicated with glatiramer acetate receiving additional 600 mg of EGCG or placebo, patients with relapse and remitting MS not treated with any immunomodulatory drugs (RRMS), and patients with a secondary progressive disease course (SPMS); further detailed information can be found in Table I, Supplemental Material. Peripheral blood mononuclear cells (PBMCs) were isolated using standard protocols and $CD11b^+$-enriched by MACS selection (Miltenyi Biotec, Bergisch Gladbach, Germany) according to the manufacturer's protocol. The purity was assessed by flow cytometry. The MACS-enriched $CD11b^+$ monocytes were injected into specifically fabricated chambers and incubated in phenol-free RPMI at 37° C for one hour prior to imaging.

Further experimental details are available in Supplemental Methods.

Results

Activation of NOX enzymes measured by intravital NAD(P)H fluorescence lifetime imaging pinpoints the origin of oxidative stress and correlates with immune infiltration and neuronal dysfunction in EAE

To detect and quantify NOX enzymes activation in vivo, we induced EAE in mice and imaged their brainstem

intravitally. Consistent with previous reports [38], we detected elevated ROS concentrations (~200 µM) in the brain stem of mice affected by EAE at the peak of disease, compared to disease-free control animals (Fig. 1a). ROS were detected by intravital imaging of murine brainstems which had been previously superfused with a 100 µM solution of Amplex Red®. The Amplex Red® calibration was performed using a H_2O_2 concentration series (Suppl. Fig. 2).

As the main catalysts of O_2^- production (precursor of ROS) the membrane-bound NOX enzymes (NOX1,2,3,4 and DUOX1,2) directly contribute to oxidative stress. By employing intravital NAD(P)H fluorescence lifetime imaging (FLIM) we detected the activation of NOX enzymes in the brainstem of EAE mice (Table 2). From the fluorescence intensity decay of NAD(P)H, we evaluated the fluorescence lifetime of enzyme-bound NAD(P)H at each pixel of the image in different layers of the brainstem between 30 and 150 µm depth, as described in Supplemental Material. We expected a mean fluorescence lifetime between 1.1 and 2.7 ns for NAD(P)H bound to metabolic enzymes responsible for basic cellular functions (Suppl. Fig. 4) and a fluorescence lifetime of approximately 3.65 ns for NADPH bound to NOX enzymes as calculated with two independent evaluation methods [37] (Supplemental Material, Suppl. Figs. 4 and 6). Free NAD(P)H has a fluorescence lifetime of approx. 400 ps and is easily distinguished from enzyme-bound NAD(P)H.

The specific NAD(P)H fluorescence lifetime ("NOX only" gate set at 3.3–3.9 ns) corresponding to activated NOX enzymes was detectable in EAE mice mainly within those brainstem regions that included immune cell infiltrations ($LysM^+$tdRFP or $CD4^+$YFP cells, Movie 1); that is, NOX enzymes overactivation was detected in acute lesions, but could not be detected in "normal appearing" areas in the same animal (peak disease, score 2.5, Fig. 1b, c).

The area of NOX-specific activation in acute lesions in the brainstem was significantly enlarged, both at the onset of clinical signs, with a mean of 5 ± 1.5 % in the field of view (300 × 300 μm^2), and at the peak of disease, with a mean area of 14.9 ± 5.8 %, as compared to healthy animals, with a mean area of 2.2 ± 0.9 % (Fig. 1e).

By performing intravital FRET-FLIM in the brain stem of *CerTNL15xLysMtdRFP* mice with EAE, we were able to confirm and extend our previous results indicating neuronal dysfunction during the disease (Fig. 1d, f). We showed previously that elevated Ca^{2+} concentrations over 1 µM in these mice over a period of 1 h reliably indicate neuronal dysfunction [48]. Here, we confirm this finding by showing that neuronal and axonal calcium is increased in areas adjacent to immune infiltrates. Additionally, after 2 h of intravital monitoring, the sites of increased axonal calcium showed axonal disintegration (Fig. 1h). Both the TN L15 construct decay time and the acquisition time of the FRET-FLIM technique are in the range of several 100 ms, allowing for recording time-averaged calcium concentrations relevant for the pathologic dysfunction of neurons. They are, however, both too slow to monitor neuronal calcium transients.

By simultaneously performing NAD(P)H-FLIM and FRET-FLIM in the brainstems of mice with EAE,

Fig. 1 Activation of NADPH oxidases in the CNS pinpoints oxidative stress. Oxidative stress is dependent on disease severity and correlates with cellular inflammation and neuronal dysfunction. ROS concentration in the brain stem of a healthy mouse compared to a mouse affected by EAE at peak of disease (score 2.0) (**a**). Amplex Red® was used as ROS indicator. $\lambda_{exc} = 910$ nm, $\lambda_{em} = 525 \pm 25$ nm (Thy1-Citrine in neurons depicted in *green*), $\lambda_{em} = 593 \pm 20$ nm (Amplex Red®), *scale bar* 50 µm. **b** Correlated 300 × 300 μm^2 (517 × 517 pixel) fluorescence intensity images [Thy1 = *green* (neurons), LysM = *red* (macrophages)], **c** enzyme-bound NAD(P)H-FLIM maps (τ_2-maps) and **d** neuronal Ca^{2+} maps as recorded by FRET-FLIM in three different regions of the brain stem of a *CerTN L15 x LysM tdRFP* mouse with EAE, at the peak of the disease, score = 2.5. *First row* normal appearing white matter; *second row* margin of lesion; *third row* lesion center. The activation of the NADPH oxidases (NOX) assessed by NAD(P)H-FLIM (**c**) correlates with $LysM^+$ tdRFP cell infiltrate in the CNS (**b**) and with elevated neuronal calcium (**d**), indicating neuronal dysfunction. *Scale bars* in **b**, **c** and **d** = 30 µm. The τ_2-maps show the false color-encoded fluorescence lifetime τ of enzyme-bound NAD(P)H at each recorded pixel of the image. NAD(P)H bound to metabolic enzymes are depicted in blue and green (τ between 1 and 3 ns) whereas, under oxidative stress, NADPH bound to activated NOX appears in red (τ between 3.3 and 3.9 ns, "NOX only" gate). **e** Quantification of the NOX activation area within lesions defined by $LysM^+$ cell infiltration, i.e., ratio of the area of NOX only gate to the total tissue area, 4.98 ± 1.53 % at the onset of clinical signs (day 1–2 after appearance of first clinical signs, EAE scores 0.5–1.0) and 14.88 ± 5.81 % of the tissue area at peak of disease (day 3–5 after onset of clinical symptoms, EAE scores 1.5–2.5) as compared to 2.19 ± 0.94 % in healthy controls. Six independent EAE experiments (EAE onset $n = 6$, EAE peak $n = 12$ healthy controls $n = 3$), see Table 2. **f** Quantification of elevated neuronal calcium area is assessed by FRET-FLIM relative to the total neuronal area. Data display means of imaging fields of individual animals from two independent EAE experiments (healthy controls $n = 3$, EAE onset $n = 3$, EAE peak $n = 4$). The increased NOX activity correlates with an increased area of elevated neuronal calcium ("$Ca^{2+} > 1$ µM" gate) at the time of EAE onset (1.32 ± 0.78 %) and at peak disease (12.80 ± 2.41 %), as compared to healthy controls (0 %, $n = 3$, mean calcium concentration 170 nM, maximum calcium concentration 450 nM). **g** Correlation between NOX enzymes activation area and increased neuronal calcium area at lesion sites and non-infiltrated sites in the brain stem of *CerTN L15 x LysM tdRFP* mice affected by EAE. **h** Pathologically increased neuronal calcium level (>1 µM calcium) correlates with immune cell infiltrate and, after 2 h, with axonal break-down as shown by intravital images in the brain stem of a *CerTN L15* mouse affected by EAE (peak)—*scale bar* 10 µm. All images are acquired in the region 30–150 µm depth within the brain stem (300 × 300 × 50 μm^3, z-step = 2 µm). For the statistic evaluation in **e** and **f** we applied ANOVA tests (*$p < 0.05$, **$p < 0.01$, ***$p < 0.001$)

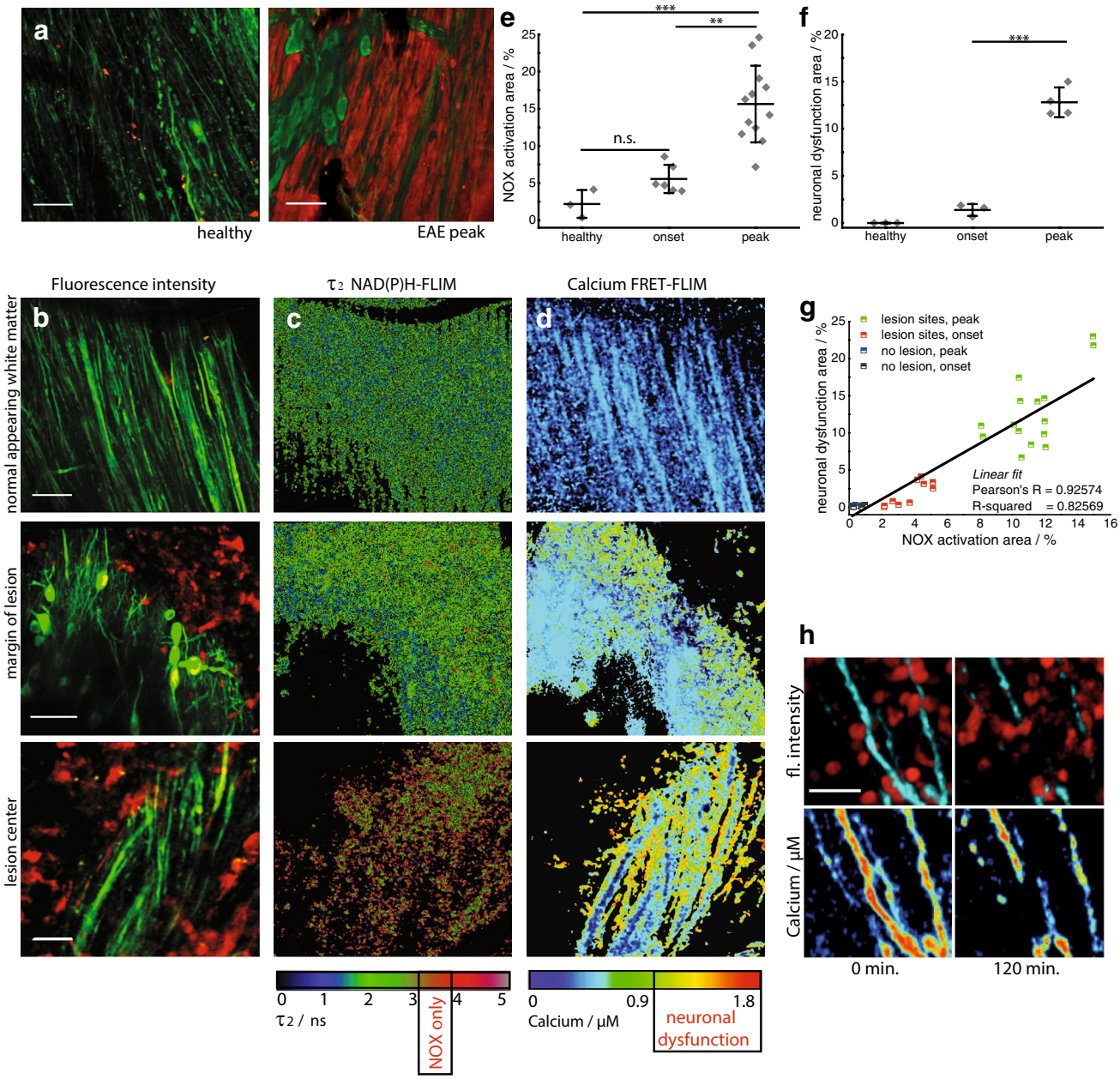

we found that the increased NOX activation correlated with an extended area of elevated neuronal calcium ("Ca^{2+} >1 µM" gate) at EAE onset (1.3 ± 0.8 %) and at peak disease (12.8 ± 2.4 %), as compared to control mice (0 %) (Fig. 1g). The high spatial correlation between areas of NOX enzymes activation and increased neuronal calcium indicating early neuronal dysfunction (Pearson's *R* coefficient over 0.9) in EAE is depicted in Fig. 1g. Interestingly, at lesion sites, both the overactivation of NOX enzymes and the neuronal dysfunction were generally lower at onset than at disease peak. The areas of NOX enzymes activation and increased calcium values were determined as mean values of 3–12 acute lesions per mouse. Each data point in Fig. 1e, f represents the average value for each individual mouse.

Cellular origins of oxidative stress in EAE

We verified the capacity of intravital NAD(P)H-FLIM to identify the cellular origins of oxidative stress directly in the CNS by confirming the contributions of macrophages and activated microglia, which are well-known contributors to the activation of NOX enzymes during EAE. Subsequently, we used the unique versatility of this technique to identify novel cellular sources of oxidative stress by performing endogenous NAD(P)H-FLIM in the CNS

of EAE mice with a variety of fluorescently labeled cell subsets. Here, we evaluated the relative contributions of each cell type (LysM$^+$tdRFP, CerTNL15, CD4$^+$YFP, $CX_3CR_1^{+/-}$EGFP or sulforhodamine101 labeled cells) to the total area of NOX enzymes activity.

Characterization of cellular markers

The reliability of the chosen cellular markers used in the intravital experiments was verified by flow cytometry or histology in mice affected by EAE. While in healthy LysM$^+$tdRFP animals only rare tdRFP$^+$ cells can be found in the CNS, during EAE ($n = 4$) the tdRFP$^+$ compartment increased markedly at lesion sites. Of the tdRFP$^+$ cells, 65 % were CD45^{high}CD11b$^+$Ly6G$^-$ (macrophages), 25 % CD45^{low}-CD11b$^+$ (microglia) and 7 % CD45^{high}CD11b$^+$Ly6G$^+$ (neutrophil granulocytes) (Fig. 2a). The overlap of LysM$^+$tdRFP cells with $CX_3CR_1^+$ cells was quantified by flow cytometry using an anti-CX_3CR_1 antibody. 17.8 ± 8.9 % of all LysMtdRFP$^+$ cells were $CX_3CR_1^+$CD45^{low} (microglia) and 27.6 ± 10.1 % were $CX_3CR_1^+$CD45^{high} (macrophages). This represented only a minority of the total $CX_3CR_1^+$ cells as displayed in the 2.8 ± 1.4 % of cells that co-expressed LysM-tdRFP ($n = 3$) (Fig. 2b).

In disease-free control animals, sulforhodamine 101 (sulforh101) specifically labels astrocytes in the cortex [39, 40]. To characterize the cells labeled with sulforh101 during EAE in the brainstem we analyzed by immunofluorescence intracellular sulforh101 (following i.v. injection) as well as GFAP and CD11b expression. Minimal co-localization (6.1 ± 1.4 %) of sulforh101 labeling with CD11b staining could be observed at EAE lesion sites in the brainstem (Fig. 2c). We detected sulforh101 co-localization mainly with GFAP^{low} cells [16] but not with GFAP^{high} cells (Fig. 2d). 80 ± 6 % of sulforh101-labeled cells were GFAP$^+$, whereas this cell population represents only half of all GFAP-expressing cells (Fig. 2d). Intravital imaging data recorded in the brainstem of $CX_3CR_1^{+/-}$EGFP mice additionally labeled with sulforh101 showed negligible overlap between the EGFP and sulforh101 labeling, typically 2 ± 1.5 %, both in healthy controls and in mice affected by EAE (Fig. 3a). The lesions investigated by intravital imaging in the brainstem showed typical EAE characteristics, which we confirmed by histology (Suppl. Fig. 1).

Phagocytic capacity of astrocytes and their potential role in EAE

We focused on astrocytes as potential contributors to oxidative stress during neuroinflammation as they are known to have phagocytic capacity. Morphological analysis of our intravital experiments revealed a disruption of the fine process-rich astrocytic network typically found in healthy control animals (Fig. 3a), similar to that which could be seen on histological staining (Fig. 2). The disruption of the astrocytic network was associated with changes towards a reactive phenotype and glial scar formation at lesion sites, with dense accumulations of astrocytic end feet and processes lining up along the vessels and around inflammatory cells ($CX_3CR_1^+$) in EAE (Figs. 2d, 3a).

Furthermore, NAD(P)H-FLIM analysis in astrocytes using beads for phagocytosis coated with *Staphylococcus aureus* fragments (pHrodo) in mixed cell cultures with microglia showed increased NAD(P)H fluorescence lifetime typical of NOX enzymes activity. We could correlate increased NOX enzymes activation with the localization of phagocytosed pHrodo beads (red) (Fig. 3b).

As the expression of p22 NOX subunit in astrocytes during EAE is only sparse [45], we investigated Noxo1 expression by immunofluorescence to address the question which NOX enzyme could be responsible for the observed NAD(P)H lifetime prolongation. NOX1 function is less dependent on p22 coexpression compared to other isoforms [54]. We could detect in GFAP^{high} cells and GFAP^{low} cells Noxo1 expression (Fig. 3c, d) including GFAP^{low} and sulforh101-co-labeled cells (Fig. 3g) in EAE lesions. Furthermore, Noxo1 was also found in CD11b$^+$ cells (with both phagocytic and microglial morphology) (Fig. 3e).

Altogether, these data suggest that astrocytes generate oxidative stress within the CNS during the course of chronic neuroinflammation.

Astrocytes are major cellular contributors to oxidative stress in EAE

We quantified the contribution of specific cell types to the total area of NOX enzymes activity in the CNS using the cellular markers described above. In line with previous studies, we found that the mean contribution of LysM$^+$ cells amounted to 22.7 ± 6.4 % at onset, and 28.2 ± 4.7 % at the peak of EAE. Additionally, the mean contribution of $CX_3CR_1^+$cells amounted to 13.1 ± 2.3 % at onset, and 17.4 ± 2.4 % at the peak of EAE. Macrophages and microglia (either LysM$^+$ and/or $CX_3CR_1^+$) together constitute the main source of oxidative stress at onset and peak of the disease (Fig. 4d). This finding confirms the reliability of our method to evaluate oxidative stress by detecting the activation of NOX enzymes.

Using this novel approach, we found that although microglia and macrophages are the main sources of NOX enzymes activity, a significant fraction could not be attributed to those cell types. Surprisingly, we found that astrocytes (sulforhodamine 101-labeled cells [3]) accounted for 26.4 ± 4.4 and 34.2 ± 5.6 % of total area of NOX enzymes overactivation at onset and peak of EAE, respectively (Fig. 4d). In this model, the contribution of astrocytes to

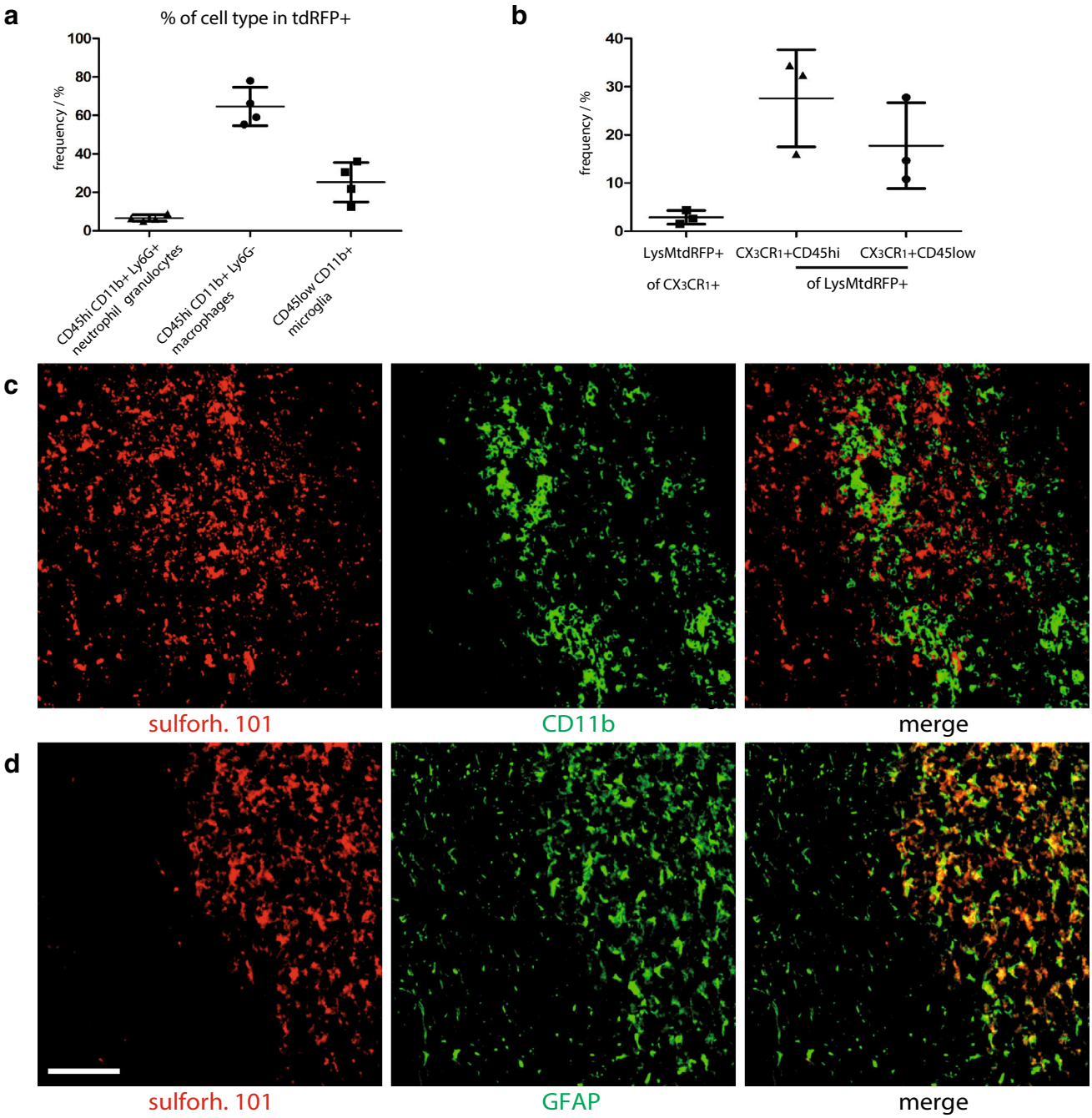

Fig. 2 Characterization of active lesions as well as of LysMtdRFP$^+$ and sulforhodamine 101 labeled cells during EAE. **a** FACS analysis data in the CNS of LysM$^+$tdRFP mice at peak EAE, characterizing the tdRFP$^+$ cell population ($n = 4$). **b** FACS analysis data in the CNS of LysM$^+$tdRFP mice ($n = 3$) at peak EAE showing the overlap of LysMtdRFP and CX_3CR_1-antibody labeled cells. **c** Immunofluorescence images within the brain stem of a C57Bl6 mouse affected by EAE, at peak of the disease, showing no co-localisation between sulforhodamine 101 (*red*) and CD11b$^+$ cells (*green*) at infiltration sites. **d** Immunofluorescence images within the brain stem of the same mouse, showing colocalization between sulforhodamine 101 (*red*) and GFAP$^+$ cells (*green*) at reactive gliosis sites. *Scale bar* 200 µm

oxidative stress within the CNS is comparable to that of the labeled macrophages and microglia together, thus identifying astrocytes also as central contributors to oxidative stress in the acute phases of EAE.

The mean contribution of CD4$^+$cells to NOX enzymes activity was negligible, amounting to 3.6 % at peak disease, comparable to the mean contribution of neurons with 2.3 % at onset and 3.8 % at peak of EAE (Fig. 4d).

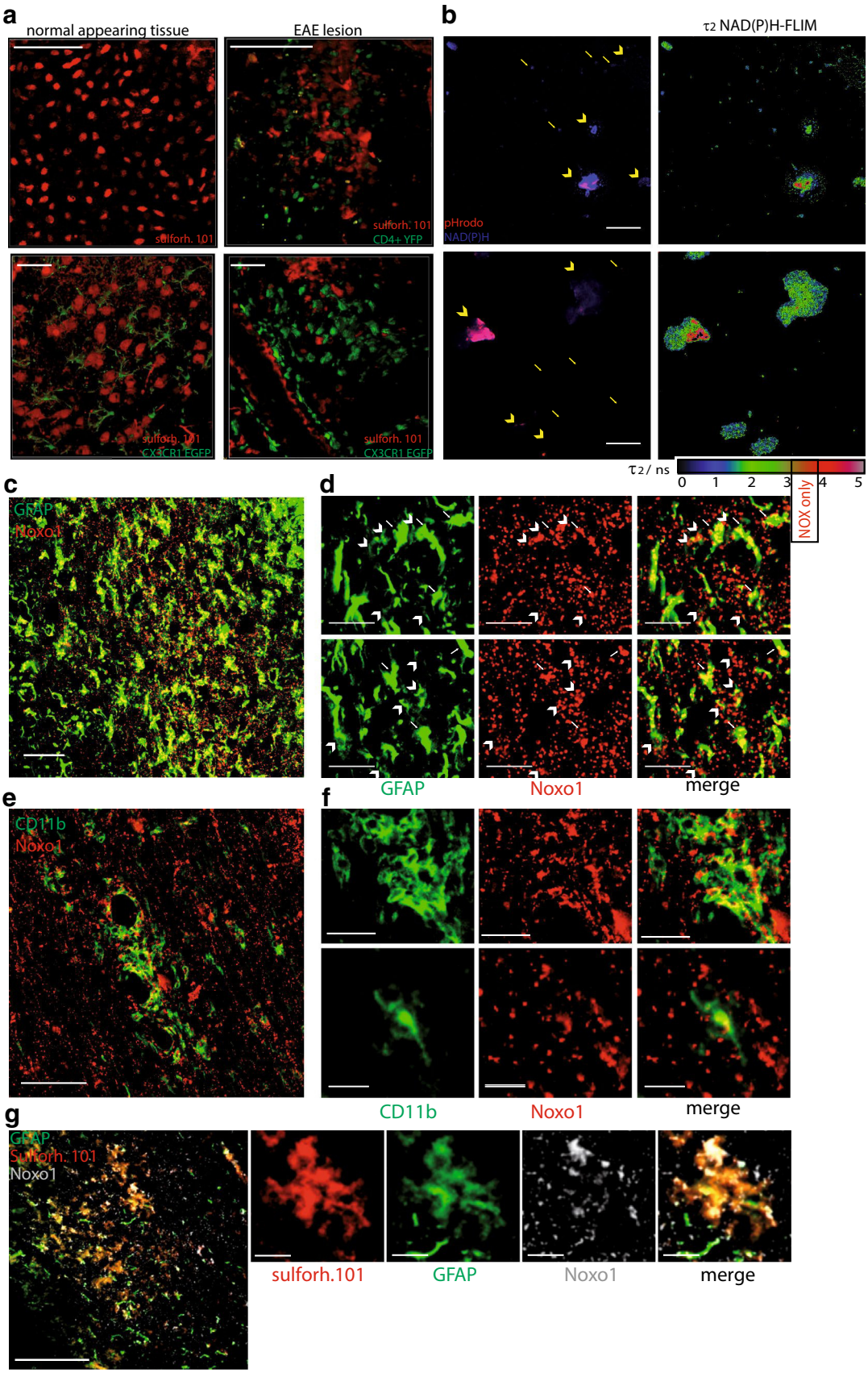
a
normal appearing tissue
EAE lesion
sulforh. 101
sulforh. 101
CD4+ YFP
sulforh. 101
CX3CR1 EGFP
sulforh. 101
CX3CR1 EGFP
b
τ2 NAD(P)H-FLIM
pHrodo
NAD(P)H
τ2 / ns
0 1 2 3 4 5
NOX only
c
GFAP
Noxo1
d
GFAP
Noxo1
merge
e
CD11b
Noxo1
f
CD11b
Noxo1
merge
g
GFAP
Sulforh. 101
Noxo1
sulforh.101
GFAP
Noxo1
merge

◀**Fig. 3** Astrocytes as phagocytes and their potential role in EAE. **a** 3D fluorescence intensity images were acquired in the brain stem of $CD4^+$ YFP mice: healthy controls (*upper*, *left panel*) and at a lesion site, in EAE (*upper*, *right panel*) [$CD4^+$ cells (YFP) = *green*, astrocytes (sulforhodamine 101) = *red*]. *Scale bar* 100 µm. Similarly, 3D fluorescence intensity images were acquired in the brain stem of $CX_3CR_1^{+/-}$ EGFP mice: healthy controls (*lower*, *left panel*) and at the lesion site in EAE (*lower*, *right panel*) [microglia/macrophages (EGFP) = *green*, astrocytes (sulforhodamine 101) = *red*]. *Scale bar* 30 µm. **b** NAD(P)H fluorescence images (*blue*) of mixed astrocytes (*arrow head*) and microglia (*arrows*) cell cultures phagocytosing *Staphylococcus aureus* beads (pHrodo, *red* after uptake) are shown on the *right side*. Corresponding NAD(P)H-FLIM maps (τ_2-maps) shown on the *left side* reveal the correlation between phagocytosis of pHrodo beads and the typical increase of fluorescence lifetime in astrocytes indicating the activation of NOX enzymes. **c** Immunofluorescence overview image within the brain stem of a mouse affected by EAE indicating the distribution of Noxo1 (subunit of NOX1, *red*) and GFAP signal (*green*). *Scale bar* 100 µm. **d** Zoom ins of **c** demonstrating that Noxo1 is found both in $GFAP^{high}$ cells (indicated by *white arrows*) and $GFAP^{low}$ cells (indicated by *white arrow heads*) in the CNS of mice affected by EAE. *Scale bar* 30 µm. **e** Immunofluorescence overview image within the brain stem of a mouse affected by EAE indicating the distribution of Noxo1 (subunit of NOX1, *red*) and CD11b signal (*green*). *Scale bar* 150 µm. **f** Zoom ins of **e** demonstrating that Noxo1 is found in $CD11b^+$ cells (with both phagocytic and microglial morphology). *Scale bar* 40 µm (*upper panels*), *scale bar* 20 µm (*lower panels*). **g** Immunofluorescence overview image within the brain stem of a mouse affected by EAE indicating the distribution of Noxo1 (subunit of NOX1, *gray*), GFAP signal (*green*) and sulforh101 signal (*red*). *Scale bar* 200 µm. **h** Zoom in of **g** demonstrating that Noxo1 is found in $GFAP^{low}$, sulforh101-labeled cells. *Scale bar* 30 µm

We further analyzed the fraction of activation within each cell subset by calculating the percentage of the specific cell area that shows NOX enzymes activation, as well as averaged values per mouse displayed in Fig. 4e. The area of NOX enzymes activation within neurons ($Thy1^+$ cells in *$LysM^+$tdRFPxCerTNL15* mice) was very small, both at clinical onset and at peak of disease with less than 2 %. Conversely, in $LysM^+$tdRFP cells the area of NOX enzymes activation was generally higher with 8 % at clinical onset and rising significantly to 27 % at peak disease (Fig. 4e). The area of NOX enzymes activation in $CX_3CR_1^{+/-}$EGFP cells was 11 and 14 %, respectively. We obtained similar data in astrocytes with 12 % at onset and 10 % in peak. In $CD4^+$YFP cells, the area of NOX enzymes activation was low at peak of disease, amounting to only 3 %.

In our experimental setup, not all cells of the specific cell subtype are fluorescently labeled also due to the use of heterozygous fluorescent mouse strains, but we could address the majority of cells with our labeling strategy. The remaining percentage of NOX enzyme activation area that was not associated with labeled cells in this model (12.85 % at peak, 35.46 % in onset of EAE) is probably due to unlabeled macrophages, microglia and/or astrocytes. The contribution of other immune or CNS-specific cell types, such as oligodendrocytes or immune cells with phagocytic capacity, to the generation of oxidative stress cannot be completely excluded but is expected to be low.

Soluble factors drive activation of NADPH oxidases in EAE

Regarding the co-localization of neuronal structures ($Thy1^+$ cells) and $LysM^+$ cells in *CerTNL15xLysMtdRFP* mice, we found that only a 28 to 30 % of the co-localized area was associated with increased NOX enzymes activation in EAE (Fig. 4f, h). The normalized co-localization index, calculated as we previously described [48] indicated significantly more extensive interaction between neurons and macrophages at peak disease than at the time of onset (Fig. 4g), independently of the number of neurons or macrophages at the imaged site. Thus, while the interactions between neurons and $LysM^+$ cells were more extensive with the progression of the disease, NOX enzymes activation was not specifically induced by neurons or by their direct interaction with $LysM^+$ cells. On the other hand, we showed that upon applying glutamate (300 µM) locally to the brainstem of healthy mice, the NOX enzymes activation area increased from values typical for control animals (0.7 ± 0.2 %) to values similar as those reached in peak of EAE (11.9 ± 3.1 %) (Suppl. Fig. 5), indicating that glutamate-induced excitotoxicity can lead to similar levels of NOX enzymes activation as are present in acute EAE lesions. These data support the interpretation that the cause of NOX enzymes activity in macrophages, activated microglia and astrocytes within the CNS in EAE is not necessarily triggered by direct contact to CNS components like axons, but is rather associated with soluble factors, such as glutamate or inflammatory mediators.

NOX is overactivated in peripheral $CD11b^+$ monocytes in both MS and EAE and can be ameliorated by systemic administration of EGCG

To translate our findings to MS, we isolated $CD11b^+$ monocytes from peripheral blood mononuclear cells (PBMC) taken from MS patients, at different stages of the disease, including CIS, RRMS and SPMS. In healthy humans and healthy mice, $CD11b^+$ monocytes were not activated after isolation, i.e., the area of NOX activation amounted to 3.4 ± 0.6 and 3.4 ± 1.9 %, respectively. In untreated RRMS patients, the area of NOX activation was 18.3 ± 2.5 %, in mice at peak of EAE, the NOX activation area was 18.5 ± 3.5 %. The high levels of NOX activation in peripheral $CD11b^+$ cells of mice with EAE and of untreated RRMS patients could be ameliorated by treatment with glatiramer acetate (GA) alone, to only 10.8 ± 2.8 % (in RRMS patients). Upon combination treatment with both GA and additional systemic administration

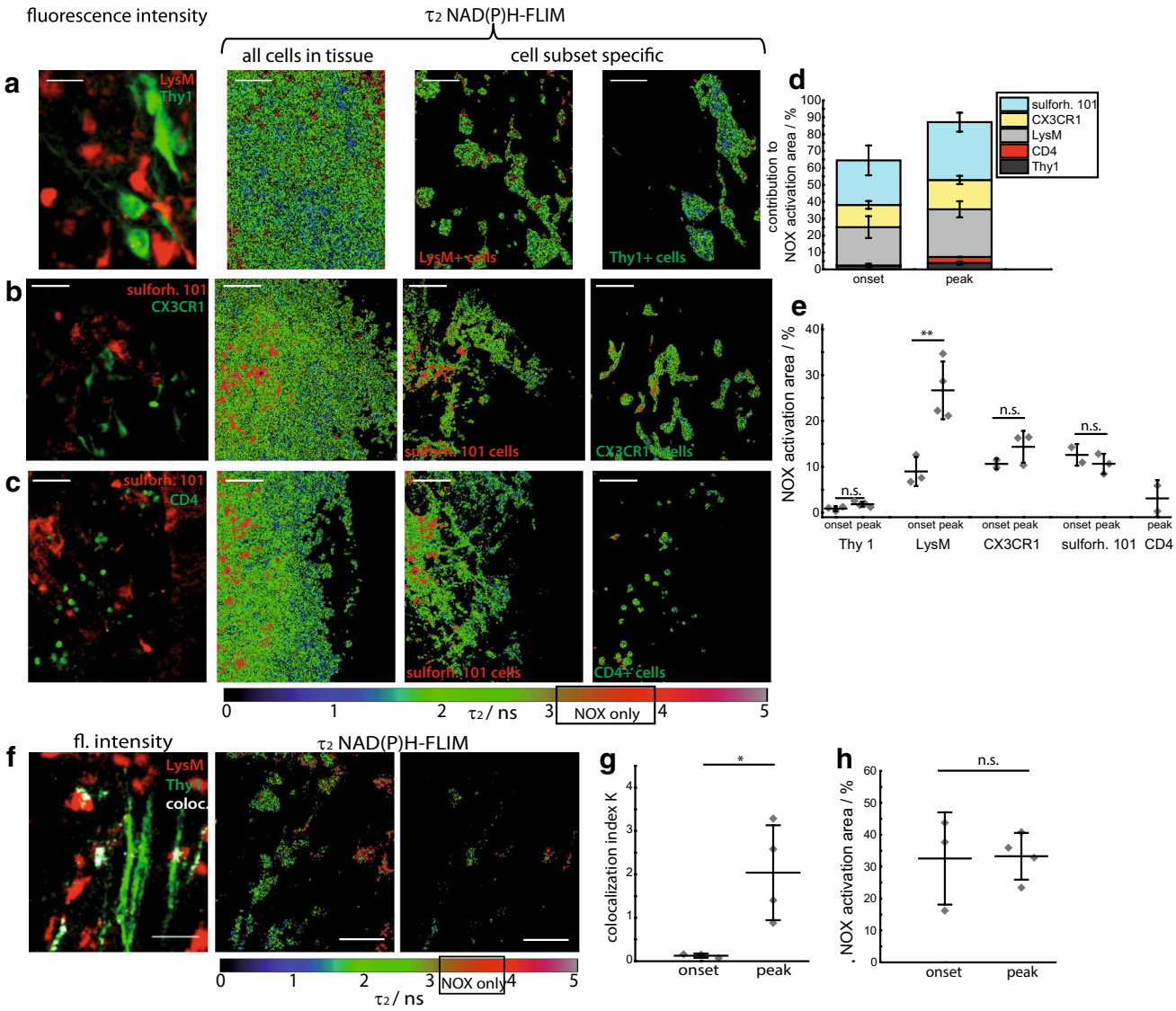

of EGCG, levels were even further reduced, almost to the levels of healthy controls: 5.8 ± 3.4 % in mice and 6.4 ± 1.2 % in RRMS patients (Fig. 5).

To understand the kinetics of NOX activation leading to oxidative stress during the course of the disease, we analyzed PBMCs of newly diagnosed (untreated) patients with CIS, untreated RRMS patients and differently treated SPMS patients. We observed little NOX activation in CIS patients (3.6 ± 1.2 %), and markedly elevated NOX activation in untreated RRMS patients (18.3 ± 2.5 %) and in treated SPMS patients (15.1 ± 3.2 %) (Fig. 5b). These data could be reproduced in mice, since at onset of disease $CD11b^+$ splenocytes showed almost normal NOX activation (5.0 ± 1.1 % %), while at peak of disease the values were similar to those measured in untreated RRMS patients (18.5 ± 3.5 %). Immunization with adjuvant only (CFA without MOG) did not increase NOX activation (3.0 ± 0.9 %) in $CD11b^+$ splenocytes. All values of NOX activation area represent mean values acquired over 30–120 cells per individual.

To address if EGCG counteracts a possible overexpression of NOX2 subunits in MS, rather than direct NOX2 overactivation, we performed qRT-PCR analysis of PBMCs from ECGC-treated and untreated patients. We did not detect any differences in the expression level of the gp91 (NOX2 subunit) in patients treated with GA and placebo as compared to treatment with GA and EGCG (Fig. 6e), indicating that the reduced activation of NOX2 in EGCG-treated patients was not caused by reduced gp91 gene expression. Rather, this observation could be explained by direct inhibition of NOX2 activation by EGCG, which is in accordance with the fact that EGCG competes with NADPH in binding to the NADPH-binding site of enzymes [6] including the NADPH oxidases (NOX enzymes). In

◀**Fig. 4** Cellular origin of NADPH oxidases activity in the CNS of EAE mice. **a** The fluorescence intensity image and the τ_2 NAD(P)H-FLIM map of whole tissue area was used to analyze the cellular origin of NOX activation signal in the CNS. Therefore, we performed an overlay of both images and analyzed the NAD(P)H-FLIM signal at the areas of the respective cell types. Exemplarily LysM$^+$ cells as well as Thy1$^+$ cells (neurons) in **(a)**, $CX_3CR_1^{+/-}$ EGFP—*green* or sulforhodamine 101—*red* (astrocytes) in **b** and CD4$^+$ YFP—*green* (T cells) or sulforhodamine 101—*red* (astrocytes) in **c** are shown in the brain stem of mice affected by EAE. All τ_2 NAD(P)H-FLIM images depict the normalized area of NOX activation in relation to the total cellular area in the respective cell subsets. *Scale bar* 30 µm (**a**) and 50 µm (**b**, **c**). Quantification of the contribution of LysM, Thy1, CX_3XR_1, CD4$^+$ and sulforhodamine 101-labeled cell subsets, respectively, to the total area of NOX enzymes activation within a lesion. LysM$^+$ phagocytes: 22.7 % at onset and 28.2 % at the peak of EAE, $CX_3CR_1^+$ cells: 13.1 % at onset and 17.4 % at the peak of EAE, astrocytes (sulforhodamine 101): is 26.2 and 37.0 %, CD4$^+$ cells: 3.6 % at peak disease, neurons (Thy1$^+$): 2.3 % at onset and 3.8 % at peak (**d**). To analyze the proportion of activated cells in one specific cell subset, we quantified the NOX enzymes activation area relative to the total area of the respective cell type at onset and peak of disease (**e**). The area of NOX activation within neurons (Thy1$^+$ cells in the *LysM$^+$tdRFP x CerTN L15* mice): onset 0.8 ± 0.5 % and peak 1.8 ± 0.4 %, LysM$^+$ cells onset 7.9 ± 2.3 %, and peak 26.4 ± 6.6 %, $CX_3CR_1^+$ cells: onset 10.6 ± 0.6 % and peak 14.4 ± 1.7 %, astrocytes (sulforhodamine 101): onset 11.7 ± 0.6 % and peak 9.8 ± 1.6 %, CD4$^+$ cells: peak 3.1 ± 2.0 %. Data from 2 EAE experiments in *LysM$^+$tdRFP x CerTN L15* mice, $n = 3$ onset, peak $n = 4$; 2 EAE experiments in *$CX_3XR_1^{+/-}$ EGFP* mice labeled with sulforhodamine 101, $n = 2$ onset and $n = 3$ peak; 1 EAE experiment in *CD4$^+$ YFP* mice labeled with sulforhodamine 101, peak $n = 2$ (**e**). *Left* fluorescence intensity image of brain stem lesion in EAE (Thy1 = *green*, LysM = *red*, colocalisation = *white*). τ_2 (enzyme-bound) NAD(P)H-FLIM image of LysM$^+$tdRFP cells in tissue (*middle*) and at the Thy1/LysM colocalisation area (*right*) depicts the normalized area of NOX enzymes activation in relation to total LysM$^+$ cellular area as well as the activation within the colocalisation area. *Scale bar* 30 µm (**f**). The normalized colocalisation index indicates the interaction level between LysM$^+$ and Thy1 cells, respectively, in onset and in peak of the disease, in the same experiments (**g**). Quantification of the mean NOX activation area of individual mice relative to the total area of LysM/Thy1 colocalisation at the onset ($n = 3$) and peak ($n = 4$) of disease, two independent EAE experiments (**h**). All images are acquired in 30–150 µm depth within the brain stem (z-step = 2 µm). For statistic evaluation in **d** we applied the ANOVA test, in **g** and **h** Mann–Whitney *U* tests (*$p < 0.05$, **$p < 0.01$, ***$p < 0.001$)

vitro data from our group using 100 µM EGCG yielded similar results, as they lead to an immediate shift with more free NAD(P)H with a shorter fluorescence lifetime (data not shown).

As NOX2 activity requires the fusion of the membrane-bound p22 and cytosolic p47 components, we examined the co-localization of p22 and p47 in human CD11b$^+$ PBMCs by imaging cytometry to confirm our FLIM data with an independent approach. The co-localization was quantified as the Bright Detail Similarity (BDS), which measures the correlation coefficient between the intensities in localized bright spots of radius 1 µm or less. In healthy donors, less than 0.1 % of CD11b$^+$ cells demonstrated co-localization of the p22 and p47 subunits, as indicated by a BDS >2, while RRMS patients had a markedly increased proportion of cells in which the two subunits co-localized, with 3.6 % of CD11b$^+$ cells having a BDS >2 (Fig. 6a–c). Using a DCF (Di-Chloridium Fluorescein) fluorescence-based ROS/RNS detection assay in serum, we measured a general trend towards lower ROS/RNS concentrations in GA-treated RRMS patients with EGCG co-therapy as compared to placebo (Fig. 6d). Consistent with MS pathology (with the brain as the target of inflammation) and the frequencies of overactivated cells in the blood as detected with imaging cytometry, the ROS/RNS are highly diluted in serum, and were not significantly different between the groups under investigation.

Discussion

To elucidate how oxidative stress causes neuronal degeneration and to clarify the mechanisms of anti-oxidant therapy, it is necessary to have a tool which allows real-time monitoring of functional changes at cellular and sub-cellular level. Applying this tool both within the central nervous system—where the damage takes place—and in the peripheral immune system demonstrates novel links between human disease and animal models, and offers unique functional insights into the systemic impact of MS.

In the present study, we monitored for the first time the functionality of NADPH oxidases catalyzing the production of ROS, which leads to oxidative stress in vivo. The fact that NOX enzymes are membrane-bound enzymes facilitates the identification of their cellular origins. Our intravital imaging and marker-free NAD(P)H-FLIM data demonstrate that NADPH oxidases are overactivated in astrocytes (sulforh101 labeled) during neuroinflammation, in addition to the known contributors, LysM$^+$ and $CX_3CR_1^+$ phagocytes, previously reported and recently corroborated in bone marrow chimeric mice deficient for NRROS, a negative regulator of ROS [38, 42]. Our intravital data regarding the role of astrocytes in chronic neuroinflammation are supported by histological studies showing that Noxo1 is expressed in GFAP$^+$ cells, and that negative p22 immunostaining [45] in astrocytes does not exclude a NOX2-independent functional NADPH oxidases activation in vivo [54]. Additionally, we showed that NOX enzymes activation was spatially associated with lesion sites in EAE, and correlated with locations of neuronal dysfunction. This finding is consistent with the report that mice with knockout of the common subunit of NOX enzymes (p47$^{-/-}$ mice) are more resistant to EAE [57] supporting the idea that NOX2, the phagocytic isotype, is not the only member of the NOX family that may contribute to excessive ROS production in chronic neuroinflammation. In line with this, mice lacking only NOX2 (gp91$^{-/-}$) develop only a slightly milder form of EAE [29] and expression levels of NOX enzyme subunits other than NOX2

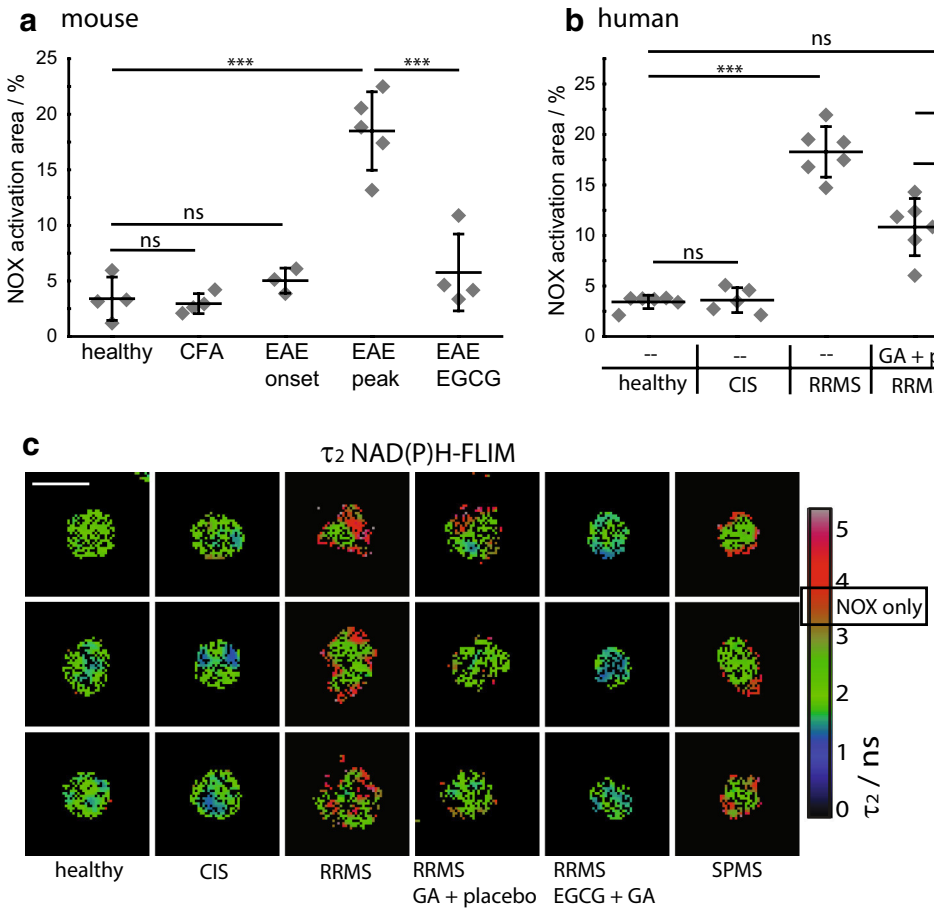

Fig. 5 NOX activation in murine and human peripheral CD11b$^+$ cells during chronic neuroinflammation as compared to treatment with EGCG. **a** Quantification of mean normalized area of NOX activation as measured from τ_2 (enzyme-bound) NAD(P)H fluorescence lifetime images of MACS-purified splenic CD11b$^+$ monocytes from healthy controls ($n = 4$), from mice immunized only with Freund's Complete Adjuvant (CFA, $n = 4$) and from mice with EAE—at onset of disease ($n = 3$), at peak of disease ($n = 5$) or treated with EGCG ($n = 4$) encompassing two to four independent EAE experiments. **b** Quantification of mean normalized area of NOX activation of MACS-enriched blood CD11b$^+$ human monocytes from age- and gender-matched healthy controls ($n = 6$), patients with clinically isolated syndrome (CIS, $n = 5$), untreated RRMS patients ($n = 6$), RRMS patients treated either with glatiramer acetate (GA) and placebo ($n = 6$) or with glatiramer acetate and EGCG ($n = 6$) as well as SPMS patients with their regular MS-related therapy ($n = 6$). **a**, **b** Data points are mean values of at least 50 cells from one individual, for the statistic evaluation we applied ANOVA tests (*$p < 0.05$, **$p < 0.01$, ***$p < 0.001$). **c** Representative color-encoded τ_2 NAD(P)H fluorescence lifetime images of MACS-enriched blood CD11b$^+$ human monocytes

were elevated within active MS lesions [13]. One additional candidate is NOX1, which was reported to be neurotoxic in microglia [8]. Importantly, our NAD(P)H-FLIM technique to detect the catalysis of oxidative stress does not discriminate between NOX isotypes. Rather, it detects their increased activation as compared to other NAD(P)H-dependent enzymes responsible for basic cellular processes that are present in the same observation volume ($0.4 \times 0.4 \times 1.5\ \mu m^3$). Therefore, the hallmark of our technique is its capacity to monitor excessive NOX enzyme function as a reliable indicator of oxidative stress, rather than dissecting the activation of specific NOX isotypes.

NADPH oxidases activation was not restricted to a specific cell type, and was not preferentially found co-localized with the major compartments of the immune system (macrophages/activated microglia) and of the CNS (neurons), suggesting a predominant contribution of locally acting soluble factors like TNF-α or glutamate [15, 62]. Glutamate is not only an excitotoxic factor but was also shown to induce NOX activation. Supporting this interpretation, we found that local treatment with glutamate caused a significant increase of the NOX enzymes activation area as revealed by intravital NAD(P)H-FLIM in the brain stem of healthy mice (Suppl. Fig. 5).

As macrophages/microglia are two of the main producers of ROS in EAE, it was unexpected that only up to 50 % of the area of macrophages/microglia (LysM$^+$tdRFP cells and $CX_3CR_1^{+/-}$EGFP cells) showed activation of NOX

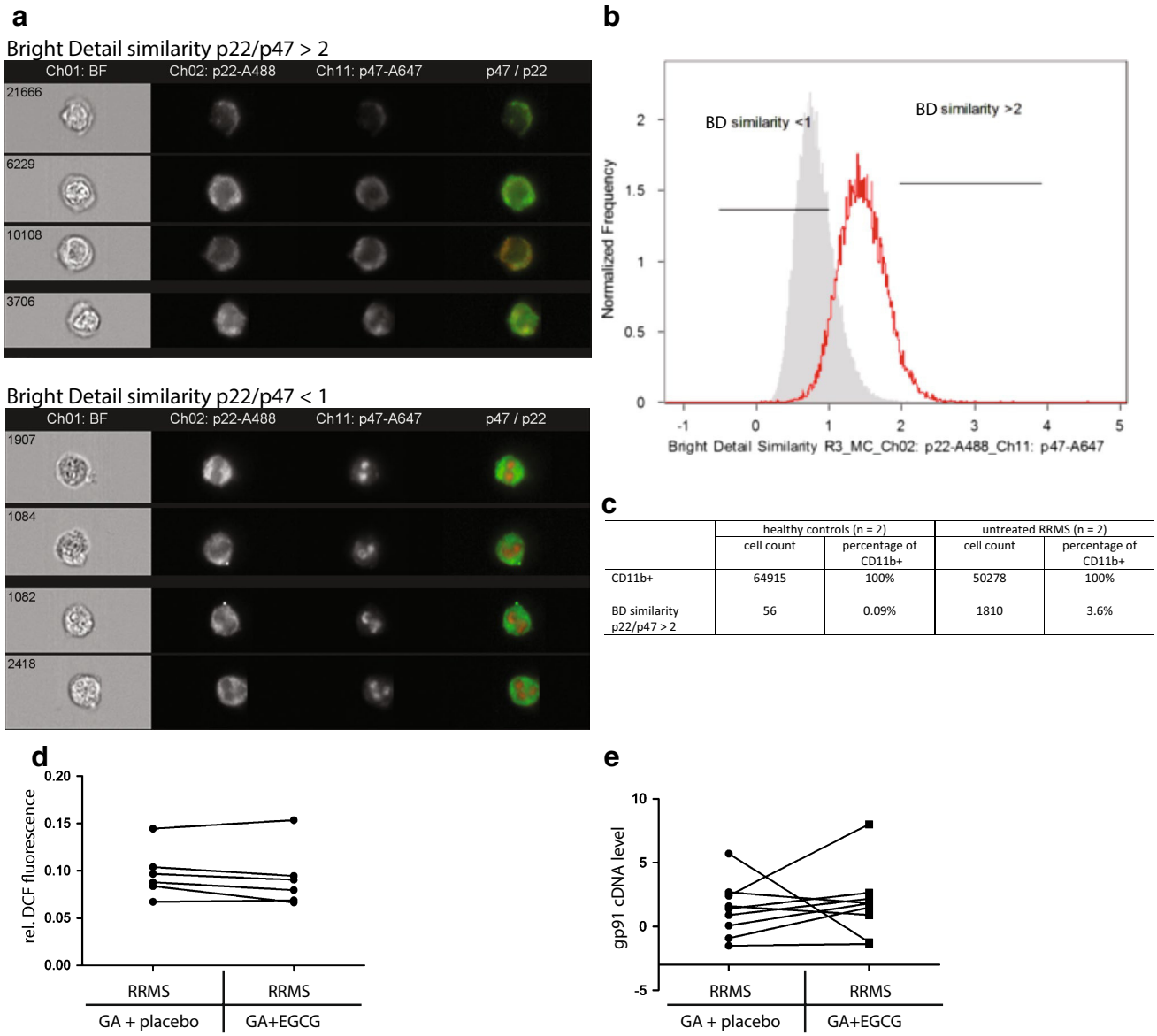

	healthy controls (n = 2)		untreated RRMS (n = 2)	
	cell count	percentage of CD11b+	cell count	percentage of CD11b+
CD11b+	64915	100%	50278	100%
BD similarity p22/p47 > 2	56	0.09%	1810	3.6%

Fig. 6 NOX subunits expression levels and co-localization in human peripheral CD11b$^+$ cells as well as ROS detection in serum during chronic neuroinflammation. **a** Representative images of cells, generated by imaging flow cytometry immunostained for CD11b, p22 (membrane-bound NOX subunit) and p47 (cytosolic NOX subunit). Cells shown are gated on CD11b (not shown). The upper panel depicts cells with high bright detail similarity (>2) between p22 and p47 patterns (activated NOX), whereas the lower panel shows cells with low bright detail similarity (<1). **b** Less CD11b$^+$ cells of a healthy control show high similarity (>2) between p22 and p47 as compared to an untreated RRMS patient. **c** The table depicts corresponding cell numbers and percentages from two healthy controls and two untreated RRMS patients showing that CD11b$^+$ cells with high similarity between p22 and p47, indicating activated NOX, are at least 20× more frequent in untreated RRMS patients than in healthy controls. **d** Results of DCF fluorescence-based ROS/RNS detection assay in serum of patients show a general trend of lower ROS/RNS production in glatiramer acetate (GA) treated RRMS patients after EGCG complementary therapy as compared to placebo. **e** Analyzed gp91 cDNA levels of PBMCs with qRT-PCR showed no difference in expression levels in patients pre- or post-treatment with EGCG

enzymes in vivo (Fig. 4e). This is consistent with the findings that the reactive oxidative burst is counter-regulated in MS by myelin-loaded macrophages up-regulating antioxidant enzymes [14, 17, 58]. The toxic role of excessive ROS production in MS pathogenesis has been proposed to be related to multiple mechanisms, including enhanced blood–brain barrier transmigration [56], oligodendrocyte damage, and mitochondrial damage leading to further ROS production. Here, we provide evidence for an additional mechanism of NOX enzymes-mediated pathogenesis in MS: direct induction of neuronal dysfunction. We demonstrated in vivo that NOX enzymes activity leading

to excessive ROS production was spatially correlated with pathologically increased neuronal calcium—a reliable indicator of neuronal dysfunction at lesion sites [7, 48].

The activation of astrocytes towards oxidative stress generation in chronic neuroinflammation supports the hypothesis that these cells are partially responsible for the accumulated neuronal dysfunction and damage over the course of the disease. In the later phases of the disease, activated astrocytes and microglia may continue to enhance neuronal loss even in the absence of overt immune infiltration of the CNS. Thus, these cells may become a major target of therapy, especially in the progressive phase of the disease. We also employed our NAD(P)H-FLIM technique, under in vitro conditions, to monitor NOX enzymes activation in peripheral cells. The elevated NOX activation in monocytes from the periphery of EAE mice and of MS patients at various stages of the disease strengthens the view that both MS and EAE have a complex systemic dimension. Increased NOX activation in peripheral monocytes is not specific for MS, as we could also see moderately elevated NOX activation in individuals with common cold (data not shown). However, we saw a significant increase of NOX activation with disease progression, similar to our observation in the target organ, the CNS. The time-dependent increase in MS patients from no overactivation at the beginning of the disease (CIS patients and EAE onset) to elevated NOX activity in RRMS and SPMS patients' PBMCs we observed, in conjunction with data from other groups showing overexpression of NOX subunits in the CNS tissue of progressive MS patients at lesion sites [13] supports the hypothesis that during the course of the disease the immune system (and possibly also CNS components like astrocytes and microglia) develops an "oxidative stress memory". Our findings are furthermore in accordance with data showing that in the chronic phase of the disease oxidized DNA, damaged lipids, and proteins are present in PBMCs of MS patients [21], supporting the proposition that excessive ROS plays a major role in the progressive phase of the disease.

Collectively, these results point to new treatment strategies aiming to reduce oxidative stress in MS. EGCG, the major polyphenolic compound of the green tea plant has been investigated under numerous conditions. Although the molecular mechanisms of its actions are not fully understood [33], there is experimental data pointing to the inhibition of ROS production through EGCG in vitro [63]. Empirically, we showed that EGCG is neuroprotective in EAE, it is known to influence T cell and neuronal function [2, 19, 61] and clinical trials investigating the effects of EGCG (NCT00525668, NCT00799890 and NCT01417312) are ongoing.

In the current study, we demonstrated a direct anti-oxidative mechanism of EGCG on PBMCs of MS patients. Oral treatment with EGCG completely counteracted the chronic NOX overactivation in MS patients, consistent with a higher enzymatic activity, as we could not detect overexpression of NOX2 subunit gp91 by qRT-PCR. Since it is known that EGCG inhibits the binding of NADPH to enzymes within the cell, we observed the mechanism of blocking NADPH binding to NADPH oxidases.

Beside insights into the cellular sources of oxidative stress in EAE and MS, in the CNS and in the periphery, this work demonstrates the unique versatility of intravital NAD(P)H-FLIM as a marker-free method to investigate mechanisms of oxidative stress in inflammatory pathologies, underscoring its intriguing potential for biomedicine as well as clinical research, in a more general context.

Acknowledgments We thank O. Griesbeck for providing the *CerTN L15* transgenic mice, H.J. Fehling for the *Rosa26.tdRFP* transgenic mice and K. Westendorf for providing the *CD4*$^{+}$*.YFP* mouse. We would like to thank E. Gratton and M. Digman for kindly receiving J.P. in the frame of a lab exchange at the University Irvine, CA and for fruitful discussions concerning the detection of oxidative stress by FLIM. We kindly thank R. Günther, N. Asselborn and P. Mex for excellent technical assistance. We are highly grateful to Frank Heppner who provided insight and expertise that greatly assisted the research. Funding: We acknowledge the Deutsche Forschungsgemeinschaft under grant NI 1167/2-1, NI 1167/3-1, NI 1167/4-1 as well as the TRR130 to R.N., H.R. and A.E.H. and the Berlin-Brandenburg School for Regenerative Therapies GSC 203 for H.R. for financial support. This work was partially funded through DFG Exc 257 to F.P. and A.E.H. and TPC4 in FOR 1336 to Jo. P. We declare no competing financial interests.

Open Access This article is distributed under the terms of the Creative Commons Attribution 4.0 International License (http://creativecommons.org/licenses/by/4.0/), which permits unrestricted use, distribution, and reproduction in any medium, provided you give appropriate credit to the original author(s) and the source, provide a link to the Creative Commons license, and indicate if changes were made.

References

1. Agronskaia AV, Tertoolen L, Gerritsen HC (2004) Fast fluorescence lifetime imaging of calcium in living cells. J Biomed Optics 9:1230–1237. doi:10.1117/1.1806472
2. Aktas O, Prozorovski T, Smorodchenko A, Savaskan NE, Lauster R, Kloetzel PM, Infante-Duarte C, Brocke S, Zipp F (2004) Green tea epigallocatechin-3-gallate mediates T cellular NF-kappa B inhibition and exerts neuroprotection in autoimmune encephalomyelitis. J Immunol 173:5794–5800
3. Appaix F, Girod S, Boisseau S, Romer J, Vial JC, Albrieux M, Maurin M, Depaulis A, Guillemain I, van der Sanden B (2012) Specific in vivo staining of astrocytes in the whole brain after intravenous injection of sulforhodamine dyes. PLoS One 7:e35169. doi:10.1371/journal.pone.0035169
4. Balu M, Mazhar A, Hayakawa CK, Mittal R, Krasieva TB, Konig K, Venugopalan V, Tromberg BJ (2013) In vivo multiphoton NADH fluorescence reveals depth-dependent keratinocyte metabolism in human skin. Biophys J 104:258–267. doi:10.1016/j.bpj.2012.11.3809

5. Bedard K, Krause K-H (2007) The NOX Family of ROS-generating NADPH oxidases: physiology and pathophysiology. Physiol Rev 87:245–313. doi:10.1152/physrev.00044.2005
6. Blacker TS, Mann ZF, Gale JE, Ziegler M, Bain AJ, Szabadkai G, Duchen MR (2014) Separating NADH and NADPH fluorescence in live cells and tissues using FLIM. Nat Commun 5:3936. doi:10.1038/ncomms4936
7. Breckwoldt MO, Pfister FM, Bradley PM, Marinkovic P, Williams PR, Brill MS, Plomer B, Schmalz A, St Clair DK, Naumann R et al (2014) Multiparametric optical analysis of mitochondrial redox signals during neuronal physiology and pathology in vivo. Nat Med 20:555–560. doi:10.1038/nm.3520
8. Cheret C, Gervais A, Lelli A, Colin C, Amar L, Ravassard P, Mallet J, Cumano A, Krause KH, Mallat M (2008) Neurotoxic activation of microglia is promoted by a nox1-dependent NADPH oxidase. J Neurosci 28:12039–12051. doi:10.1523/JNEUROSCI.3568-08.2008
9. Choi BY, Kim JH, Kho AR, Kim IY, Lee SH, Lee BE, Choi E, Sohn M, Stevenson M, Chung TN et al (2015) Inhibition of NADPH oxidase activation reduces EAE-induced white matter damage in mice. J Neuroinflamm 12:104. doi:10.1186/s12974-015-0325-5
10. Clausen BE, Burkhardt C, Reith W, Renkawitz R, Forster I (1999) Conditional gene targeting in macrophages and granulocytes using LysMcre mice. Transgenic Res 8:265–277
11. Cooney SJ, Bermudez-Sabogal SL, Byrnes KR (2013) Cellular and temporal expression of NADPH oxidase (NOX) isotypes after brain injury. J Neuroinflamm 10:155. doi:10.1186/1742-2094-10-155
12. Elson D, Requejo-Isidro J, Munro I, Reavell F, Siegel J, Suhling K, Tadrous P, Benninger R, Lanigan P, McGinty J et al (2004) Time-domain fluorescence lifetime imaging applied to biological tissue. Photochem Photobiol Sci 3:795–801. doi:10.1039/b316456j
13. Fischer MT, Sharma R, Lim JL, Haider L, Frischer JM, Drexhage J, Mahad D, Bradl M, van Horssen J, Lassmann H (2012) NADPH oxidase expression in active multiple sclerosis lesions in relation to oxidative tissue damage and mitochondrial injury. Brain 135:886–899. doi:10.1093/brain/aws012
14. Frischer JM, Bramow S, Dal Bianco A, Lucchinetti CF, Rauschka H, Schmidbauer M, Laursen H, Sorensen PS, Lassmann H (2009) The relation between inflammation and neurodegeneration in multiple sclerosis brains. Brain 132:1175–1189
15. Gilgun-Sherki Y, Melamed E, Offen D (2004) The role of oxidative stress in the pathogenesis of multiple sclerosis: the need for effective antioxidant therapy. J Neurol 251:261–268. doi:10.1007/s00415-004-0348-9
16. Grass D, Pawlowski PG, Hirrlinger J, Papadopoulos N, Richter DW, Kirchhoff F, Hulsmann S (2004) Diversity of functional astroglial properties in the respiratory network. J Neurosci 24:1358–1365. doi:10.1523/JNEUROSCI.4022-03.2004
17. Haider L, Fischer MT, Frischer JM, Bauer J, Höftberger R, Botond G, Esterbauer H, Binder CJ, Witztum JL, Lassmann H (2011) Oxidative damage in multiple sclerosis lesions. Brain 134:1914–1924. doi:10.1093/brain/awr128
18. Heim N, Garaschuk O, Friedrich MW, Mank M, Milos RI, Kovalchuk Y, Konnerth A, Griesbeck O (2007) Improved calcium imaging in transgenic mice expressing a troponin C-based biosensor. Nat Methods 4:127–129
19. Herges K, Millward JM, Hentschel N, Infante-Duarte C, Aktas O, Zipp F (2011) Neuroprotective effect of combination therapy of glatiramer acetate and epigallocatechin-3-gallate in neuroinflammation. PLoS One 6:e25456. doi:10.1371/journal.pone.0025456
20. Herz J, Siffrin V, Hauser AE, Brandt AU, Leuenberger T, Radbruch H, Zipp F, Niesner RA (2010) Expanding two-photon intravital microscopy to the infrared by means of optical parametric oscillator. Biophys J 98:715–723
21. Hunter MI, Nlemadim BC, Davidson DL (1985) Lipid peroxidation products and antioxidant proteins in plasma and cerebrospinal fluid from multiple sclerosis patients. Neurochem Res 10:1645–1652
22. Janssen A, Fiebiger S, Bros H, Hertwig L, Romero-Suarez S, Hamann I, Chanvillard C, Bellmann-Strobl J, Paul F, Millward JM et al (2015) Treatment of chronic experimental autoimmune encephalomyelitis with epigallocatechin-3-gallate and glatiramer acetate alters expression of heme-oxygenase-1. PLoS One 10:e0130251. doi:10.1371/journal.pone.0130251
23. Jung S, Aliberti J, Graemmel P, Sunshine MJ, Kreutzberg GW, Sher A, Littman DR (2000) Analysis of fractalkine receptor CX(3)CR1 function by targeted deletion and green fluorescent protein reporter gene insertion. Mol Cell Biol 20:4106–4114
24. Konig K (2000) Multiphoton microscopy in life sciences. J Microsc 200:83–104
25. Kumar S, Alibhai D, Margineanu A, Laine R, Kennedy G, McGinty J, Warren S, Kelly D, Alexandrov Y, Munro I et al (2011) FLIM FRET technology for drug discovery: automated multiwell-plate high-content analysis, multiplexed readouts and application in situ. Chem Phys Chem 12:609–626. doi:10.1002/cphc.201000874
26. Lakowicz JR, Szmacinski H, Nowaczyk K, Johnson ML (1992) Fluorescence lifetime imaging of free and protein-bound NADH. Proc Natl Acad Sci USA 89:1271–1275
27. Lassmann H, Bruck W, Lucchinetti C (2001) Heterogeneity of multiple sclerosis pathogenesis: implications for diagnosis and therapy. Trends Mol Med 7:115–121
28. Lee PP, Fitzpatrick DR, Beard C, Jessup HK, Lehar S, Makar KW, Perez-Melgosa M, Sweetser MT, Schlissel MS, Nguyen S et al (2001) A critical role for Dnmt1 and DNA methylation in T cell development, function, and survival. Immunity 15:763–774
29. Li S, Vana AC, Ribeiro R, Zhang Y (2011) Distinct role of nitric oxide and peroxynitrite in mediating oligodendrocyte toxicity in culture and in experimental autoimmune encephalomyelitis. Neuroscience 184:107–119. doi:10.1016/j.neuroscience.2011.04.007
30. Li Z, Tian F, Shao Z, Shen X, Qi X, Li H, Wang Z, Chen G (2015) Expression and clinical significance of non-phagocytic cell oxidase 2 and 4 after human traumatic brain injury. Neurol Sci Off J Ital Neurol Soc Ital Soc Clin Neurophysiol 36:61–71. doi:10.1007/s10072-014-1909-z
31. Lu F, Selak M, O'Connor J, Croul S, Lorenzana C, Butunoi C, Kalman B (2000) Oxidative damage to mitochondrial DNA and activity of mitochondrial enzymes in chronic active lesions of multiple sclerosis. J Neurol Sci 177:95–103
32. Luche H, Weber O, Nageswara Rao T, Blum C, Fehling H (2007) Faithful activation of an extra-bright red fluorescent protein in "knock-in" Cre-reporter mice ideally suited for lineage tracing studies. Eur J Immunol 37:43–53
33. Mahler A, Mandel S, Lorenz M, Ruegg U, Wanker EE, Boschmann M, Paul F (2013) Epigallocatechin-3-gallate: a useful, effective and safe clinical approach for targeted prevention and individualised treatment of neurological diseases? EPMA J 4:5. doi:10.1186/1878-5085-4-5
34. Miller D, Barkhof F, Montalban X, Thompson A, Filippi M (2005) Clinically isolated syndromes suggestive of multiple sclerosis, part I: natural history, pathogenesis, diagnosis, and prognosis. Lancet Neurol 4:281–288. doi:10.1016/S1474-4422(05)70071-5

35. Murata S, Herman P, Lakowicz JR (2001) Texture analysis of fluorescence lifetime images of nuclear DNA with effect of fluorescence resonance energy transfer. Cytometry 43:94–100
36. Nayernia Z, Jaquet V, Krause KH (2014) New insights on NOX enzymes in the central nervous system. Antioxid Redox Signal 20:2815–2837. doi:10.1089/ars.2013.5703
37. Niesner R, Narang P, Spiecker H, Andresen V, Gericke KH, Gunzer M (2008) Selective detection of NADPH oxidase in polymorphonuclear cells by means of NAD(P)H-based fluorescence lifetime imaging. J Biophys 2008:602639. doi:10.1155/2008/602639
38. Nikic I, Merkler D, Sorbara C, Brinkoetter M, Kreutzfeldt M, Bareyre FM, Bruck W, Bishop D, Misgeld T, Kerschensteiner M (2011) A reversible form of axon damage in experimental autoimmune encephalomyelitis and multiple sclerosis. Nat Med. 17:495–499. http://www.nature.com/nm/journal/v17/n4/abs/nm.2324.html#supplementary-information
39. Nimmerjahn A, Helmchen F (2012) In vivo labeling of cortical astrocytes with sulforhodamine 101 (SR101). Cold Spring Harbor Protoc 2012:326–334. doi:10.1101/pdb.prot068155
40. Nimmerjahn A, Kirchhoff F, Kerr JN, Helmchen F (2004) Sulforhodamine 101 as a specific marker of astroglia in the neocortex in vivo. Nat Methods 1:31–37. doi:10.1038/nmeth706
41. Noseworthy JH, Lucchinetti C, Rodriguez M, Weinshenker BG (2000) Multiple sclerosis. N Engl J Med 343:938–952. doi:10.1056/NEJM200009283431307
42. Noubade R, Wong K, Ota N, Rutz S, Eidenschenk C, Valdez PA, Ding J, Peng I, Sebrell A, Caplazi P et al (2014) NRROS negatively regulates reactive oxygen species during host defence and autoimmunity. Nature 509:235–239. doi:10.1038/nature13152
43. Reinehr R, Gorg B, Becker S, Qvartskhava N, Bidmon HJ, Selbach O, Haas HL, Schliess F, Haussinger D (2007) Hypoosmotic swelling and ammonia increase oxidative stress by NADPH oxidase in cultured astrocytes and vital brain slices. Glia 55:758–771. doi:10.1002/glia.20504
44. Rinnenthal JL, Bornchen C, Radbruch H, Andresen V, Mossakowski A, Siffrin V, Seelemann T, Spiecker H, Moll I, Herz J et al (2013) Parallelized TCSPC for dynamic intravital fluorescence lifetime imaging: quantifying neuronal dysfunction in neuroinflammation. PLoS One 8:e60100. doi:10.1371/journal.pone.0060100
45. Schuh C, Wimmer I, Hametner S, Haider L, Van Dam AM, Liblau RS, Smith KJ, Probert L, Binder CJ, Bauer J et al (2014) Oxidative tissue injury in multiple sclerosis is only partly reflected in experimental disease models. Acta Neuropathol 128:247–266. doi:10.1007/s00401-014-1263-5
46. Shin ES, Park J, Shin JM, Cho D, Cho SY, Shin DW, Ham M, Kim JB, Lee TR (2008) Catechin gallates are NADP+-competitive inhibitors of glucose-6-phosphate dehydrogenase and other enzymes that employ NADP+ as a coenzyme. Bioorg Med Chem 16:3580–3586. doi:10.1016/j.bmc.2008.02.030
47. Siffrin V, Brandt AU, Radbruch H, Herz J, Boldakowa N, Leuenberger T, Werr J, Hahner A, Schulze-Topphoff U, Nitsch R et al (2009) Differential immune cell dynamics in the CNS cause CD4 + T cell compartmentalization. Brain 132:1247–1258 **(pii: awn354)**
48. Siffrin V, Radbruch H, Glumm R, Niesner R, Paterka M, Herz J, Leuenberger T, Lehmann SM, Luenstedt S, Rinnenthal JL et al (2010) In vivo imaging of partially reversible th17 cell-induced neuronal dysfunction in the course of encephalomyelitis. Immunity 33:424–436
49. Sorce S, Krause KH (2009) NOX enzymes in the central nervous system: from signaling to disease. Antioxid Redox Signal 11:2481–2504. doi:10.1089/ARS.2009.2578
50. Srinivas S, Watanabe T, Lin CS, William CM, Tanabe Y, Jessell TM, Costantini F (2001) Cre reporter strains produced by targeted insertion of EYFP and ECFP into the ROSA26 locus. BMC Dev Biol 1:4
51. Stringari C, Edwards RA, Pate KT, Waterman ML, Donovan PJ, Gratton E (2012) Metabolic trajectory of cellular differentiation in small intestine by Phasor Fluorescence Lifetime Microscopy of NADH. Sci Rep 2:568. doi:10.1038/srep00568
52. Stringari C, Nourse JL, Flanagan LA, Gratton E (2012) Phasor fluorescence lifetime microscopy of free and protein-bound NADH reveals neural stem cell differentiation potential. PLoS One 7:e48014. doi:10.1371/journal.pone.0048014
53. Suhling K, Levitt JA, Chung PH, Kuimova MK, Yahioglu G (2012) Fluorescence lifetime imaging of molecular rotors in living cells. J Vis Exp JoVE. doi:10.3791/2925
54. Sumimoto H, Miyano K, Takeya R (2005) Molecular composition and regulation of the Nox family NAD(P)H oxidases. Biochem Biophys Res Commun 338:677–686. doi:10.1016/j.bbrc.2005.08.210
55. van der Goes A, Brouwer J, Hoekstra K, Roos D, van den Berg TK, Dijkstra CD (1998) Reactive oxygen species are required for the phagocytosis of myelin by macrophages. J Neuroimmunol 92:67–75
56. Van der Goes A, Wouters D, Van Der Pol SM, Huizinga R, Ronken E, Adamson P, Greenwood J, Dijkstra CD, De Vries HE (2001) Reactive oxygen species enhance the migration of monocytes across the blood-brain barrier in vitro. FASEB J Off Publ Fed Am Soc Exp Biol 15:1852–1854
57. van der Veen RC, Dietlin TA, Hofman FM, Pen L, Segal BH, Holland SM (2000) Superoxide prevents nitric oxide-mediated suppression of helper T lymphocytes: decreased autoimmune encephalomyelitis in nicotinamide adenine dinucleotide phosphate oxidase knockout mice. J Immunol 164:5177–5183
58. van Horssen J, Schreibelt G, Drexhage J, Hazes T, Dijkstra CD, van der Valk P, de Vries HE (2008) Severe oxidative damage in multiple sclerosis lesions coincides with enhanced antioxidant enzyme expression. Free Radic Biol Med 45:1729–1737. doi:10.1016/j.freeradbiomed.2008.09.023
59. van Horssen J, Singh S, van der Pol S, Kipp M, Lim JL, Peferoen L, Gerritsen W, Kooi EJ, Witte ME, Geurts JJ et al (2012) Clusters of activated microglia in normal-appearing white matter show signs of innate immune activation. J Neuroinflamm 9:156. doi:10.1186/1742-2094-9-156
60. Vladimirova O, Lu FM, Shawver L, Kalman B (1999) The activation of protein kinase C induces higher production of reactive oxygen species by mononuclear cells in patients with multiple sclerosis than in controls. Inflamm Res Off J Eur Histamine Res Soc [et al] 48:412–416
61. Wang J, Ren Z, Xu Y, Xiao S, Meydani SN, Wu D (2012) Epigallocatechin-3-gallate ameliorates experimental autoimmune encephalomyelitis by altering balance among CD4+ T-cell subsets. Am J Pathol 180:221–234. doi:10.1016/j.ajpath.2011.09.007
62. Werner P, Pitt D, Raine CS (2001) Multiple sclerosis: altered glutamate homeostasis in lesions correlates with oligodendrocyte and axonal damage. Ann Neurol 50:169–180
63. Yin S-T, Tang M-L, Su L, Chen L, Hu P, Wang H-L, Wang M, Ruan D-Y (2008) Effects of epigallocatechin-3-gallate on lead-induced oxidative damage. Toxicology 249:45–54. doi:10.1016/j.tox.2008.04.006

frontiers in Immunology

ORIGINAL RESEARCH
published: 14 March 2016
doi: 10.3389/fimmu.2016.00092

Ongoing Oxidative Stress Causes Subclinical Neuronal Dysfunction in the Recovery Phase of EAE

Helena Radbruch[1], Daniel Bremer[2], Robert Guenther[2], Zoltan Cseresnyes[2], Randall Lindquist[2], Anja E. Hauser[2,3] and Raluca Niesner[2]**

[1]Department of Neuropathology, Charité – Universitätsmedizin Berlin, Berlin, Germany, [2]German Rheumatism Research Center (DRFZ) a Leibniz Institute, Berlin, Germany, [3]Immundynamics, Charité – Universiätsmedizin Berlin, Berlin, Germany

Most multiple sclerosis (MS) patients develop over time a secondary progressive disease course, characterized histologically by axonal loss and atrophy. In early phases of the disease, focal inflammatory demyelination leads to functional impairment, but the mechanism of chronic progression in MS is still under debate. Reactive oxygen species generated by invading and resident central nervous system (CNS) macrophages have been implicated in mediating demyelination and axonal damage, but demyelination and neurodegeneration proceed even in the absence of obvious immune cell infiltration, during clinical recovery in chronic MS. Here, we employ intravital NAD(P)H fluorescence lifetime imaging to detect functional NADPH oxidases (NOX1–4, DUOX1, 2) and, thus, to identify the cellular source of oxidative stress in the CNS of mice affected by experimental autoimmune encephalomyelitis (EAE) in the remission phase of the disease. This directly affects neuronal function *in vivo*, as monitored by cellular calcium levels using intravital FRET–FLIM, providing a possible mechanism of disease progression in MS.

Keywords: NOX, EAE/MS, intravital imaging, FLIM–FRET, calcium

OPEN ACCESS

Edited by:
Saparna Pai,
The Centenary Institute, Australia

Reviewed by:
Nathan Karin,
Technion – Israel Institute of Technology, Israel
Anne Kathrin Mausberg,
Heinrich Heine University, Germany

****Correspondence:***
Helena Radbruch
helena.radbruch@charite.de;
Raluca Niesner
niesner@drfz.de

Specialty section:
This article was submitted to Multiple Sclerosis and Neuroimmunology, a section of the journal Frontiers in Immunology

Received: *17 October 2015*
Accepted: *25 February 2016*
Published: *14 March 2016*

Citation:
Radbruch H, Bremer D, Guenther R, Cseresnyes Z, Lindquist R, Hauser AE and Niesner R (2016) Ongoing Oxidative Stress Causes Subclinical Neuronal Dysfunction in the Recovery Phase of EAE. Front. Immunol. 7:92. doi: 10.3389/fimmu.2016.00092

INTRODUCTION

Multiple sclerosis (MS) is a chronic neuroinflammatory disease, with most patients exhibiting a relapsing and remitting course of disease. The neurological damage is a consequence of a mainly T cell-driven immune reaction against myelin in the central nervous system (CNS) (1). Macrophages/microglia, B, and T cells create an acute inflammatory setting, resulting in demyelination and neuronal damage. Most of the patients who experience a second episode develop further relapses. Despite the intensive analysis of the acute immune attack, only little is known about the processes going on at the lesion site after the initial insult (2, 3).

Why and where do new relapses appear? What factors determine the chronicity of a lesion and the course of disease? "Old" lesions appear morphologically inert and are characterized by single perivascular T cells, minimal axonal damage in histological stainings with anti-amyloid precursor protein (APP) antibodies and a dominant fibrotic glial scar (4, 5). In contrast to the progressive disease phase, the inflammatory phase is well modeled by murine experimental autoimmune encephalomyelitis (EAE). In this mouse model using an immunization with MOG_{35-55} peptide, acute clinical signs remit after a few days and mice enter into a chronic phase with or without a residuum of neurological deficits (1). Reactive oxygen species (ROS) generated by invading and resident CNS macrophages have been implicated in mediating demyelination and axonal damage (6–8). In this

study, we address implications of the ceased immune attack for the CNS tissue, beyond the fact that the majority of peripheral immune cells disappeared. In MS patients, we previously detected an ongoing over-activation of NADPH oxidases (especially NOX2) in blood monocytes during remission (8). Using intravital NAD(P)H fluorescence lifetime imaging in mice affected by EAE, during the inflammatory phase (onset and peak of the disease), we detected a massively increased amount of functional NADPH oxidases (NOX1–4, DUOX1, 2) within the CNS as compared to healthy controls (8). Using the same method, we investigated whether functional NADPH oxidases are still present in the CNS after recovery of EAE and, thus, whether oxidative stress is still ongoing in absence of peripheral infiltration of the CNS. We simultaneously monitor calcium concentrations in neurons using intravital FRET–FLIM-based neuronal calcium imaging to evaluate the reaction of the neurons on the altered CNS environment over the course of EAE development and remission. Thereby, we investigate whether in mice with clinical recovery morphologically inert appearing lesions exhibit residual inflammation, as reflected by increased oxidative stress and sub-clinical neuronal dysfunction, in order to better understand mechanisms of chronicity and disease progression in MS and related diseases.

RESULTS

Characterization of the Remission Phase in the CNS of Mice Affected by EAE

The grade of inflammation in brain stem of mice with EAE after clinical recovery (remission) was characterized and compared to animals at the peak of disease and to healthy controls. Our aim was to first characterize peripheral and CNS resident cellular compartments during the remission phase by means of intravital imaging and to corroborate previous results concerning the lack of overt inflammation in this phase.

Characterization of Cellular Markers in the CNS, during EAE Remission

It is widely accepted that in MS, inactive CNS lesions with no signs of immune infiltration are detectable. In our EAE model, some mice show a complete clinical recovery of EAE signs. We characterized these mice by FACS analysis of whole murine CNS (brain and spinal cord) and demonstrated that both monocytes/macrophages ($CD45^{high}CD11b^{+}$ cells) and T cells ($CD45^{high}CD3^{+}$ cells) disappear from the CNS during the remission phase of EAE. Only 7.9 ± 2.8% of the isolated CNS cells were $CD45^{high}CD11b^{+}$ cells (macrophages/monocytes), comparable with healthy controls with 6.2 ± 2.4% (**Figures 1A,B**), whereas their frequency during onset and peak of EAE was previously shown to be strongly increased, to ~50% of the infiltrates (8–10). The majority of cells after EAE recovery were cells with characteristics of microglia: 72.5 ± 3.6% were $CD45^{low}CD11b^{+}$ of which 95.2 ± 6.7% expressed *CX3CR1*. The overlap of *CX3CR1* and tdRFP (LysM) was in both compartments under 5% (3.5 ± 3.2% for $CD45^{high}CD11b^{+}$ cells and 3.5 ± 3.1% for $CD45^{low}CD11b^{+}$ cells). $CD45^{high}CD3^{+}$ cells – typically present during the peak of EAE (11) – mainly disappeared after EAE recovery, constituting only 0.2 ± 0.1% of total cell number. All these findings are in line with the low clinical scores of the mice (between 0 and 0.5; **Table 1**) and are consistent with previous observations of cellular compositions after EAE recovery (10). Our results encompass two independent EAE experiments with a total number of $n = 3$ mice analyzed in remission phase (**Table 1**) and $n = 5$ analyzed healthy mice.

Using intravital microscopy in *CX3CR1*$^{+/-}$ *EGFP* mice ($n = 3$) after EAE recovery, we could show a reduced overlap of 3.6 ± 1.8% between EGFP and i.v. injected sulforhodamin 101 (SR101), which labels astrocytes both in health and in peak EAE (8). These results are similar to the overlap measured in healthy *CX3CR1*$^{+/-}$*EGFP* mice labeled by i.v. injection with SR101 (2.7 ± 1.1% overlap, **Figure 1C**).

Intravital Imaging Reveals Morphologic Features of EAE Remission in the CNS

We performed intravital imaging experiments in the brain stem of *CerTN L15* × *LysM tdRFP* mice (neurons express the Ca^{2+} indicator TN L15, while predominantly *LysM*$^{+}$ phagocytes express tdRFP) and of *CX3CR1*$^{+/-}$ *EGFP* mice (microglia/macrophages express EGFP, while predominantly astrocytes are labeled by SR101).

Infiltration of the CNS by *LysM*$^{+}$ cells is transient, and varies with the stage of disease. In health, practically no *LysM*$^{+}$ cells are present except for few perivascular *LysM*$^{+}$ microglia. During peak of EAE, many *LysM*$^{+}$ cells are present within CNS lesions, and they mostly disappear during the remission phase. We could only identify isolated regions where *LysM*$^{+}$ cells were present inside or in the close proximity to blood vessels or meninges (**Figure 2A**).

In contrast to the peripheral immune cells, the inflammatory-induced gliosis of CNS-resident cells [microglia and astrocytes having phagocytic capacity (8)] persists after EAE recovery (**Figure 2B**). We evaluated shape and function of astrocytes and microglia to test our hypothesis that the function of these CNS cells, in chronic neuroinflammation, has persistently (pathologically) elevated phagocytic features, even in the absence of peripheral immune cells.

First, we quantitatively analyzed the shape of microglia, based on the fact that resting microglia, typical for healthy CNS, are highly ramified, whereas activated microglia, especially those having a phagocytic function, lose their cellular processes and adopt an amoeboid shape. The amoeboid shapes are expected to be found especially in the diseased CNS (10).

We used Fourier coefficients to quantify and reproduce the ramified shape of microglia and to quantify their shape changes in the remission phase as compared to health and peak of the disease. Briefly, single microglia cells were segmented from intravital microscopy data acquired in the brain stem of healthy and EAE mice (in peak and remission phase). Six two-dimensional projections from each three-dimensional object (cell) were generated, and their shape was approximated by overlapping circles as displayed in **Figure 2C**. Each layer of circles is mathematically characterized by a scalar parameter called Fourier coefficient. Thus, the first Fourier coefficient defines the position of a cell, the second defines its dimensions by approximating it with a perfect

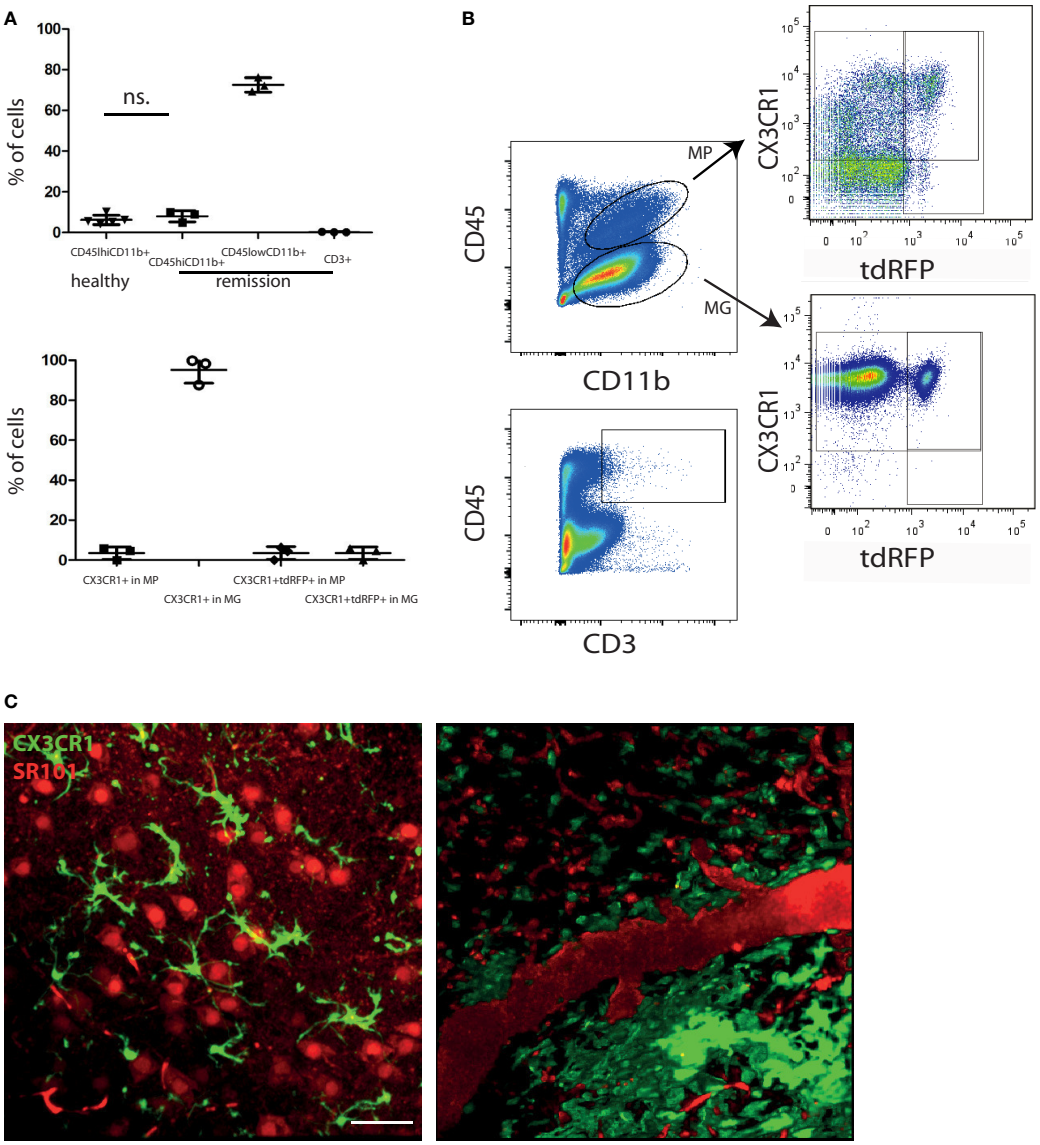

FIGURE 1 | Peripheral immune infiltration of the CNS has largely resolved in the remission phase of EAE. **(A)** FACS analysis of CNS cells after recovery of EAE shows a low immune infiltrate with few monocytes/macrophages (CD45^{high}CD11b^{+}; MP) and CD3^{+} cells. Most of the CD45 expressing cells are CD45^{low}CD11b^{+} (microglia; MG). CD45^{high}CD11b^{+} frequencies are comparable to healthy untreated mice ($n = 5$; ±SD). We applied an unpaired *t*-test to statistically evaluate the results. In the CD45^{high}CD11b^{+} fraction (MP), only few cells express CX3CR1 but most of the cells in the CD45^{low}CD11b^{+} fraction (MG). The overlap of CX3CR1 and tdRFP was comparable in both cell types around 3% ($n = 3$; ±SD, clinical information listed in **Table 1**) **(B)** Exemplarily gating strategy of the FACS analysis of whole CNS in mice after recovery of EAE. **(C)** Projection of 3D intravital fluorescence image in the brain stem of a *CX3CR1*$^{+/-}$ *EGFP* mouse in health and during the remission phase of EAE. The astrocytes (and blood vessels) are labeled by i.v. injected SR101 (red), while the microglia are expressing EGFP (green). Scale bar = 50 μm. The colocalization of the EGFP and SR101 signals, i.e., overlap of the microglial and astrocytic markers, respectively, amounts to 3.6 ± 1.8%.

sphere, and the next Fourier coefficients define the number and length of cellular processes. Each cellular process is approximated by a set of spheres of various diameters, with the center on the surface of the most distant, previous sphere (**Figure 2C**). The higher the ramification and the length of cellular processes, the larger are the relative values of the high-order Fourier coefficients with respect to the second Fourier coefficient. We found a high shape similarity of microglia during the remission phase (118 cells) and of those imaged at the lesion site, at the peak of the disease (57 cells). In comparison to resting microglia in healthy controls (71 cells), the similarity was rather low (**Figure 2D**). The third, fourth, and fifth Fourier coefficients show a significant difference (using an ANOVA test) both in remission and in peak as compared to healthy controls. The results encompass two independent EAE experiments with $n = 3$ healthy controls, $n = 2$ mice at peak EAE, and $n = 4$ mice during the remission phase. The findings of our intravital experiments demonstrate that in remission, after clinical recovery, microglia retain an

TABLE 1 | Mouse strains, EAE data of the mice and mean NOX activation area values within lesions or gliosis/astrogliosis areas with SD per animal (6–20 areas within the brain stem per animal).

EAE ID	Mouse strain	EAE score at analysis time point	Maximum EAE score	Mean NOX activation area (%)	SD
1	CX3CR1.EGFP	1.5	1.5	17.88	5.13
1	CerTN L15 × LysM tdRFP	1.0	1.0	13.20	1.06
1	CerTN L15 × LysM tdRFP	0.5	2.0	8.15	2.25
2	CerTN L15 × LysM tdRFP	2.5	2.5	16.99	9.02
2	CerTN L15 × LysM tdRFP	0.5	1.5	9.91	3.97
3	CerTN L15 × LysM tdRFP	2.0	2.0	10.65	0.51
3	CerTN L15 × LysM tdRFP	2.0	2.0	7.18	1.42
3	CX3CR1.EGFP	1.5	1.5	11.61	1.34
3	CX3CR1.EGFP	0.0	1.5	9.27	3.25
3	CX3CR1.EGFP	0.0	1.0	8.77	3.97
4	CX3CR1.EGFP	0.0	2.0	11.53	5.38
4	CX3CR1.EGFP	0.0	1.5	9.71	2.79
4	CX3CR1.EGFP	0.5	2.0	12.19	4.65
4	CerTN L15 × LysM tdRFP	0.0	2.0	–	–
5	CerTN L15 × LysM tdRFP	0.5	3.5	–	–
5	CerTN L15 × LysM tdRFP	0.5	3.5	–	–
Healthy controls	**Mouse strain**			**Mean NOX activation area (%)**	**SD**
1	CerTN L15 × LysM tdRFP			0.37	0.13
2	C57BL/6			2.84	0.29
3	CerTN L15 × LysM tdRFP			0.47	0.09
4	C57BL/6			0.60	0.28
5	CerTN L15 × LysM tdRFP			2.08	0.91

We included five independent EAE experiments and five healthy controls for the intravital NAD(P)H–FLIM experiments.

activated morphology, suggesting that their function remains predominantly phagocytic despite the fact that clinical symptoms disappeared.

Consistent with the results of shape analysis of microglia, the astrocytic network appears intact in healthy controls ($n = 2$), whereas during peak EAE ($n = 4$) and the remission phase ($n = 3$), it appears disrupted (**Figure 2E**). Additionally, the fine astrocytic processes completely disappear and are replaced by thick perivascular processes, while the astrocytic cell bodies adopt ameboid shapes (**Figure 2E**). A quantification of these observations is rather difficult. Even if a good segmentation of the single astrocytes and their processes is given, currently there is no available mathematical approach or set of mathematical parameters to summarize the complexity of the profound changes of the astrocytic network. However, altogether the observations regarding morphological modifications suggest that the astrocytes are also shifted toward a phagocytic function.

Subclinical Neuronal Dysfunction Correlates with Oxidative Stress without Overt Immune Infiltration after Recovery of EAE

Altered morphology often indicates functional changes, but morphology is not a direct measure of the cellular function. To evaluate alterations in cellular function over the course of EAE, we used intravital NAD(P)H fluorescence lifetime imaging (FLIM), as previously described (8), to detect the over-activation of NADPH oxidases (NOX1–4, DUOX1, 2). As we previously showed in intravital imaging experiments of mice affected by EAE, a concentration of ~200 μM of ROS is detectable in the brain stem, in EAE, using local ROS labeling with Amplex Red. In contrast, in healthy animals, we could not detect any ROS generation. As ROS molecules are highly reactive and diffusive, their detection is limited and the analysis of their cellular source practically impossible. We circumvent this disadvantage by detecting the catalyzer of ROS production, i.e., NOX enzymes, using NAD(P)H–FLIM *in vivo*. We previously showed that high ROS concentration in the brain stem of EAE animals correlates with the over-activation of NOX enzymes as detected by intravital NAD(P)H–FLIM (12). The fluorescence lifetime of NADPH bound to NADPH oxidases is ~3650 ps (12), differing from generally active NADH- and NADPH-dependent enzymes [fluorescence lifetime of NAD(P)H ~2200 ps]. The over-activation of NADPH oxidases is a prerequisite of oxidative stress – known to be one of the main causes of neuronal dysfunction in chronic neuroinflammation (6, 13).

In healthy mice, intravital NAD(P)H–FLIM of the brain stem reveals predominantly metabolic enzyme activity (8). At peak of EAE, the lesion site is associated with vast areas of activated NADPH oxidases, leading to increased oxidative stress (8). Surprisingly, even if overt inflammation and the clinical symptoms disappear, a local activation of NADPH oxidases does not decline to levels found in healthy mice. While the area of NOX enzymes activation in the brain stem of healthy mice amounts in average to 1.8 ± 1.3%, the same average value at peak of the disease significantly increases eightfold to 15.6 ± 5.1% and declines only slightly to 9.4 ± 1% during the remission phase, still over fivefold higher than in healthy mice (**Figures 3A,C**).

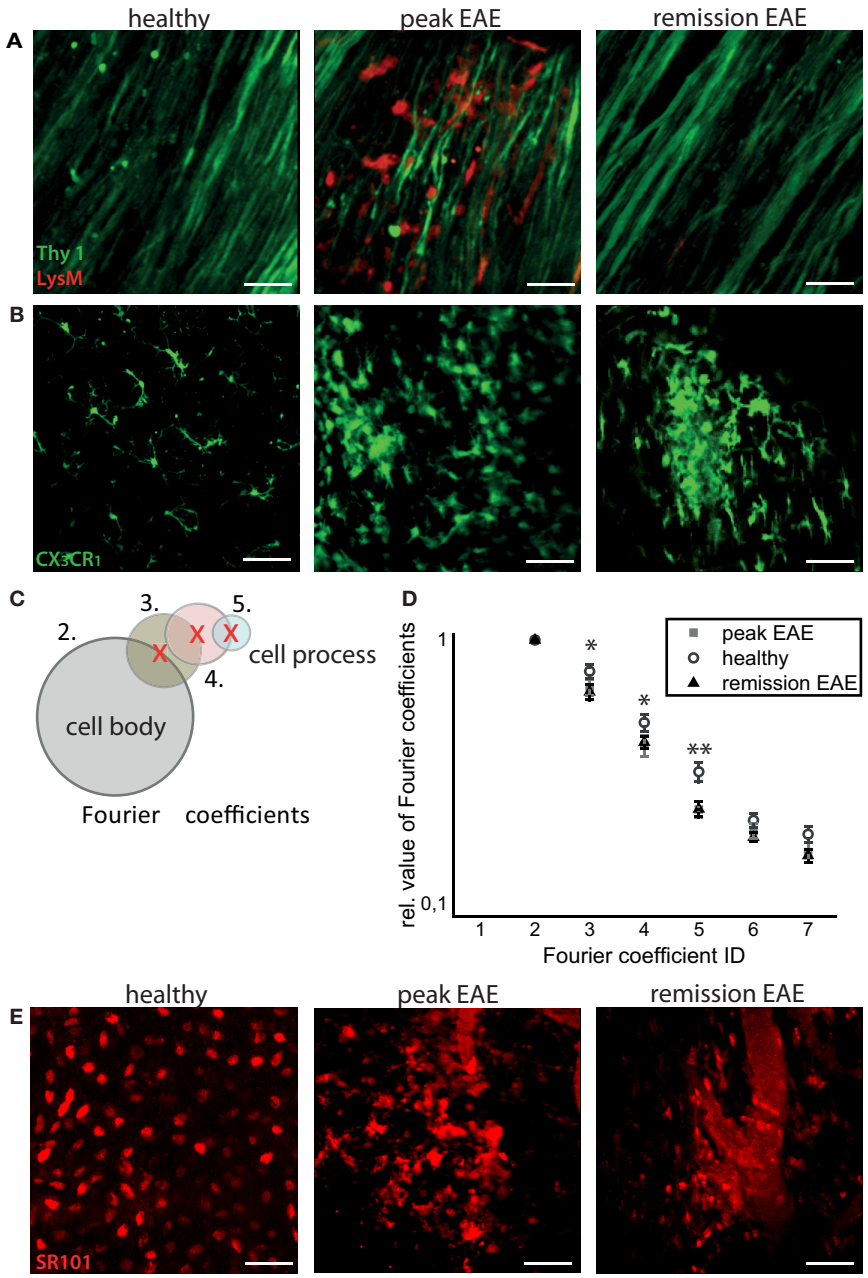

FIGURE 2 | Intravital imaging reveals that remission in EAE correlates with lack of overt immune infiltration, with persisting disruptions of the microglial and astrocytic networks. **(A)** 3D intravital fluorescence images in the brain stem of *CerTN L15* × *LysM tdRFP* mice in health ($n = 5$), at peak EAE ($n = 6$) and in the remission phase ($n = 2$). $\lambda_{exc} = 850 + 1110$ nm, $\lambda_{em} = 525 \pm 25$ nm (Thy1-Citrine in neurons depicted in green), $\lambda_{em} = 593 \pm 20$ nm (LysM tdRFP in phagocytes depicted in red), scale bar = 50 μm. **(B)** 3D intravital fluorescence images in the brain stem of *CX3CR1*$^{+/-}$ *EGFP* mice in health ($n = 3$), at peak EAE ($n = 4$) and in the remission phase ($n = 5$). $\lambda_{exc} = 935$ nm, $\lambda_{em} = 525 \pm 25$ nm (CX3CR1$^{+/-}$ EGFP in microglia/macrophages depicted in green), scale bar = 50 μm. **(C)** Using higher-order Fourier coefficients, we describe the complex shape of microglia. The first Fourier coefficient describes the position of the cells, the second coefficient the sphericity of the cell body and starting from the third Fourier coefficient, the ramification of all cell processes is reproduced: the higher the values of high-order Fourier coefficients with respect to the second Fourier coefficient, the higher the degree of ramification and length of cellular processes of microglia. **(D)** The different shapes of the microglia, shown in **(B)**, were classified in health (71 cells) at peak EAE (57 cells) and in its remission phase (63 cells). The difference between the values of the third, fourth, and fifth Fourier coefficients is significant between healthy controls and remission, but not significant between peak of EAE and remission of EAE. Statistical significance was determined by ANOVA (*$p < 0.05$, **$p < 0.01$, ***$p < 0.001$). **(E)** Projection of 3D intravital fluorescence images in the brain stem of C57/B6 mice i.v. injected with sulforhodamine 101 (SR101) in health ($n = 2$), at peak EAE ($n = 4$) and in the remission phase ($n = 3$). $\lambda_{exc} = 880$ nm, $\lambda_{em} = 593 \pm 20$ nm (SR101 in astrocytes depicted in red), scale bar = 50 μm.

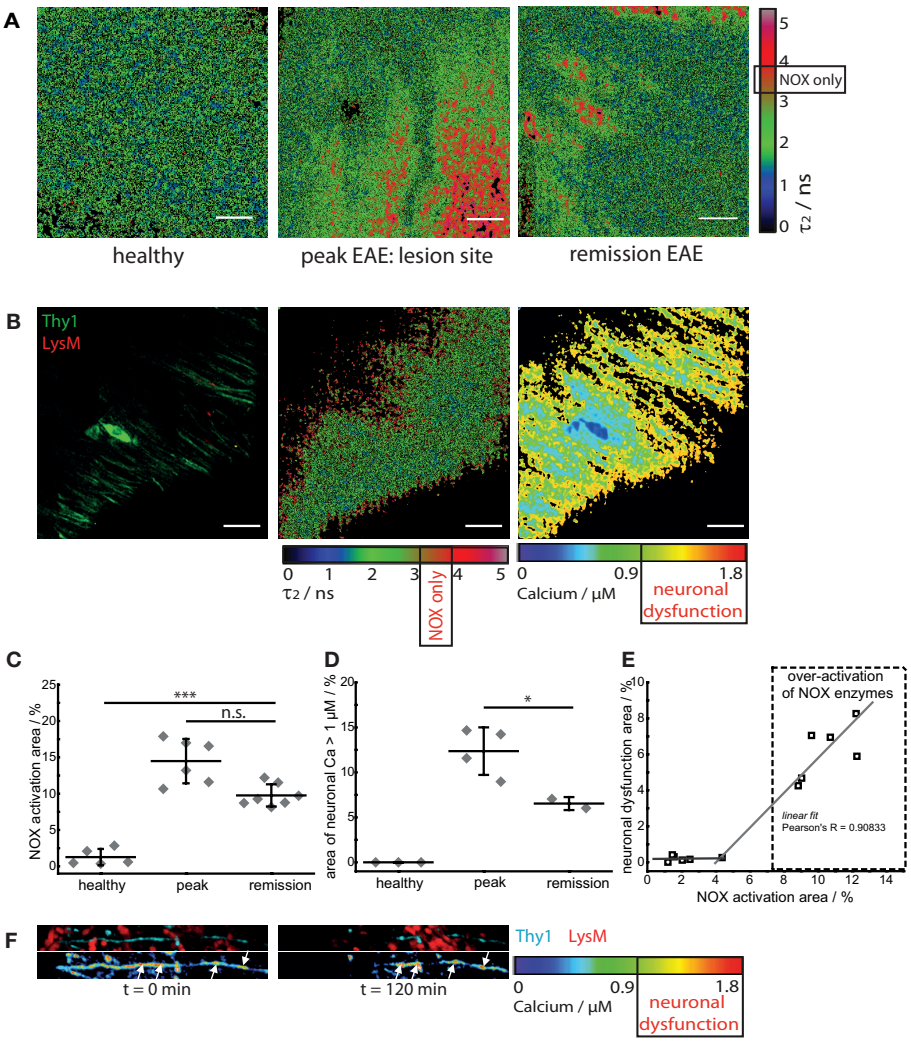

FIGURE 3 | NOX enzymes activation correlates with neuronal dysfunction in the remission phase of EAE. **(A)** τ_2 (enzyme-bound) NAD(P)H–FLIM images acquired in the brain stem of healthy mice ($n = 5$) and of mice affected by EAE at peak of the disease ($n = 6$) and in the remission phase ($n = 7$). The results encompass four independent EAE experiments. Scale bar = 30 µm. **(B)** Intravital fluorescence intensity image, NAD(P)H–FLIM image and FRET–FLIM neuronal calcium image acquired in the brain stem of a *CerTN L15* × *LysM tdRFP* mouse in the remission phase of EAE. Scale bar = 30 µm. **(C)** Quantification of the mean NOX activation area of individual mice at peak EAE ($n = 6$) and in the remission phase ($n = 7$), four independent EAE experiments. While the mean are of NOX activation is strongly increased in the remission phase of EAE as compared to healthy controls, we could observe only a slight decrease of the NOX activation area as compared to peak of EAE (at lesion sites). **(D)** Quantification of the neuronal dysfunction area characterized by a neuronal calcium concentration larger than 1 µM at peak EAE ($n = 4$) and in the remission phase ($n = 2$), two independent EAE experiments. The area of elevated neuronal calcium (area of neuronal dysfunction) is slightly reduced in the remission phase of EAE as compared to the peak of the disease. However, since in healthy controls there is no elevated neuronal calcium, in both phases of EAE, the elevated calcium indicates massive neuronal dysfunction. **(E)** Direct correlation between NOX enzymes over-activation area and neuronal dysfunction area in the remission phase of EAE, within the brain stem ($n = 2$ mice). All images are acquired at 30–150 µm depth within the brain stem (*z*-step = 2 µm). **(F)** Intravital 3D images of the brain stem of a *CerTN L15* × *tdRFP* mouse affected by EAE, at peak of the disease, at an arbitrary time point $t = 0$ and 120 min later. The upper panels show intensity images of axons (cyan, Thy1) and of immune cells (red), whereas the lower images show the corresponding FRET ratio images (Calcium images) of the axons. At the contact sites between axons and immune cells, we observe strongly increased neuronal calcium. After 2 h, at exactly these sites, we observed dramatic morphological changes of the axons, i.e., appearance of ovoid bodies and axonal disruption. The axonal disruption and ovoid bodies formation along the axon is indicated by white arrows in the lower panels of **(F)**. Statistical evaluation in **(C,D)** was determined by ANOVA tests (*$p < 0.05$, **$p < 0.01$, ***$p < 0.001$).

To determine if this increased activation of NAD(P)H oxidases was associated with subclinical neuronal dysfunction, we determined the neuronal calcium level using intravital FRET–FLIM in the brain stem of *CerTN L15* × *LysM tdRFP* mice affected by EAE, as previously described (8, 14, 15). Associated with the persisting oxidative stress, we observed increased neuronal calcium indicating subclinical neuronal dysfunction, and progressing to neuronal damage, within the areas of elevated oxidative stress. The area of measured neuronal dysfunction in the remission phase (6.2 ± 1.7%) is lower than at peak of disease (11.7 ± 2.8%) (16),

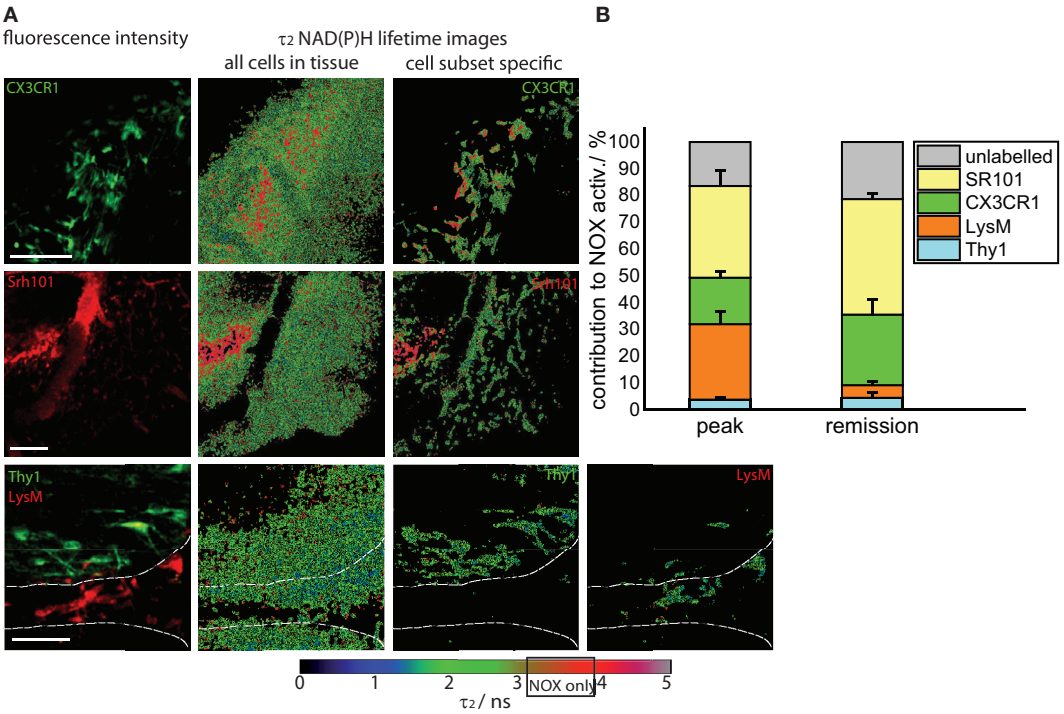

FIGURE 4 | **Cellular origin of oxidative stress in the remission phase of EAE**. **(A)** Intravital fluorescence images and enzyme-bound NAD(P)H fluorescence lifetime images of all cells and of specific cell subtypes acquired in the brain stem of transgenic mice affected by EAE, in the remission phase. We evaluated *CerTN L15* × *LysM tdRFP* mice, in which neurons Thy1 express the calcium indicator TN L15 and LysM$^+$ phagocytes express tdRFP, and *CX3CR1*$^{+/-}$ *EGFP* mice, in which microglia/macrophages express EGFP. Astrocytes were intravitally labeled with sulforhodamine 101 by i.v. injection at least 2 h before imaging. The white lines in the fluorescence and fluorescence lifetime images at the bottom of **(A)** demarcate the outline of a blood vessel. Hence, it becomes obvious that most of *LysM*$^+$ cells reside within the blood vessels, and only few can be found at the border to the CNS parenchyma. Scale bars = 50 μm. **(B)** Contribution of the individual cell subsets to the over-activation of the NOX enzymes in the CNS of mice during the remission phase of EAE (n = 2 CerTN L15 × LysM tdRFP mice – neurons/Thy1 and LysM; n = 5 CX3CR1$^{+/-}$ EGFP mice – microglia/CX3CR1 cells; n = 3 mice labeled with sulforhodamine 101 – astrocytes). The results encompass four independent EAE experiments.

in line with higher scores during peak than in the recovery phase (**Table 1**); however, it is significantly higher than in healthy mice, in which no neuronal dysfunction can be observed using the same approach (**Figures 3B,D**) (14). As depicted in **Figure 3E**, in regions with no or very low over-activation of NOX enzymes (<4% of the total observed area), no neuronal dysfunction can be detected. Beyond this value, the oxidative stress regime is established and neuronal dysfunction linearly increases with increasing area of NOX enzymes activation, within the CNS (Pearson's $R = 0.90883$).

As we and others previously demonstrated, a sustained elevated calcium concentration in neurons, both *in vivo* and in primary neuronal cultures, can precede morphological changes and finally neuronal death. In the brain stem of a *CerTN L15* × *LysM tdRFP* mouse affected by EAE, enhanced contact of axons with peripheral *LysM* cells correlate with an increased calcium baseline in axons (**Figure 3F**). Imaging over 2 h reveals after recovery of EAE sites of increased calcium concentration do not correlate with dramatic morphological changes such as ovoid bodies or even axonal disruption, in contrast to the situation in peak EAE as depicted in **Figure 3F** (white arrows). Since the *TN L15* genetically encoded biosensor reacts slowly to calcium (within few hundred milliseconds), it cannot track the physiologic calcium oscillations typical for neurons, but records only the low average baseline (≈100 nM) (14).

Microglia and Astrocytes Mainly Contribute to Oxidative Stress after EAE Recovery

Next, we elucidated the specific cellular origin of the persistent oxidative stress in the CNS during the remission phase. The approach used in our study – performing endogenous NAD(P)H–FLIM in the CNS of mice with differently fluorescing cell subsets (*LysM*$^+$*tdRFP*, *CerTNL15*, *CX3CR1*$^{+/-}$ *EGFP*, or *SR101* labeled cells) affected by EAE – enables the direct identification of specific cellular origins of oxidative stress by examining colocalization of assembled NOX enzymes acquired via NAD(P)H–FLIM with cellular markers visualized by fluorescence imaging (**Figures 4A,B**).

We quantified the contribution of specific cell types to the total area of NOX enzymes activation in the CNS and found that the mean contribution of *LysM*$^+$ phagocytes amounts to maximally 4.3%, a value comparable to that of neurons (Thy1$^+$ cells, 4.7%).

Whereas the contribution of neurons to the area of oxidative stress generation is, as expected, similar at peak EAE and during the remission phase, *LysM*+ phagocytes proved to be a major source of massive ROS production only during peak EAE but not during the remission, due to their low frequency within the CNS in this phase. Only few perivascular macrophages could be detected (**Figure 4A**, bottom panel) in line with the results of our FACS analysis in **Figure 1A** (5% of the cells are tdRFP expressing) and complementary to **Figure 2A**, in which no LysM tdRFP cell infiltration is shown after EAE recovery. LysM tdRFP cells can are located only in closest proximity to or within blood vessels (marked by white lines in **Figure 4A**) and are, even then, only partially activated (**Figure 4A**, bottom panel right image).

The main contribution to ROS production after recovery in EAE is associated with *CX3CR1*+ cells, i.e., 26%, and astrocytes (SR101), i.e., 45% (**Figure 4B**). Thus, microglia and astrocytes together contribute over 70% of the oxidative stress generation in remission of EAE. Since only in half of the microglia EGFP is detectable by intravital microscopy (heterozygous breeding) and not the entire astrocyte population takes up SR101 [i.e., only half of GFAP+ cells, namely GFAP^{low} (8)], the frequencies of microglia and astrocytes may well be underestimated, and we expect an even higher effective contribution of these cell types to oxidative stress.

DISCUSSION

It is widely accepted that during chronic neuroinflammation, both in the human disease MS and in its murine model EAE, oxidative stress plays a major role in demyelination and neuronal damage (6–8). Most of the findings reported in EAE studies resulted from investigations during the peak of inflammation (17). After peak of disease, in C57BL/6 mice immunized with MOG_{35-55} peptide (7), clinical signs can resolve spontaneously (10, 17) or the mice enter a chronic phase with persistent paralysis (1). This pattern resembles features of the human disease MS, since in its relapsing-remitting phase (RRMS) symptoms are normally self-limiting and patients spontaneously recover.

Despite our knowledge about the dynamic processes of the acute immune response in the CNS, information about the reaction of the tissue after the inflammatory attack is very limited. The processes determining how and where new lesions occur are difficult to study in human tissue as the majority of the samples derives either from very early (biopsies) or very late (post-mortem) lesions. How lesions resolve, how progression takes place, and other characteristics of the later phases of the disease are not well understood (3, 18–20). The alterations of the immune system in MS lesions are obvious, but how this impacts the function of the CNS tissue is almost unknown. Only few inflammatory animal models focus on remyelination as a tissue response, e.g., studies using models of inflammatory cortical demyelination (18, 19).

In this study, we addressed the question of tissue damage regarding oxidative stress as a major detrimental factor for the cells within CNS tissue and consecutive ongoing subclinical neuronal dysfunction after clinical remission of EAE signs. We observed that astrocytes and microglia are shifted toward an activated phenotype, showing both changes in morphology and, even more striking, a high level of activated NADPH oxidases correlating with persisting neuronal elevated calcium levels without evident morphological alterations. Hence, the consequences of sustained neuronal calcium levels after EAE recovery in contrast to peak of EAE are not clear yet (16). Could this be a reason for long-term neuronal damage leading to a progressive disease course in humans?

The role and fate of microglia/macrophages during neuroinflammation is still not well understood (10, 20). From BrdU studies, it was concluded that although microglia enter the cell cycle during acute inflammation, they return to quiescence following remission (21). Furthermore, gene expression analysis of microglia and macrophages suggested that after EAE recovery, these cells return toward homeostasis (10). In contrast, our data demonstrate that at least a subpopulation of microglia is not quiescent and still retains their activated function during remission, as demonstrated by their ameboid morphology and enhanced NOX activity in our model.

The results of our present study indicate that even after remission of the clinical signs, astroglial scars represent areas of ongoing tissue damage, even in the absence of peripheral immune cells. Our findings support the idea of a "trapped" ongoing CNS inflammation as a mechanism of chronic progression in MS (2). At this phase of the disease, astrocytes and microglia alone are a source of persistent oxidative stress locally correlating with ongoing subclinical neuronal dysfunction, as measured by pathologically increased calcium levels in *CerTN L15* × *LysM tdRFP* mice.

Our model provides a useful tool to further investigate the "tissue memory" of neuroinflammatory processes, in order to better understand mechanisms of chronicity and disease progression in MS.

MATERIALS AND METHODS

Two-Photon Laser-Scanning Microscopy

Both fluorescence intensity and FLIM experiments were performed using a specialized two-photon laser-scanning microscope based on a commercial scan head (TriMScope, LaVision BioTec, Bielefeld, Germany). The detection of the fluorescence signals was accomplished either with photomultiplier tubes in the ranges 460 ± 30, 525 ± 25, 593 ± 20 nm or with a 16-channel parallelized TCSPC detector (FLIM-X_{16}, LaVision BioTec, Bielefeld, Germany) in the range 460 ± 30 nm. The excitation of NADH and NADPH was performed at 760 nm (detection at 460 ± 30 nm), of Cerulean (detection at 460 ± 30 nm), SR101 (detection at 593 ± 20 nm), and EGFP (detection at 525 ± 25 nm) at 850 or 880 nm, and of tdRFP at 1110 nm (detection at 593 ± 20 nm).

For both intensity and fluorescence lifetime imaging, we used an average maximum laser power of 8 mW to avoid photodamage. The experimental parameters for FLIM were 160 ps histogram bin [for NAD(P)H–FLIM] and 80 ps histogram bin (for FRET–FLIM) and maximum acquisition time for a 512 × 512 image was 5 s to record a fluorescence decay stack. The time-window in which the fluorescence decays were acquired was set to 9 ns.

Data Analysis

Three-dimensional intravital images acquired within the brain stem of *CX3CR1*$^{+/-}$ *EGFP* mice, either healthy or affected by EAE, at peak and in the remission phase of the disease, were segmented using image analysis software (Imaris, BitPlane, UK). The 3D surfaces of the segmented cells (50–200 cells per condition) were transferred to Fiji/ImageJ and six orthogonal projections were generated for each cell. For each projection of each cell, the Fourier coefficients, describing the sphericity vs. ramification of the cell, were calculated (custom plug-in available in Fiji developed by Zoltan Cseresnyes). All Fourier coefficients corresponding to a single cell were merged following a linear algebraic combination to describe all ramifications of the cell (cell processes). The rank of the Fourier coefficients describes increasingly complex cellular ramifications: whereas the first Fourier coefficient corresponds to the first spherical approximation of the cell, the next coefficients describe increasingly longer processes.

Fluorescence lifetime imaging data analysis was performed using self-written software, as previously described (12, 14). The time-resolved fluorescence signal of NAD(P)H, as acquired by the TCSPC device, was approximated with a bi-exponential decay function (Eq. 1):

$$I_{\mathrm{NAD(P)H}}(t) = \varepsilon + a_1 \times e^{-t/\tau_1} + a_2 \times e^{-t/\tau_2} \quad (1)$$

with ε the background, the 1-indexed term of the sum representing the fluorescence decay of free NADH and NADPH and the 2-indexed term representing the fluorescence decay of enzyme-bound NADH and NADPH. The fluorescence lifetime τ_1 [free NAD(P)H] is 400–450 ps, while the fluorescence lifetime τ_2 of NAD(P)H bound to metabolic enzymes has an average of ~2000 ps. If bound to NADPH oxidases (NOX1–4, DUOX1, 2), NADPH shows a typical fluorescence lifetime of 3650 ps, independent of cell type and even of species, since we repeatedly measured this value in various cell types of humans, mice, and even plants (*Nicotiana tabacum*). We focused all through the manuscript on the fluorescence lifetime τ_2 of the enzyme bound NAD(P)H.

As previously described, we define the area of neuronal dysfunction as the area of free neuronal calcium exceeding a concentration of 1 μM (14). The neuronal calcium concentration was measured *in vivo* using FLIM, in mice expressing the FRET-based calcium biosensor TN L15 in Thy1$^+$ cells. Thereby, the time-resolved fluorescence decay of the donor in the FRET construct (Cerulean) was also approximated by a biexponential function (Eq. 2):

$$I_{\mathrm{Cerulean}}(t) = \varepsilon + a_1 \times e^{-t/\tau_1} + a_2 \times e^{-t/\tau_2} \quad (2)$$

with ε the background, the 1-indexed term representing the fluorescence decay of the FRET-quenched donor and the 2-indexed term representing the fluorescence decay of the unquenched donor. Here, we focused on the ratio $a_1/(a_1 + a_2)$ of the relative concentrations of the FRET-quenched a_1 and unquenched Cerulean a_2, and, using our previously published calibration curve, we determined the absolute calcium concentration within neurons.

Statistical analysis and graphical presentation was carried out with GraphPad Prism 4 (Graphpad Software, USA) and OriginPro (OriginLab, USA). Results are shown as mean values from analyzed data per mouse, in addition the mean ± SD summarize collective data from performed experiments.

Mice

All mice used were on a C57BL/6 background. The *CerTN L15* × *LysM tdRFP* mouse expresses a FRET-based calcium biosensor consisting of Cerulean (donor) and Citrine (acceptor) bound to troponin C, a calcium-sensitive protein present in certain subsets of neurons (22). Additionally, tdRFP is expressed in LysM$^+$ cells. The *CX3CR1*$^{+/-}$ *EGFP* mouse was used to detect microglia (**Table 1**).

EAE Induction

Experimental autoimmune encephalomyelitis was induced as previously described. Briefly, mice were immunized subcutaneously with 150 μg of MOG_{35-55} (Pepceuticals, UK) emulsified in CFA (BD Difco, Germany) and received 200 ng pertussis toxin (PTx, List Biological Laboratories, Inc.) intraperitoneally at the time of immunization and 48 h later. Intravital multi-photon microscopy was performed at different stages of the disease, i.e., peak (3–7 days after appearance of first clinical symptoms) and remission (after decline of clinical symptoms to a score ≤0.5). Mice were randomly picked for analysis. Detailed information about the performed EAE runs and individual scores of the mice are listed in **Table 1**. Mice at peak of disease were part of a previous study of Mossakowski et al. (8) and serve as a reference in this study. We did not included animals that never got sick and at onset analyzed animals.

Preparation of the Brain Stem Window for Intravital Imaging

As previously described, the brain stem was exposed by carefully removing the musculature above the dorsal neck area and removing the dura mater between the first cervical vertebra and the occipital skull bone. The head was inclined for access to deeper brainstem regions and the brain stem superfused with isotonic Ringer solution. Anesthesia depth was controlled by continuous CO_2 measurements of exhaled gas and recorded with a CI-240 Microcapnograph (Columbus Instruments, USA) and by an Einthoven three-lead electrocardiogram (ECG). In order to avoid strong breathing artifacts in the brainstem of anesthetized mice, the ECG signal was correlated to the respiration rate and used as an external trigger for the image acquisition software, which controls the hardware of the microscope setup. Thus, each fluorescence stack was recorded at the same respiration state of the mouse and also in the same tissue region. Animal experiments were approved by the appropriate state committees for animal welfare (G0081/10, LAGeSo – Landesamt für Gesundheit und Soziales) and were performed in accordance with current guidelines and regulations.

FACS Analysis

To isolate cells from the whole brain and spinal cord of *LysM tdRFP* mice, the tissue was homogenized after PBS perfusion, and a percoll gradient was performed according to standard

protocols with 25 and 75% stock istotonic percoll (GE Helthcare) and HBSS. Cells were blocked with antibodies to Fcγ receptors (DRFZ, clone 2.4G2) to avoid non-specific staining, and were subsequently stained with FITC-labeled PerCP-labled rat anti-CD45 (BioLegend) or Cy5- (DRFZ), APC- or Pacific Blue™ (BioLegend)-labeled rat anti-CD11b, in some experiments fixable Viability Dye eFluor®780 (eBioscience), anti-CX3CR1 APC and anti-CD3 Brilliant Violet™ (both BioLegend) were used according to standard procedures, followed by fixation using 4% Paraformaldehyde (Electron Microscopy Science) for 10 min. FACS analysis was performed on a LSR Fortessa (BD).

AUTHOR CONTRIBUTIONS

DB, HR, RN, and RG designed and performed research and analyzed data. DB, HR, RN, and RL wrote the manuscript. HR and RN initiated, organized, and supervised the project. HR and AH provided expertise in mouse handling and intravital imaging and performed EAE experiments (G0081/10). ZC developed algorithms and analyzed data.

ACKNOWLEDGMENTS

We thank O. Griesbeck for providing the *CerTN L15* transgenic mice and H. J. Fehling for the *Rosa26.tdRFP* transgenic mice. We kindly thank R. Günther and P. Mex for excellent technical assistance. We are highly grateful to Frank Heppner who provided insight and expertise that greatly assisted the research.

FUNDING

We acknowledge the Deutsche Forschungsgemeinschaft under grant NI 1167/3-1, NI 1167/4-1 to RN as well as under the TRR130 TP17 and C01 to RN, HR, and AH for financial support. This work was partially funded through the excellence cluster NeuroCure (DFG EXC257) to AH.

REFERENCES

1. Wekerle H. Lessons from multiple sclerosis: models, concepts, observations. *Ann Rheum Dis* (2008) **67**(Suppl 3):iii56–60. doi:10.1136/ard.2008.098020
2. Bradl M, Lassmann H. Progressive multiple sclerosis. *Semin Immunopathol* (2009) **31**:455–65. doi:10.1007/s00281-009-0182-3
3. Stadelmann C, Wegner C, Bruck W. Inflammation, demyelination, and degeneration – recent insights from MS pathology. *Biochim Biophys Acta* (2011) **1812**:275–82. doi:10.1016/j.bbadis.2010.07.007
4. Frischer JM, Bramow S, Dal-Bianco A, Lucchinetti CF, Rauschka H, Schmidbauer M, et al. The relation between inflammation and neurodegeneration in multiple sclerosis brains. *Brain* (2009) **132**:1175–89. doi:10.1093/brain/awp070
5. Frohman EM, Racke MK, Raine CS. Multiple sclerosis – the plaque and its pathogenesis. *N Eng J Med* (2006) **354**:942–55. doi:10.1056/NEJMra052130
6. Fischer MT, Sharma R, Lim JL, Haider L, Frischer JM, Drexhage J, et al. NADPH oxidase expression in active multiple sclerosis lesions in relation to oxidative tissue damage and mitochondrial injury. *Brain* (2012) **135**:886–99. doi:10.1093/brain/aws012
7. Nikić I, Merkler D, Sorbara C, Brinkoetter M, Kreutzfeldt M, Bareyre FM, et al. A reversible form of axon damage in experimental autoimmune encephalomyelitis and multiple sclerosis. *Nat Med* (2011) **17**:495–9. doi:10.1038/nm.2324
8. Mossakowski AA, Pohlan J, Bremer D, Lindquist R, Millward JM, Bock M, et al. Tracking CNS and systemic sources of oxidative stress during the course of chronic neuroinflammation. *Acta Neuropathol* (2015) **130**(6):799–814. doi:10.1007/s00401-015-1497-x
9. Croxford AL, Lanzinger M, Hartmann FJ, Schreiner B, Mair F, Pelczar P, et al. The cytokine GM-CSF drives the inflammatory signature of CCR2+ monocytes and licenses autoimmunity. *Immunity* (2015) **43**:502–14. doi:10.1016/j.immuni.2015.08.010
10. Yamasaki R, Lu H, Butovsky O, Ohno N, Rietsch AM, Cialic R, et al. Differential roles of microglia and monocytes in the inflamed central nervous system. *J Exp Med* (2014) **211**:1533–49. doi:10.1084/jem.20132477
11. Siffrin V, Brandt AU, Radbruch H, Herz J, Boldakowa N, Leuenberger T, et al. Differential immune cell dynamics in the CNS cause CD4+ T cell compartmentalization. *Brain* (2009) **132**:1247–58. doi:10.1093/brain/awn354
12. Niesner R, Narang P, Spiecker H, Andresen V, Gericke KH, Gunzer M. Selective detection of NADPH oxidase in polymorphonuclear cells by means of NAD(P)H-based fluorescence lifetime imaging. *J Biophys* (2008) **2008**:602639. doi:10.1155/2008/602639
13. Schuh C, Wimmer I, Hametner S, Haider L, Van Dam AM, Liblau RS, et al. Oxidative tissue injury in multiple sclerosis is only partly reflected in experimental disease models. *Acta Neuropathol* (2014) **128**:247–66. doi:10.1007/s00401-014-1263-5
14. Rinnenthal JL, Börnchen C, Radbruch H, Andresen V, Mossakowski A, Siffrin V, et al. Parallelized TCSPC for dynamic intravital fluorescence lifetime imaging: quantifying neuronal dysfunction in neuroinflammation. *PLoS One* (2013) **8**:e60100. doi:10.1371/journal.pone.0060100
15. Radbruch H, Bremer D, Mothes R, Günther R, Rinnenthal JL, Pohlan J, et al. Intravital FRET: probing cellular and tissue function in vivo. *Int J Mol Sci* (2015) **16**:11713–27. doi:10.3390/ijms160511713
16. Siffrin V, Radbruch H, Glumm R, Niesner R, Paterka M, Herz J, et al. In vivo imaging of partially reversible th17 cell-induced neuronal dysfunction in the course of encephalomyelitis. *Immunity* (2010) **33**:424–36. doi:10.1016/j.immuni.2010.08.018
17. Moreno B, Jukes JP, Vergara-Irigaray N, Errea O, Villoslada P, Perry VH, et al. Systemic inflammation induces axon injury during brain inflammation. *Ann Neurol* (2011) **70**:932–42. doi:10.1002/ana.22550
18. Denis NL, Wrzos C, Brück W, Stadelmann C, Nessler S. A new mouse model of inflammatory cortical demyelination. *J Neuroimmunol* (2014) **275**(1):119. doi:10.1016/j.jneuroim.2014.08.316
19. Merkler D, Ernsting T, Kerschensteiner M, Bruck W, Stadelmann C. A new focal EAE model of cortical demyelination: multiple sclerosis-like lesions with rapid resolution of inflammation and extensive remyelination. *Brain* (2006) **129**:1972–83. doi:10.1093/brain/awl135
20. Greter M, Lelios I, Croxford AL. Microglia versus myeloid cell nomenclature during brain inflammation. *Front Immunol* (2015) **6**:249. doi:10.3389/fimmu.2015.00249
21. Ajami B, Bennett JL, Krieger C, McNagny KM, Rossi FM. Infiltrating monocytes trigger EAE progression, but do not contribute to the resident microglia pool. *Nat Neurosci* (2011) **14**:1142–9. doi:10.1038/nn.2887
22. Heim N, Garaschuk O, Friedrich MW, Mank M, Milos RI, Kovalchuk Y, et al. Improved calcium imaging in transgenic mice expressing a troponin C-based biosensor. *Nat Methods* (2007) **4**:127–9. doi:10.1038/nmeth1009

Conflict of Interest Statement: The authors declare that the research was conducted in the absence of any commercial or financial relationships that could be construed as a potential conflict of interest.

Copyright © 2016 Radbruch, Bremer, Guenther, Cseresnyes, Lindquist, Hauser and Niesner. This is an open-access article distributed under the terms of the Creative Commons Attribution License (CC BY). The use, distribution or reproduction in other forums is permitted, provided the original author(s) or licensor are credited and that the original publication in this journal is cited, in accordance with accepted academic practice. No use, distribution or reproduction is permitted which does not comply with these terms.

frontiers in Immunology

ORIGINAL RESEARCH
published: 23 December 2016
doi: 10.3389/fimmu.2016.00642

Longitudinal Intravital Imaging of the Retina Reveals Long-term Dynamics of Immune Infiltration and Its Effects on the Glial Network in Experimental Autoimmune Uveoretinitis, without Evident Signs of Neuronal Dysfunction in the Ganglion Cell Layer

OPEN ACCESS

Edited by:
Melanie P. Matheu,
Adheren Immunity, USA

Reviewed by:
Hideki Ogura,
Yale University, USA
Christoph Scheiermann,
Ludwig Maximilian University of Munich, Germany

***Correspondence:**
Raluca Niesner
niesner@drfz.de

Specialty section:
This article was submitted to Inflammation, a section of the journal Frontiers in Immunology

Received: 15 July 2016
Accepted: 13 December 2016
Published: 23 December 2016

Citation:
Bremer D, Pache F, Günther R, Hornow J, Andresen V, Leben R, Mothes R, Zimmermann H, Brandt AU, Paul F, Hauser AE, Radbruch H and Niesner R (2016) Longitudinal Intravital Imaging of the Retina Reveals Long-term Dynamics of Immune Infiltration and Its Effects on the Glial Network in Experimental Autoimmune Uveoretinitis, without Evident Signs of Neuronal Dysfunction in the Ganglion Cell Layer. Front. Immunol. 7:642. doi: 10.3389/fimmu.2016.00642

Daniel Bremer[1], Florence Pache[1,2], Robert Günther[1], Jürgen Hornow[3], Volker Andresen[4], Ruth Leben[1], Ronja Mothes[1,5], Hanna Zimmermann[2], Alexander U. Brandt[2], Friedemann Paul[2], Anja E. Hauser[1,6], Helena Radbruch[5] and Raluca Niesner[1]*

[1] German Rheumatism Research Center, Berlin, Germany, [2] NeuroCure Clinical Research Center, Clinical and Experimental Multiple Sclerosis Research Center, Department of Neurology, Charité – Universitätsmedizin Berlin, Berlin, Germany, [3] Luigs & Neumann GmbH, Ratingen, Germany, [4] LaVision Biotec GmbH, Bielefeld, Germany, [5] Department of Neuropathology, Charité – Universitätsmedizin, Berlin, Germany, [6] Immundynamics, Charité – Universitätsmedizin Berlin, Berlin, Germany

A hallmark of autoimmune retinal inflammation is the infiltration of the retina with cells of the innate and adaptive immune system, leading to detachment of the retinal layers and even to complete loss of the retinal photoreceptor layer. As the only optical system in the organism, the eye enables non-invasive longitudinal imaging studies of these local autoimmune processes and of their effects on the target tissue. Moreover, as a window to the central nervous system (CNS), the eye also reflects general neuroinflammatory processes taking place at various sites within the CNS. Histological studies in murine neuroinflammatory models, such as experimental autoimmune uveoretinitis (EAU) and experimental autoimmune encephalomyelitis, indicate that immune infiltration is initialized by effector $CD4^+$ T cells, with the innate compartment (neutrophils, macrophages, and monocytes) contributing crucially to tissue degeneration that occurs at later phases of the disease. However, how the immune attack is orchestrated by various immune cell subsets in the retina and how the latter interact with the target tissue under *in vivo* conditions is still poorly understood. Our study addresses this gap with a novel approach for intravital two-photon microscopy, which enabled us to repeatedly track $CD4^+$ T cells and LysM phagocytes during the entire course of EAU and to identify a specific radial infiltration pattern of these cells within the inflamed retina, starting from the optic nerve head. In contrast, highly motile $CX_3CR_1^+$ cells display an opposite radial motility pattern, toward the optic nerve head. These inflammatory processes induce modifications of the microglial network toward an activated morphology, especially around the optic nerve head and main retinal blood vessels, but do not affect the neurons within the ganglion cell layer. Thanks to the new technology, non-invasive correlation of clinical scores of

CNS-related pathologies with immune infiltrate behavior and subsequent tissue dysfunction is now possible. Hence, the new approach paves the way for deeper insights into the pathology of neuroinflammatory processes on a cellular basis, over the entire disease course.

Keywords: longitudinal retina imaging, experimental autoimmune uveoretinitis, neuronal calcium imaging, chronic inflammation, multiphoton microscopy

INTRODUCTION

Autoimmunity against compartments of the central nervous system (CNS) can lead to the development of chronic neuroinflammatory diseases, of which multiple sclerosis (MS) is the main representative. Frequently, the very first clinical signs of MS disease course are related to transient loss of vision (1–3). In the case of neuromyelitis optica (NMO), another chronic neuroinflammatory disease with strong involvement of the retina, permanent damage of visual function represents a clinical hallmark (4–6). Thinning of the neuronal retina, i.e., retinal neural fiber layer and the ganglion cell layer (GCL), has been demonstrated using optical coherence tomography (OCT) both in MS and NMO patients (7, 8). Whether this loss of neuronal tissue in the retina is caused by immune infiltration at distal parts of the optic nerve or by a direct immune attack on neuronal retina components remains unclear.

Although experimental autoimmune uveoretinitis (EAU) is not a classical model of neuroinflammation, it mimics CNS autoimmunity within the retina and resembles complementary features of chronic neuroinflammation as compared to experimental autoimmune encephalomyelitis (EAE). Various EAU models in mouse and rat have been developed to highlight the contribution of different immune cell subtypes to autoimmunity in the eye (9). In this study, we use an EAU model with immunization of C57/B6-J mice against the first peptide sequence (1–20) of the interphotoreceptor retinoid-binding protein (IRBP). The latter protein is found in the extracellular space between photoreceptors and the retinal pigment epithelium (RPE). Previous histological studies have shown that in this model autoreactive $CD4^+$ T cells pass the blood–retina barrier, infiltrate the retina, and attract cell subsets of the innate immune system from the periphery and from within the CNS. Presumably, visual loss is caused by retinal tissue degeneration, especially detachment of the photoreceptor layer. This hypothesis is supported by fundoscopy, histology, OCT, and electroretinography results of other studies (10, 11). However, the dynamics of the immune infiltrate and its effects on the function of the neuronal retina, as the central tissue responsible for intact visual function, have not yet been investigated, due to the lack of suitable technologies. In this context, technologies—such as the longitudinal intravital two-photon imaging—are needed, which open the possibility for non-invasive, dynamic 3D image acquisition in the mouse retina.

While two-photon microscopy of retinal whole mounts has already been established and applied to elucidate central questions in neurosciences and neurobiology (12–14), intravital retinal imaging in the mouse has only recently been demonstrated as viable in the context of ophthalmologic diseases (15–17). In studies using the technology, either adaptive optics (16) or a periscope-based setup (18) was used to visualize changes to the RPE in various mouse models. However, the complexity of the optical setup limited the imaging results to single static images.

In this work, we describe a new approach for intravital retinal two-photon imaging and demonstrate its advantages in the context of chronic inflammation in the eye. The main benefit of the approach as compared to established techniques such as OCT, electroretinography (19–21), or scanning laser ophthalmoscopy is its ability to assess cellular motility patterns as well as tissue function and dysfunction over the whole disease course, at cellular and subcellular resolution. Additionally, our setup does not require adaptive or other complex optics, thus, allowing for easy and intuitive use. Employing our intravital retinal imaging approach, we quantified the specific motility pattern of $CD4^+$, $LysM^+$, and $CX_3CR_1^+$ cells in the inflamed retina and observed the morphologic shift within the glial network induced by the immune infiltrate in EAU. No sustained neuronal dysfunction of the ganglion cells associated with sustained increased cellular calcium was detected during the first phase of EAU, in contrast to the results found under similar inflammatory conditions in the brain (22). This finding indicates that the intracellular calcium signaling in the neuronal retina is not primarily affected by the inflammation in our EAU disease model. Although intracellular calcium is generally accepted to be associated with neuronal function and dysfunction, we do not exclude that neuronal retinal dysfunction may appear later during disease course.

RESULTS

Clinical Scoring and Characterization of Cellular Markers during EAU

We employed fundoscopy in C57/Bl6-J mice immunized with IRBP (peptide 1–20) to resume previous findings regarding the clinical symptoms of EAU at the onset and peak of the disease, up to day 28 after immunization and, thus, to validate our experimental setup (**Table 1**). We observed perivascular cellular accumulations (cuffing), changes in the optic disc aspect due to immune infiltration and widening of the main retinal blood vessels (Figure S1A in Supplementary Material), which are previously described hallmarks of the disease (10). Clinical scoring considering these criteria—summarized in **Table 2**—shows an exacerbation of the disease over time ($n = 10$ mice, three independent EAU experiments, Figure S1B in Supplementary Material).

In line with previous reports (9, 10, 19), immunofluorescence and histology (HE) analysis of the retina at peak of EAU corroborated our fundoscopy results. As highlighted by DAPI and

TABLE 1 | Mouse strains and experimental autoimmune uveoretinitis (EAU) experiment code for all mice included in longitudinal multiphoton imaging of the retina.

Mouse strain	Experiment ID
CerTN L15 × LysM tdRFP	EAU-1
CerTN L15 × LysM tdRFP	EAU-2
CerTN L15 × LysM tdRFP	EAU-2
LysM tdRFP	EAU-5
LysM tdRFP	EAU-5
LysM tdRFP	EAU-5
CerTN L15 × LysM tdRFP	Healthy
CerTN L15 × LysM tdRFP	Healthy
CerTN L15 × LysM tdRFP	Healthy
CerTN L15 × LysM tdRFP	Healthy
$CX_3CR_1^{+/-}$ EGFP	EAU-4
$CX_3CR_1^{+/-}$ EGFP	EAU-4
$CX_3CR_1^{+/-}$ EGFP	EAU-4
$CX_3CR_1^{+/-}$ EGFP	Healthy
$CX_3CR_1^{+/-}$ EGFP	Healthy
$CD4^+$ eYFP	EAU-3
$CD4^+$ eYFP	EAU-3
$CD4^+$ eYFP	EAU-3
$CD4^+$ eYFP	Healthy
$CD4^+$ eYFP	Healthy

The mice were also scored by fundoscopy and analyzed at day 28 after immunization using histology and immunofluorescence techniques.

TABLE 2 | Experimental autoimmune uveoretinitis grading criteria in mice with C57BL/6 background adapted from Xu et al. (23).

Score	Optic disc inflammation	Retinal vessels	Retinal tissue
1	Minimal	Engorged vessels	1–4 small lesions
2	Mild	Engorged vessels and 1–4 mild cuffings	>4 small lesions or 2–3 linear lesions
3	Moderate	>4 mild cuffings or 1–3 moderate cuffings	>4 small lesions and >3 linear lesions
4	Severe	>3 moderate cuffings or severe cuffings	Linear lesion confluent

HE staining in cross sections of the eye, the highly ordered retinal layer structure common to healthy controls becomes wave-shaped (Figure S1C in Supplementary Material) and massive immune cell infiltration was found throughout all retinal layers and in the vitreous humor in the EAU mice, but not in healthy controls.

Immunofluorescence analysis showed an increase of $Iba1^+$ cell number, indicating microglial activation. Similarly, the glial fibrillary acidic protein (GFAP) signal (astrocytes) within the GCL increased, indicating astrocytic activation as previously found in the inflamed brain (24) (Figure S1D in Supplementary Material).

Setup for Longitudinal Intravital Multiphoton Imaging of the Mouse Retina

In this study, we present a novel *in vivo* microscopy setup that facilitates the study of immune system dynamics in the retina. The new technology, based on time-lapse multiphoton fluorescence imaging of the retina at subcellular resolution, allows not only quantification of immune infiltration but also monitoring of tissue dysfunction.

Since the eye of the mouse is highly myopic, focusing the excitation laser beam of a multiphoton microscope on the retina is challenging due to spherical aberrations, especially due to third order spherical aberration (25). The mouse eye was modeled as an optical multilens system comprising cornea, aqueous body, lens, vitreous humor, and retina, taking into account typical refractive indexes of the single components and their curvature [**Figure 1A**; (25)]. We found that the spherical aberrations in the myopic mouse eye can be corrected if focusing the excitation beam through a water-immersion objective lens, thus allowing for high-quality imaging of the retina (**Figure 1B**). The use of air objective lenses to image the retina is only possible if using an additional contact lens (in our case, a plano-concave lens, diameter: 3 mm, center thickness: 1 mm, radius of curvature: −1.6 mm, TT Optics GmbH), to correct the spherical aberrations (**Figure 1C**).

In order to avoid damage of the cornea due to dehydration during imaging, we decided to use a water-immersion objective lens in our microscopy setup. The challenge in this respect is the necessity for large working distances of the objective lenses (>4 mm), as the average diameter of the mouse eye at 10 weeks of age is approximately 3.2 mm (25). Additionally, to ensure non-invasive repeated imaging of the same mouse, we avoided direct mechanical contact between cornea and objective lens and limited the image acquisition time to 20 min.

We designed a water-immersion objective lens with a working distance of 6 mm and an effective NA of 0.28 (**Figure 1B**), using nearly the aperture of the mouse eye (0.32) made possible by pharmaceutically widening the pupil (mixture of 2% phenylephrine and 0.4% tropicamide) directly before starting the imaging experiments. The spatial resolution of the 10× air objective (NA = 0.3) was 1.25 μm laterally and 14.1 μm axially at 850 nm excitation wavelength, which allowed visualization of three-dimensional cellular details. Similarly, the resolution of the 4× water-immersion objective (NA = 0.28) was 1.33 μm laterally and 16.3 μm axially after excitation at 850 nm.

In order to find the orientation of the eye during repeated imaging sessions, we developed a positioning stage with two translational and two rotational axes (**Figure 1D**). The mouse was fixed onto this stage using a biocompatible titanium alloy head-post mounted onto the skull 2 weeks prior to performing experiments (**Figure 1D**, inset). The head-post was glued to the skull using dental cement, which ensures high stability of the fixation and does not have any side effects on the mouse. The positioning system additionally contained an inhalation mask, which enables highly accurate control of the anesthesia and, hence, of the eye movement. The mechanical reproducibility of the positioning system using our system was 2 ± 1.5 μm for the translation axes (x and y). The repeated eye positioning under *in vivo* conditions was strongly influenced by the level of animal anesthesia (**Figure 1E**), but does not exceed 10 μm under optimal anesthesia conditions (**Figures 1E**, $N = 100$ repositioning steps). The displacement can be easily corrected using the vasculature of the eye as reference system. In summary, thanks to the positioning system, data were generated at the same imaging position during repeated imaging

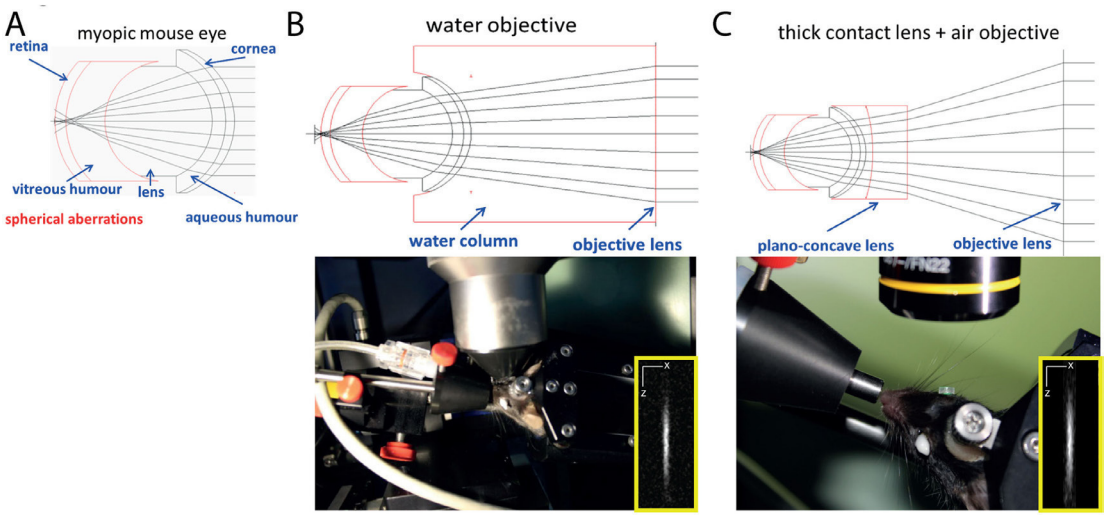

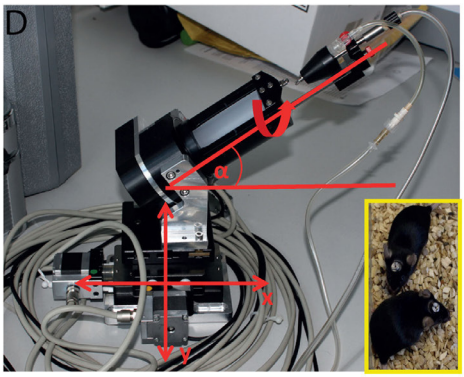

E

isoflurane conc. / %:	1.5	2	3
x displacement / µm:	1.2	7	19.3
y displacement / µm:	1.5	3.3	10.5
displacement / µm:	1.92	7.74	21.97

	rotation axis 1	rotation axis 2
x displacement / µm:	3.78	2.52
y displacement / µm:	2.35	3
displacement / µm:	4.45	3.92
	x translation	y translation
x displacement / µm:	1.75	
y displacement / µm:		3.16
displacement / µm:	3.6	3.6

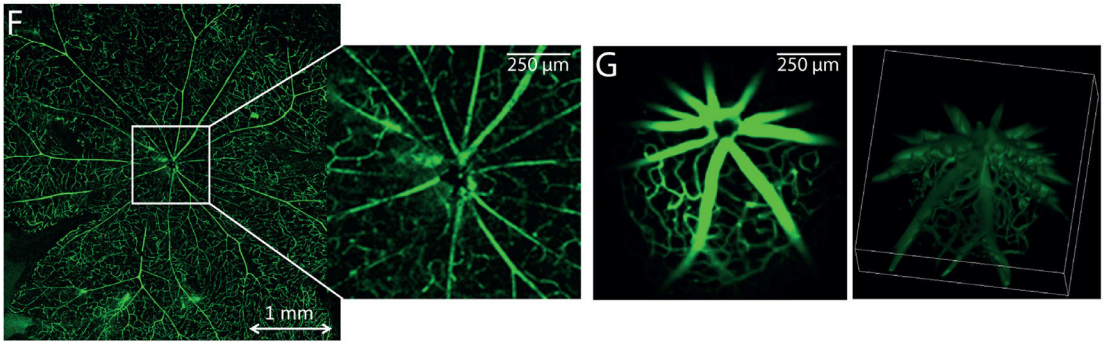

FIGURE 1 | **Longitudinal intravital retinal imaging setup for monitoring cellular dynamics and functions over time**. **(A)** Simulation of the myopic mouse retina shows that spherical aberration hampers focusing on the mouse retina. **(B)** A simple and robust solution, as demonstrated by the simulation in the upper image, is the use of water-immersion objectives with large working distances (touchless imaging). The objective lens used is a 4× magnification water-immersion objective lens, NA = 0.28, and WD 6 mm, as shown during imaging in the lower image. Lateral resolution: 1 µm, axial resolution 11 µm at excitation wavelength 850 nm. **(C)** Simulations of the optical path (upper image) show that using corresponding plan-concave lenses together with an air objective lens also allow focusing onto the mouse retina. We placed a plan-concave lens of 3 mm diameter using hydrogel on the eye of the mouse and focused the excitation beam using a 10× air objective NA = 0.3 and WD 18 mm. The insets show *x* and *z* projections of the point spread function of the system measured on 100 nm fluorescent beads (emission 605 nm), at 850 nm excitation wavelength. **(D)** The mouse positioning system allows translation on three different axis (*x*, *y*, and *z*) and rotation around two axes with a mechanical reproducibility of 2 µm. The fixation on the positioning system is based on a titanium alloy head-post mounted on the skull of the mouse 2 weeks before starting the experiments [inset of **(D)**]. **(E)** The tables overview the positioning reproducibility of the setup in **(D)** during 100 repeated acquisition steps of the vasculature labeled with FITC dextrane, when varying the anesthesia depth given by the isoflurane concentration (upper table) and shifting the rotational axis (middle table) and the translational axis (*x* and *y*, lower table). Comparison of image quality of the retina vasculature (FITC dextrane) as visualized in flat mounts **(F)** and by longitudinal intravital microscopy **(G)**. Whereas the imaging quality is similar, the two-photon microscopy allows for 3D visualization of the central region of 1 mm × 1 mm in the retina.

sessions. This allowed us to compare the data sets acquired at various time points from the same animal. Repeated intravital imaging experiments in healthy CD4+.eYFP, $CX_3CR_1^{+/-}$ EGFP, and CerTN L15 × LysM tdRFP mice—summarized in **Table 1**—using our setup showed no evident signs of either retinal inflammation or calcium-associated neuronal retinal dysfunction, as is often the case of repeated anesthesia, surgery, or mechanical stress during the imaging process (Figure S2 in Supplementary Material).

In order to verify the optical performance of our device, we compared the image of a retinal flat mount with the two-photon image of the retina in a living anesthetized mouse after injection with FITC dextrane for labeling of the vasculature (**Figures 1F,G**). Both imaging methods were able to resolve even fine capillaries with high accuracy, while only the multiphoton imaging restored the curvature of the retina by 3D imaging (Video S1 in Supplementary Material). The effective field of view under *in vivo* conditions reached 1.5 mm × 1.5 mm, which was, as expected, smaller than that of the flat mount.

The key advantage of the multiphoton microscopy is the ability to longitudinally image the retina in living animals, i.e., over weeks, so that the entire disease course can be investigated in a single animal. We also employed our technology to gain novel insight into the pathologic processes during EAU as a model of chronic inflammation in the eye.

Dynamics of Retinal Infiltration with Peripheral Immune Cells in EAU

We performed repeated intravital multiphoton imaging of CD4.eYFP mice during the course of EAU at 7, 11, 14, 21, and 28 days after immunization with $IRBP_{1-20}$. In line with previous immunofluorescence data and with our fundoscopic clinical score, we found an increase in CD4+ T cell number over the course of EAU in all investigated mice (**Figures 2A,B**; $n = 3$ mice, **Table 1**) beginning from day 14 (onset of disease). Longitudinal intravital imaging revealed that CD4+ T cells infiltrated the retina starting from the optic disc and diffused radially. Analysis of the CD4+ cell infiltration in a concentric zonal sectioning of the retina (area I 430 μm diameter, centered the middle of the optic disc, area II 430 to 860 μm diameter, and area III 860 to 1,250 μm diameter) showed that the immune infiltration increases in the peripheral areas and decreases at the optic nerve head during EAU (**Figures 2C,D**). Interestingly, most of CD4+ T cells in the retina are not showing strongly directed displacement during the imaging window of 20 min (**Figures 2E,F,J**); Videos S2 and S3 in Supplementary Material), neither at day 21 nor at day 28 after immunization. At day 14 after immunization, the CD4+ cells were clustered at the optic nerve head and no trajectories could be recorded. The global displacement vector of CD4+ cells at all investigated time points during EAU, describing either centrifugal or centripetal motion, showed no preferential short-term motion of these cells. The mean displacement rate of CD4+ cells infiltrating the retina was reduced as compared to that of CD4+ T cells in the brain stem, during EAE (22). These findings imply that the CD4+ T cell infiltration of the retina, although a highly directed overall process, is rather slow.

Repeated intravital imaging experiments in the retina of LysM tdRFP mice affected by EAU ($n = 4$ mice, **Table 1**, **Figures 2G–I**, Videos S4 and S5 in Supplementary Material) revealed that LysM+ cells (peripheral phagocytes—macrophages, monocytes, and neutrophils) behave similar to CD4+ cells. The LysM+ cells enter the retina at the optic nerve head and the main retinal blood vessels at day 14 after immunization (**Figure 2G**). The time point of their entry was slightly later than that of CD4+ cells, as proportionally less LysM+ cells than CD4+ T cells were found at day 14 after immunization as compared to later time points (days 21 and 28). This observation lends weight to the hypothesis that CD4+ T cells initiate the retinal inflammation in EAU and attract cells of the innate immune system to the eye, e.g., LysM+ cells.

The displacement rates of LysM+ cells were slower than the displacement rates of LysM+ cells in the brain stem of EAE mice, but significantly higher than that of CD4+ T cells in the retina during EAU (***$p < 0.001$, ANOVA statistical evaluation). Interestingly, both the displacement and the displacement rate of LysM+ cells were significantly higher at day 21 than days 28 and 14 (onset EAU) (**Figure 2K**). The global displacement vector for highly motile LysM+ cells in EAU, at days 14 and 21, amounted to 117.1 and 146.8 μm, respectively. This indicates a preferential centrifugal motion, away from the optic nerve. At day 28, the LysM+ cells showed a slight centripetal motion (global displacement vector −34.6 μm).

The typical second harmonics generation signal of highly ordered collagen fibers were not detectable (**Figures 2B,G**) at any point during the EAU course. The collagen fibers typically build the conduits in secondary lymphoid organs and serve as highways for immune cells in the inflamed brain.

Retinal CX_3CR_1 Subset Shifts toward an Activated Morphology and Exhibits Centripetal Motion during EAU

Longitudinal intravital multiphoton imaging of the retina in CX_3CR_1.EGFP mice affected by EAU revealed a change in the behavior of $CX_3CR_1^+$ cells from a probing toward a phagocytic morphology. In healthy controls as well as in mice at days 7 and 11 after immunization (pre-onset), most of the $CX_3CR_1^+$ cells were microglia and had a highly ramified morphology. In contrast, amoeboid cells (phagocytes, mainly activated microglia, and macrophages) appeared, particularly around the vessels and at the optic nerve head, starting from day 14 after immunization, i.e., EAU onset (**Figures 3A,B**) but were practically absent in the parenchyma. Time-lapse imaging after immunization revealed a leaky retinal vasculature in EAU mice, but not in healthy controls, which indicates disruption of the blood–retina barrier (Videos S6–S9 in Supplementary Material). Most $CX_3CR_1^{+/-}$ EGFP cells remained mostly sessile, showing low displacement and reduced displacement rate (**Figures 3C–F**). The values of both displacement and displacement rate of the cells reached a maximum at day 14 after immunization (EAU onset) and were decreased at later time points (days 21 and 28 after immunization, EAU peak). During onset and peak EAU, i.e., in mice having clinical symptoms, these values were significantly higher than during the pre-onset phase (days 7 and 11 after immunization), i.e., in mice

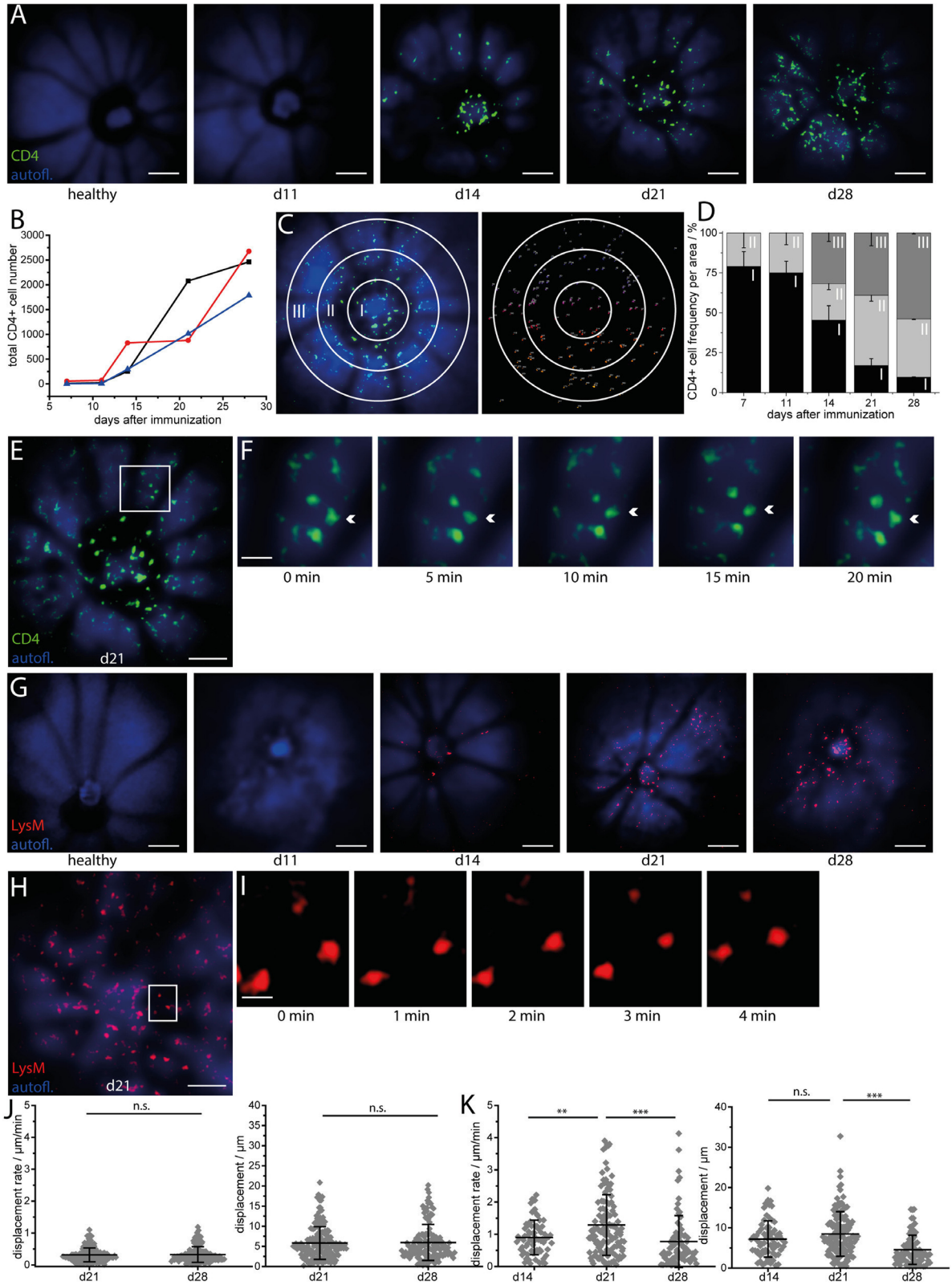

FIGURE 2 | Longitudinal intravital imaging pinpoints CD4+ T cells and LysM+ phagocytes infiltration of the retina as a slow but highly oriented process during experimental autoimmune uveoretinitis (EAU).

(*Continued*)

FIGURE 2 | Continued

(A) Representative three-dimensional projections of fluorescence retinal images (1,400 μm × 1,400 μm × 300 μm) in a healthy mouse and a EAU mouse at days 11 (pre-onset), 14 (onset), 21 (peak), and 28 (peak) during the disease course. Autofluorescence mainly originating from retinol in the retinal pigment epithelium (RPE) is depicted in blue and serves for orientation, since blood vessels and the optic nerve head do not fluoresce and appear as shadows. CD4+ eYFP cells are depicted in green and first appear within the retina at EAU onset (day 14 after immunization), starting from the optic nerve head. λ_{exc} = 960 nm, $\lambda_{detection}$ = 593 ± 20 nm (eYFP), and 525 ± 25 (autofl. retinol). Scale bar = 200 μm. **(B)** Increase of the total number of CD4 eYFP cells in the single mice affected by EAU during the course of the disease (*n* = 3 EAU mice; *n* = 2 healthy mice). **(C)** Representative 3D projection of the retina infiltrated by CD4 eYFP cells at day 21 after immunization and object recognition in the same image, following fluorescence intensity and object size criteria. The white circles define three concentric regions around the optic nerve head (Region I: 0—226 μm; Region II: 226—452 μm; Region III: 452—678 μm from the center of the optic nerve head), in which the cells were counted to quantify the distribution of the CD4+ population in EAU mice. **(D)** Spatial distribution of CD4 eYFP cells within the concentric regions defined in **(C)** during the course of EAU. The infiltration of the retina with CD4+ T cells is a slow but highly oriented process, starting from the optic nerve and spreading toward the retinal edge. Overview retinal fluorescence image of CD4 eYFP cells at day 21 after immunization **(E)** and 20 min time-lapse images of the white square inset **(F)** show that the cells are mostly sessile (Videos S2 and S3 in Supplementary Material). Acquisition rate = 1,400 μm × 1,400 μm × 300 μm *z*-tack/min. Scale bar **(E)** = 200 μm. Scale bar **(F)** = 50 μm. **(G)** Representative three-dimensional projections of fluorescence retinal images (1,400 μm × 1,400 μm × 300 μm) in a healthy mouse and in a mouse affected by EAU at time point days 11 (pre-onset), 14 (onset), 21 (peak), and 28 (peak) during the course of the disease. Autofluorescence mainly originating from retinol within the RPE is depicted in blue and serves for orientation, since blood vessels and the optic nerve head do not fluoresce and appear as shadows. LysM tdRFP cells are depicted in red and first appear within the retina at EAU onset (day 14 after immunization), starting from the optic nerve head and from the main vessels. λ_{exc} = 1,100 nm, $\lambda_{detection}$ = 593 ± 20 nm (tdRFP), and 525 ± 25 (autofl. retinol). Scale bar = 200 μm. **(H)** 3D projection of fluorescence images of LysM + tdRFP cells (red) infiltrating the retina (retinol autofluorescence, blue) at day 21 after immunization. **(I)** Five minutes time-lapse image of the white square inset in **(H)** show that LysM+ cells are also moving only slowly (Videos S4 and S5 in Supplementary Material). Acquisition rate = 1,400 μm × 1,400 μm × 200 μm *z*-tack/min. Scale bar **(H)** = 200 μm. Scale bar **(I)** = 50 μm. **(J)** Displacement and displacement rate of CD4+ T cells within the retina at days 21 and 28 after immunization (*n* = 4 EAU mice, *n* = 4 healthy mice). **(K)** Displacement and displacement rate of LysM tdRFP phagocytes within the retina at days 14, 21, and 28 after immunization. Statistical evaluation was determined by ANOVA one-way tests and Bonferroni *post hoc* test for multicolumn analysis (*$p < 0.05$, **$p < 0.01$, and ***$p < 0.001$).

showing no clinical signs. The small population of $CX_3CR_1^+$ cells showing significant displacement (>10 μm) moved exclusively in the perivascular space of main retinal vessels (**Figure 3D**; Videos S6–S9 in Supplementary Material) in both healthy controls and mice affected by EAU. Their mean displacement rate (9.55 ± 2.63 μm/min in healthy controls and 10.55 ± 4.80 μm/min mice affected by EAU) was similar to that measured for CD4+ cells moving within the perivascular space, in the brain stem of mice affected by EAE (26). The displacement vectors of all motile cells were summed up in healthy and EAU-affected mice, respectively, to determine the global displacement vector with respect to the optic nerve head for each condition (**Figure 3G**). In healthy mice, the displacement of the $CX_3CR_1^{+/-}$ EGFP cells was not directional (**Figures 3F,G**), suggesting that cells are not preferentially moving toward or away from the optic nerve. In EAU, most of the motile cells moved centripetally, toward the optic nerve (**Figures 3G,I**), as revealed by the global displacement vector oriented toward the optic nerve head. This implies that a subset of $CX_3CR_1^+$ cells were activated within the retina and migrated through the optic nerve head, probably gaining access to inner parts of the CNS.

In order to determine the directionality of $CX_3CR_1^+$ cells relative to the optic nerve, we calculated the vectors defined by the optic nerve head and the starting and end point of the cell trajectory, respectively, for each motile $CX_3CR_1^+$ cell (**Figure 3H**). The vector sum of these two vectors projected on one dimension results in the displacement vector toward or away from the optic nerve (**Figure 3H**) for each cell.

Longitudinal Calcium Imaging Reveals No Evident Signs of Calcium-Associated Neuronal Retinal Dysfunction during Onset and Peak of EAU

As previously demonstrated by us and others, sustained elevated calcium levels in neurons, i.e., 1 μM intracellular calcium over an hour, lead to strong morphological changes and ultimately to neuronal death, both in primary neuronal cultures and under *in vivo* conditions (22, 24). We have shown that enhanced contact of axons with peripheral immune cells in the brain stem of mice affected by EAE correlates with an increased calcium baseline in axons (22, 24, 27). Since the *TN L15* construct reacts slowly to calcium, over hundreds of milliseconds, it is able to specifically track only long-lasting increases of intracellular calcium. Thereby, it reports non-physiological, lasting elevations of the intracellular calcium concentration, but not the physiologic calcium oscillations within neurons. Under physiologic conditions, the construct records only the low average baseline (≈100 nM) (27). In CerTN L15 mice mainly the ganglion cells, which expressed Thy1 (28), encode the *TN L15* construct as we demonstrated by immunofluorescence analysis (Figure S3 in Supplementary Material).

Repeated neuronal calcium measurements in CerTN L15 mice affected by EAU revealed a significant increase of neuronal calcium in the GCL at day 21 after immunization as compared to the pre-onset phase (days 7 and 11 after immunization) and onset phase (day 14 after immunization), which faded at day 28 after immunization (**Figures 4A–C**; Videos S10–S12 in Supplementary Material). This result may reflect a sustained pathology of the retina, as previously shown in other organs of the CNS. However, despite strong immune infiltration with CD4+ and LysM+ cells, as well as alterations of the microglial network toward an activated morphology, the increase of neuronal calcium in the retina of EAU mice did not reach the typical intracellular calcium level of pathologic neuronal dysfunction found in the brain stem of mice affected by EAE under qualitatively similar immune infiltration conditions (24). Moreover, the neuronal calcium levels were similar in all cells within the concentric areas I–III around the optical nerve head and did not increase during the imaging period of 20 min (**Figures 4B,D**) at any stage of the disease. Hence, retinal inflammation at the onset and peak of EAU

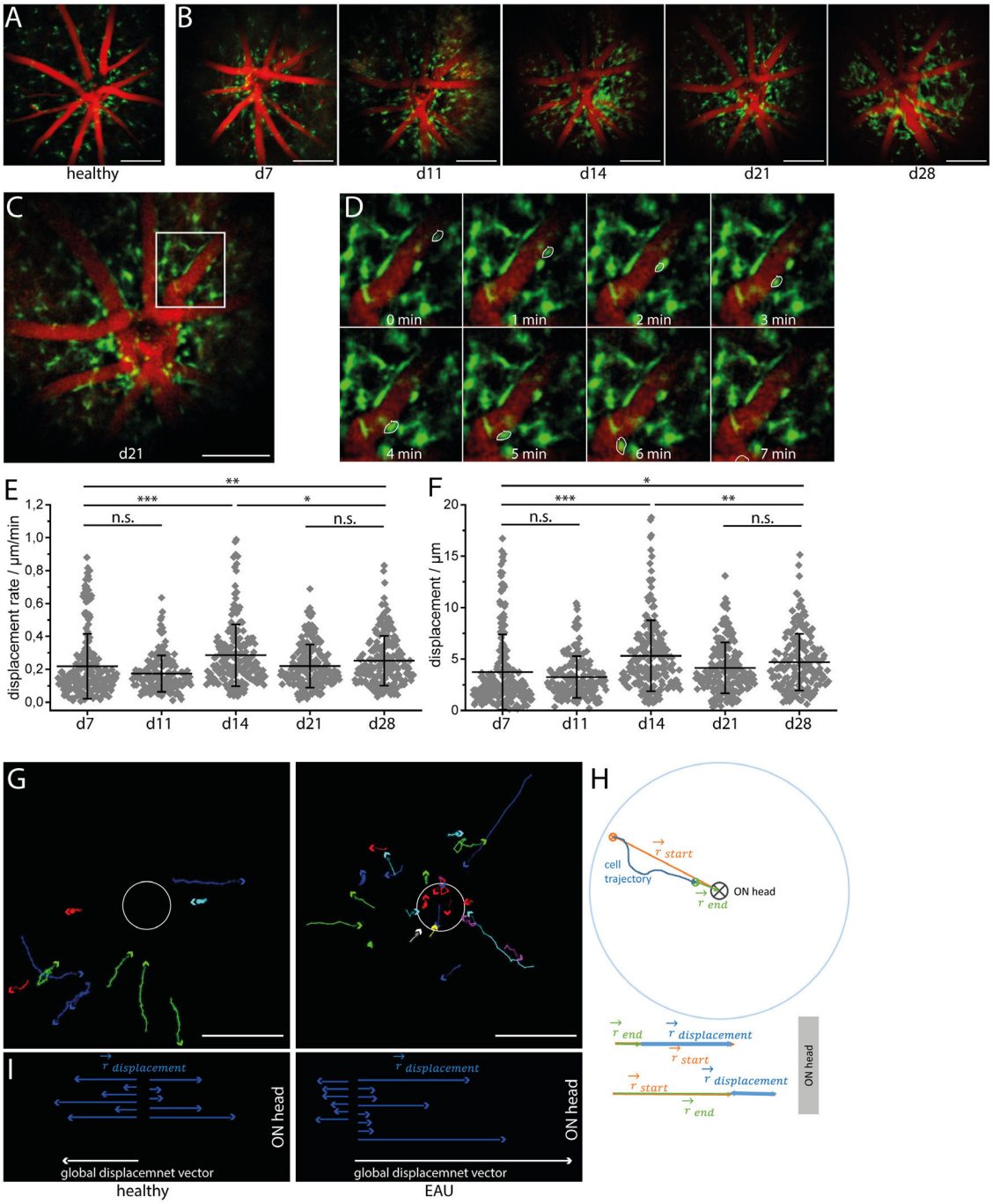

FIGURE 3 | CX_3CR_1 cell subset shifts toward an activated morphology and shows preferential centripetal motion during experimental autoimmune uveoretinitis (EAU). Sample three-dimensional projections of fluorescence retinal images (1,400 µm × 1,400 µm × 300 µm) in a healthy mouse **(A)** and in a $CX_3CR_1^{+/}$eGFP mouse affected by EAU at time points days 7 (pre-onset), 11 (pre-onset), 14 (onset), 21 (peak), and 28 (peak) during the course of the disease **(B)**. Blood vessels are labeled by rhodamine (red) and $CX_3CR_1^{+/-}$ eGFP microglia/macrophages are shown in green. During EAU, some CX_3CR_1 cells shifted from the typical resting microglial morphology toward an amoeboid morphology, which is typical for the phagocytic phenotype. λ_{exc} = 850 nm, $\lambda_{detection}$ = 525 ± 25 nm (eGFP), and 593 ± 20 (rhodamine). *z*-step = 15 µm. Scale bar = 200 µm. Overview **(C)** and corresponding time-lapse of 3D projections of fluorescence images of CX_3CR_1 eGFP cells and of the vasculature in white square inset within the retina **(D)** over 20 min. Acquisition rate = 1,400 µm × 1,400 µm × 300 µm/min. *z*-step = 15 µm. The depicted CX_3CR_1 cell (white outline) is moving within the perivascular space with a speed of 31 µm/min. **(E)** Displacement rate and displacement of $eGFP^+$ cells during the course of EAU at days 7, 11, 14, 21, and 28 after immunization (n = 3 EAU mice, n = 2 healthy controls). **(F)** Tracks of cells showing a displacement larger than 20 µm over 20 min in healthy mice and mice affected by EAU. Scale bar = 200 µm. **(G)** Displacement vectors of single motile cells toward/away from the optic nerve head and the global displacement vector for each situation: health and EAU. **(H)** Principle of assessing the displacement vector toward/away from the optic nerve head for single cells. Statistical evaluation was determined by ANOVA one-way tests and Bonferroni *post hoc* test for multicolumn analysis (*$p < 0.05$, **$p < 0.01$, and ***$p < 0.001$).

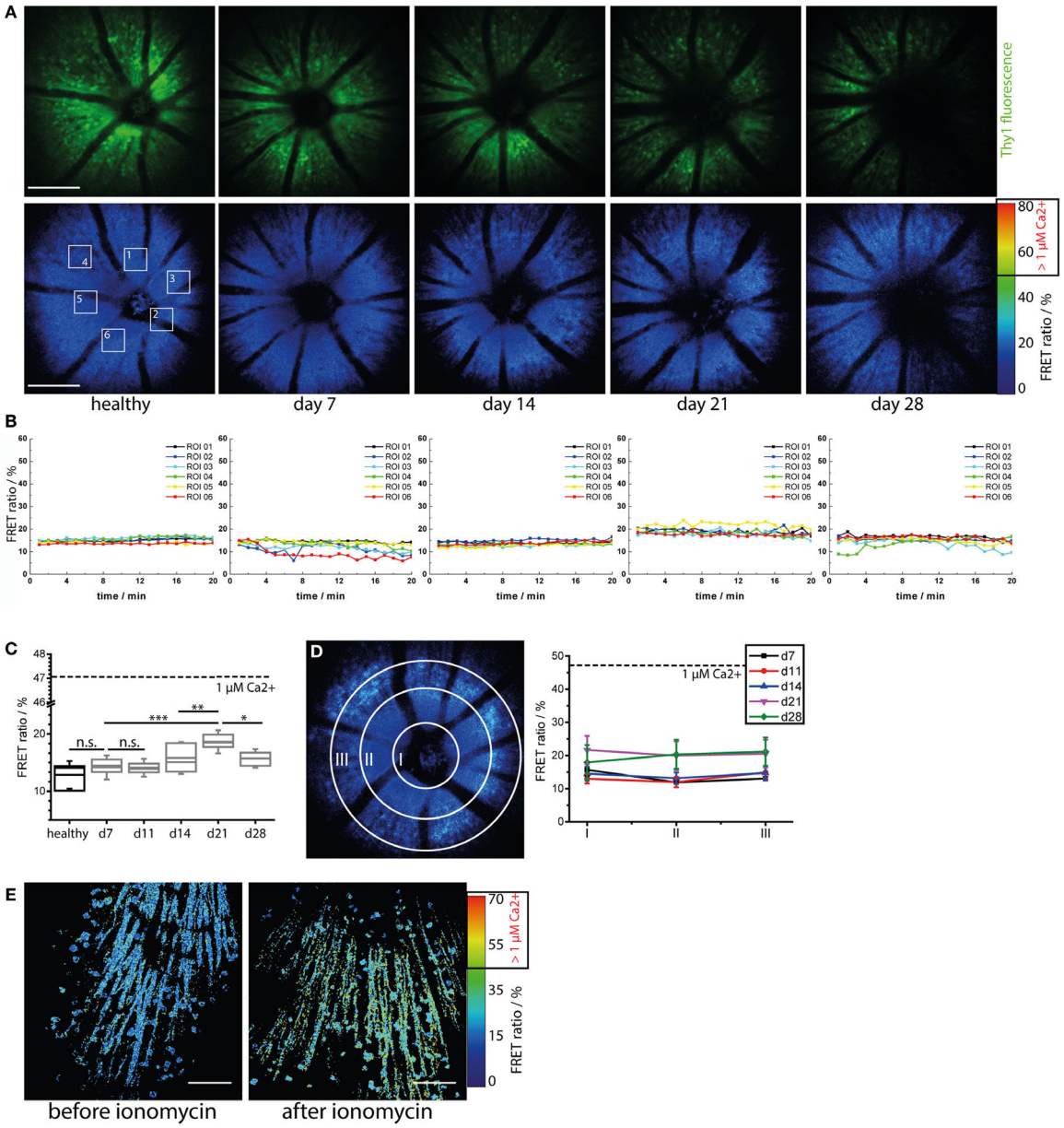

FIGURE 4 | **Immune infiltration and microglial activation do not lead to calcium-associated neuronal dysfunction in the retina during onset and peak of experimental autoimmune uveoretinitis (EAU)**. **(A)** Representative three-dimensional projections of fluorescence retinal images (upper row) and FRET ratio images (lower row) of 1,400 µm × 1,400 µm × 300 µm in a healthy and in a *CerTN L15* mouse affected by EAU at time point days 7 (pre-onset), 14 (onset), 21 (peak), and 28 (peak) during the course of the disease. TN L15, a FRET-based Ca-sensor, is genetically encoded in neurons and expressed under the Thy1 promoter. The sensor contains Troponin C as Ca-sensitive protein and Cerulean and Citrine as FRET-donor and FRET-acceptor molecules, respectively. The FRET ratio, which scales with the intracellular calcium concentration, does not change during the course of EAU. λ_{exc} = 850 nm, $\lambda_{detection}$ = 466 ± 30 nm (Cerulean), 525 ± 25 nm (Cerulean, Citrine), and 593 ± 20 (Citrine). *z*-step = 15 µm. Scale bar = 200 µm. **(B)** Time courses of the mean FRET ratio within the marked regions of interest (1–6) over 20 min for all time points depicted in **(A)**. No changes in the neuronal calcium was observed during the imaging time period, indicating that our two-photon microscopy of the eye did not disturb tissue function and is a reliable probe for identifying possible physiologic or pathologic changes.
(C) Quantification of the mean FRET ratio of the whole imaged volume in the retina in healthy and in mice affected by EAU at different phases of the disease (n = 3 healthy mice, n = 4 EAU mice, two independent EAU experiments). The mean FRET ratio indicative for neuronal calcium increases transiently up to day 21 after immunization (peak EAU) but remains under the boundary of neuronal dysfunction (1 µM calcium, corresponding to 47% FRET ratio). **(D)** Adopting the same principle of concentric segmentation of the retina around the optic nerve head as in **Figure 2** the mean FRET ratio in the Regions I–III was quantified for each measured time point after immunization, in all *CerTN L15* mice affected by EAU. In contrast to the immune infiltrate, which shows directed concentric spreading kinetics starting from the optic nerve head, the neuronal calcium shows an almost constant value all over the imaged retinal volume during both onset and peak EAU. **(E)** The retina of a healthy *CerTN L15* treated with ionomycine (40 µM) for 5 min shows increase of neuronal calcium above the threshold of neuronal dysfunction, i.e., 1 µM intracellular calcium corresponding to 47% FRET ratio. Statistical evaluation was determined using ANOVA one-way tests and Bonferroni *post hoc* test for multicolumn analysis (*p < 0.05, **p < 0.01, and ***p < 0.001).

(up to day 28 after immunization) did not correlate temporally or spatially with neuronal tissue dysfunction related to calcium signaling and did not appear to primarily target the neuronal retina (GCL). We cannot exclude that neuronal dysfunction may develop independently of a disturbance of intracellular calcium, in which case our approach would fail. Furthermore, although we found in our experiments that the maximum neuronal calcium increase is reached at day 21 after immunization, repeated imaging experiments using our approach during the chronic phase of EAU (e.g., between days 28 and 60 after immunization) would shed light on possible delayed effects of inflammation on the neuronal retina.

As we did not observe any pathologic increase of neuronal calcium during the time-lapse imaging experiment (20 min, **Figure 4B**; Figure S2C in Supplementary Material), we conclude the retina of healthy and EAU mice are not functionally affected by exposure to the focused laser beam of the multiphoton microscope. Moreover, we were able to induce calcium-associated neuronal dysfunction and damage in the retina, i.e., FRET ratio of up to 70% corresponding to neuronal calcium of 3 μM, by local application of ionomycine 40 μM in healthy CerTN L15 mice (**Figure 4E**). Hence, our approach can reliably quantify calcium-associated functional state in retinal neurons. Furthermore, we confirmed in this way that distorted calcium signaling in retinal neurons during onset and peak of EAU is only a minor aspect of the disease.

DISCUSSION

As the only part of the CNS exposed to the outer environment, the eye is the ideal candidate for non-invasive intravital imaging of autoreactive attacks of the immune system on the CNS, typical for chronic neuroinflammatory pathologies. Independent of the specific CNS region being the direct target of the immune attack, the clinical involvement of the neuronal retina has been demonstrated in various contexts of neuroinflammation. Accordingly, the thinning of the GCL and of the retinal neuronal fiber layer are well described in MS and NMO and represent promising diagnostic approaches to evaluate the disease course (29). On the other hand, models of autoimmunity in the mouse eye are particularly relevant to understand the pathological mechanisms of neuroinflammation. They are necessary to evaluate the relation between brain and retinal inflammation and, thus, to take full advantage of the eye as a window to the CNS.

Multiphoton microscopy allows unique access to information on cellular dynamics within living organisms beyond the information on cellular composition and morphological tissue changes provided by static histology. Up to now, the technology has been widely used to elucidate basic physiologic processes as well as patho-mechanisms in various organs and disease models (30–32). In the context of neuroinflammation, which involves highly dynamic, tissue-dependent processes, the relevance of intravital multiphoton microscopy as a central investigation tool becomes obvious. Moreover, since neuroinflammatory processes are lasting days, weeks, or even months, whereas typical imaging time-windows in intravital microscopy are several hours, technologies allowing for repeated imaging in one and the same animal are requested. The potential of retinal two-photon imaging has been underlined by several recent publications (16, 18); however, to our knowledge, this is the first report demonstrating repeated time-lapse imaging of the retina, allowing us to monitor cellular dynamics, cellular interactions, and tissue function longitudinally in one mouse. Our approach reduces the number of animals needed for experiments and decreases inter-individual variance due to different responses to immunization across mice. Tissue and even cellular fate can be tracked over weeks and seemingly static processes are revealed as slow but dynamic.

Using our novel approach, we found dramatic differences in the motility behavior of effector cells—$CD4^+$ T cells and phagocytes ($LysM^+$ cells)—in the eye compared to the brain stem and spinal cord under comparable inflammatory conditions. In the brain stem and spinal cord, effector cells from the periphery moved directionally and rather rapidly (5–7 μm/min), especially along *de novo* built collagen fibers, similarly to their movement within secondary lymphoid organs (33). They enter the immune-privileged brain tissue *via* meninges or leaky blood vessels and accumulate at lesion sites (22, 33). In the eye, these cell subsets show a reduced displacement rate (approximately 1 μm/min). However, during the course of the disease (days to weeks), they move in a highly directed manner from the optic nerve head toward the retinal periphery. In line with this finding, we could not detect the collagen fibers characterized by second-harmonic generation at any time point, although they have previously been shown in imaging studies of the CNS (33) and of lymphoid organs to be used for directed cell movement.

Confirming previous findings, we observed that $CD4^+$ T cells invaded the retina slightly earlier than $LysM^+$ cells (phagocytes) and presumably initiate the inflammation. The immune infiltration typically began at the head of the optic nerve head, indicating cell migration from inner areas of the CNS through the optic nerve as a main pathway of retinal infiltration next to the immune infiltration through the disrupted blood–retina barrier. Interestingly, $CD4^+$ T cells are significantly slower than $LysM^+$ cells during the whole course of EAU. Considering the lack of collagen fibers in the inflamed retina, a possible explanation of this observation is that $CD4^+$ T cells depend on the collagen fibers as highways facilitating their movement stronger than $LysM^+$ cells do.

Taken together, our findings lead to the hypothesis that the $CD4^+$ T cells, as initiators of the retinal inflammation, are locally reactivated directly at the optic nerve head and not within the perivascular space, as we do not see a compartmentalization to the retinal vasculature, unlike in the inflamed brain (26). Moreover, we hypothesize that $LysM^+$ cells attracted to the retina by CD4 T cells deliberately search for tissue-specific targets for a direct attack, as they show invasive migration patterns similar to those in the brain.

Which CD4 T cells subsets, e.g., Th17 or Th-GMCSF cells, are relevant for the induction of autoimmunity in the eye, and how do they dynamically interact with the retina and with antigen presenting cells? What role do other cellular subsets, such as CD8 T cells and other soluble factors (e.g., CXCL12 or TNFα), play

in this context? These are still open questions to be addressed in future studies.

In terms of pathological changes in the CNS compartments during neuroinflammation, a shift of the microglial network from a probing toward an activated morphology revealed the same local signs of gliosis previously described in the brain stem and spinal cord (34). In contrast to the results of intravital imaging studies of the inflamed brain (35, 36), phagocytic $CX_3CR_1^+$ cells (characterized by amoeboid shape) only moved rapidly in the perivascular space of the inflamed eye, probably because there were no conduits to orient their motion in the retinal parenchyma. Which factors inhibit or trigger the conduits for immune cells in the CNS is not yet known. Interestingly, during inflammation the $CX_3CR_1^+$ cells move perivascularly toward the optic nerve head, implying that cell immigration can be initiated in the eye during neuroinflammation and that the cells then move on *via* the optic nerve toward the inner regions of the CNS. This suggests that the fiber tracks of the optic nerve can act as a bidirectional highway for migrating cells.

Based on these observations, we assumed that in our model, not only the microglial network in the retina but also the neuronal compartment may be affected. Surprisingly, the GCL seems to be able to compensate damaging mechanisms associated with neuronal calcium in our model. Repeated neuronal calcium imaging, using a FRET-based calcium indicator genetically expressed under the Thy1 promoter in CerTN L15 mice (37), showed rather low and only transient dysfunctional calcium signaling in these neurons. In the inflamed brain, the highly dynamic peripheral immune inflammation and gliosis lead to neuronal dysfunction (34, 38), neuronal damage, and finally to neuronal death already at early stages of the disease. In contrast, the inflamed eye showed massive, slow but directed immune infiltration from the optic nerve head toward the retinal periphery, similar gliosis, but only negligible calcium-associated neuronal dysfunction at onset and peak of EAU. It should be noted that, due to the differential expression of the calcium sensor in our model, not all neuronal cells were visible, particularly rods and cones. A delayed effect of the inflammation on the calcium signaling of the retinal ganglion cells cannot be excluded. Repeated retinal intravital imaging experiments during the chronic phase of the disease will shed light on a possible accumulation of calcium-associated neuronal stress leading to late neuronal damage.

Moreover, the extent of neuronal damage to inner CNS compartments in our model, the EAU, is unclear. Similarly, reversible or irreversible effects of pathogenic $CD4^+$ T cells, phagocytes (macrophages and activated microglia) and activated astrocytes on the neuronal function of the retina, in EAE, have not been investigated yet and are also unclear. If the latter is confirmed, the novel technology presented here will make non-invasive monitoring over time of treatment effects in chronic neuroinflammation and therapeutic tracing on single cell level in one individual possible. On the one hand, this will lead to a better understanding of relevant patho-mechanisms and, on the other hand, to a dramatic reduction of experimental animals.

The newly developed retinal imaging approach presented here promises to yield new insights not only into neuroinflammatory but also into neurodegenerative mechanisms. Retinal pathology has recently been intensively discussed in the context of Alzheimer disease, Parkinson disease, and amyotrophic lateral sclerosis (39, 40). Furthermore, unprecedented breakthroughs are possible in the context of pathologies such as genetic vasculature diseases and diabetes type I (41, 42), which are associated with changes of the retinal vasculature, including main blood vessels and capillaries. In terms of elucidation of immune responses, the combination of our approach with genetic EAU models (11), in which tertiary lymphoid organs have been detected within the retina, will allow monitoring of lymphocytic maturation over the whole duration of the immune reaction.

MATERIALS AND METHODS

Two-Photon Laser-Scanning Microscopy (TPLSM)

Multiphoton fluorescence imaging experiments were performed using a specialized laser-scanning microscope based on a commercial scan head (TriMScope II, LaVision BioTec, Bielefeld, Germany). The detection of the fluorescence signals was accomplished with photomultiplier tubes in the ranges of 466 ± 20, 525 ± 25, and 593 ± 20 nm. Cerulean was excited at 850 nm and detected at 466 ± 30 nm simultaneously with citrine emission at 525 ± 25 and 593 ± 20 nm. Blood vessels were labeled with sulforhodamine 101 (excited at 900 nm and detected at 593 ± 20 nm) or FITC dextrane (excited at 800 nm and detected at 525 ± 25 nm). EGFP labeled microglia were excited at 900 nm and detected at 525 ± 50 nm. eYFP labeled $CD4^+$ T cells were excited at 900 or 960 nm and detected at 525 ± 20 nm. tdRFP labeled $LysM^+$ cells were excited at 1,100 nm and detected at 593 ± 20 nm. In all imaging experiments, an average maximum laser power of 50 mW was used to avoid photodamage. The acquisition time for an image with a field of view of 1,400 μm × 1,400 μm and a digital resolution of 994 pixel × 994 pixel was 1.6 s. To observe cell movement in different retinal layers, we acquired 300 μm large *z*-stacks each minute over a total time course of 20 min. Longer imaging sessions are possible with our setup; however, we limited the imaging time window to 20 min to avoid possible side effects due to mechanical stress or long-term laser damage on the retina.

Data Analysis

As previously described, we defined the area of neuronal dysfunction as the area of free neuronal calcium exceeding a concentration of 1 μM. The neuronal calcium concentration was measured *in vivo* in mice expressing the FRET-based calcium biosensor TN L15 in $Thy1^+$ cells. The FRET efficiency, which directly correlates with the intracellular calcium concentration, was measured ratiometrically as previously described by us (27). Briefly, the intensity I of the three acquisition channels 466, 525, and 593 were background corrected I_B, smoothed with a Gaussian filter and corrected for spectral sensitivity η of the photomultiplier tubes. The 525 and 593 channels were additionally corrected for

the spectral overlap α originating from Cerulean. The relative acceptor FRET signal FRET acceptor was calculated as follows:

$$\mathrm{FRET}_{\mathrm{acceptor}} = \frac{I_{\mathrm{YFP}}}{I_{\mathrm{YFP}} + I_{\mathrm{CFP}}} = \frac{\frac{\alpha_{525}}{\eta_{525}} \cdot \left(I_{525} - I_{\mathrm{B},525}\right) + \frac{\alpha_{593}}{\eta_{593}} \cdot \left(I_{593} - I_{\mathrm{B},593}\right)}{\frac{\alpha_{525}}{\eta_{525}} \cdot \left(I_{525} - I_{\mathrm{B},525}\right) + \frac{\alpha_{593}}{\eta_{593}} \cdot \left(I_{593} - I_{\mathrm{B},593}\right) + \frac{\alpha_{466}}{\eta_{466}} \cdot \left(I_{466} - I_{\mathrm{B},466}\right)}$$

Image segmentation and tracking of all cells were performed using existing segmentation, object-recognition and tracking plugins in FIJI, ImageJ. Statistical analysis of the data was performed using Graph Pad Prism.

Mice

All mice used were on a C57/Bl6 background. The *CerTN L15* × *LysM tdRFP* mouse expresses a FRET-based calcium biosensor consisting of Cerulean (donor) and Citrine (acceptor) bound to troponin C, a calcium-sensitive protein present in certain subsets of neurons. Additionally, tdRFP was expressed in LysM$^+$ cells. The $CX_3CR_1^{+/-}$ *EGFP* mouse was used to detect microglia and CD4$^+$ eYFP mouse was used to detect effector T cells.

EAU Induction

Experimental autoimmune uveoretinitis was induced as previously described. Briefly, mice were immunized subcutaneously with 200–300 μg of IRBP$_{1-20}$ (AnaSpec, Belgium) emulsified in CFA (BD Difco, Germany) and were administered 200 ng pertussis toxin (List Biological Laboratories, Inc.) intraperitoneally at the time of immunization and 48 h later. Intravital multiphoton microscopy was performed at different stages of the disease, i.e., pre-onset, onset and peak (days 7, 11, 14, 21, and 28). According to the grading system of Xu et al. (23), we performed clinical scoring for lesions and infiltration in the optic disc, retinal vessels, and retinal tissue for both eyes (days 7, 14, 21, and 28).

Surgical Preparation for Longitudinal Intravital Imaging

Animal experiments were approved by the appropriate state committees for animal welfare (G0093/15, LAGeSo—Landesamt für Gesundheit und Soziales) and were performed in accordance with current applicable guidelines and regulations. All TPLSM experiments were performed under deep isoflurane (1.5%) breathing anesthesia. Before each imaging session the pupil were widened with a drop of sterile eye drop solution (mixture of 2% phenylephrine and 0.4% tropicamide). The mounting of the mice to the positioning system and alignment of the retinas relative to the objective lens were performed in less than 10 min for each mouse, so that the required total anesthesia time was less than 30 min. A drop of sterile transparent eye salve (Vidisic, Bausch&Lomb) between cornea and objective lens were used to prevent eye dehydration. In some mice, the blood vessels were labeled by i.v. injection of 50 μl solution FITC dextrane or sulforhodamine 101.

HE Histology

Eyes were harvested at day 28 after immunization, fixed in 4% paraformaldehyde, embedded in optimal cutting tissue, and frozen with liquid nitrogen. The 10-μm thick retinal cross sections were stained with standard hematoxylin and eosin. The severity of EAU was evaluated by a blinded operator based on the number and size of lesions and infiltrates. Nine mice were included in the histological examination.

Retinal Flat Mounts

Whole retinas were surgically isolated from explanted, unfixed eyes as described previously (18), flattened on a glass slide, covered by medium, and finally sealed with a cover slip. For vasculature labeling, mice received an i.v. injection with labeled dextrane prior to sacrifice.

Immunofluorescence

Cryosections were prepared for immunofluorescence staining as follows: sections were rehydrated in PBS and blocked with PBS containing 1% BSA, 1% Tween, and 10% FCS. Six retina cross sections per eye were used for each staining. Astrocytes were investigated with an Alexa 488 conjugated GFAP antibody. Activated microglia and macrophages were stained with Iba1 as the primary antibody followed by Alexa 647 as the secondary antibody. Cell nuclei were stained with DAPI. Between each staining step sections were washed with PBS solution containing 1% BSA and 1% Tween. Sections were embedded with DAKO fluorescent mounting medium.

Fundoscopy

All fundoscopy experiments were performed directly before the TPLSM experiments under deep isoflurane (1.5%) breathing anesthesia. Pupils were dilated and kept moist as described above. Fundus images were acquired under a circular illuminated bright-field ocular equipped with a reflex camera (EOS600D Canon). To compensate the refractive power of the cornea air interface a thin cover slide was placed in front of the cornea. Fundus images were taken for both eyes in less than 5 min.

ETHICS STATEMENT

Landesamt fuer Gesundheit und Soziales, Berlin, Germany. Animal experiment license G0093/15.

AUTHOR CONTRIBUTIONS

DB, HR, AH and RN designed and performed the research, analyzed the data, and wrote the manuscript. RN, HR, AB, FP, and AH initiated, organized, and supervised the project. HR and AH provided expertise in mouse handling and intravital imaging and performed EAE experiments (G0093/15). FP, RG, RL, RM, HZ, and AB performed experiments. RN, DB, JH, and VA developed the setup for longitudinal retinal time-lapse imaging.

ACKNOWLEDGMENTS

The authors thank O. Griesbeck for providing the *CerTN L15* transgenic mice, H. J. Fehling for the *Rosa26.tdRFP* transgenic mice, and K. Westendorf for the CD4+ eYFP reporter mice. The authors thank P. Mex and P. Matylewski for excellent technical assistance. VA (LaVision Biotec) and JH (Luigs & Neumann) declare competing financial interests. The multiimmersion objective lens will be commercialized by LaVision Biotec, Bielefeld, Germany and the positioning system for retina imaging will be commercialized by Luigs & Neumann, Rattingen.

FUNDING

The authors acknowledge the BMWE under ZIM-grant RETI-IM to AB, VA, JH, and RN and the Deutsche Forschungsgemeinschaft under grant TRR130 to RN, HR, and AH and FOR2165/1 to RN and AH for financial support. This work was partially funded through the excellence cluster NeuroCure (DFG) to FP and AH under grant EXC 257.

SUPPLEMENTARY MATERIAL

The Supplementary Material for this article can be found online at http://journal.frontiersin.org/article/10.3389/fimmu.2016.00642/full#supplementary-material.

FIGURE S1 | **Characterization of disease symptoms in the experimental autoimmune uveoretinitis**. **(A)** Fundoscopy of C57/Bl6-J mice healthy or affected by EAU induced by immunization with IRBP peptide (1–20) reveals differences in health and different phases of the disease. **(B)** Clinical score in EAU assessed by fundoscopy (n = 10 mice encompassing, three EAU experiments). The error bars represent SD. **(C)** HE histology analysis of the retina in healthy mice and mice affected by EAU, 28 days after immunization shows dramatic immune infiltration all through the retinal layers and in the vitreous body as well as disorganized, wave-shaped retinal layers. Scale bar = 200 μm. **(D)** Immunofluorescence analysis of retina in health and in EAU shows an increase of Iba1 signal indicative for microglial activation towards a phagocytic phenotype and disorganization of the GFAP (astrocytic) structures as well as enhancement within the GCL. Scale bar = 200 μm. The retinal layer abbreviations: RPE, retinal pigment epithelium; RC, layer of rods and cones; ONL, outer nuclear layer; OPL, outer plexiform layer; INL, inner nuclear layer; IPL, inner plexiform layer; GCL, ganglion cell layer.

FIGURE S2 | **Mouse surgery and handling for repeated intravital imaging of the retina do not induce inflammation or evident neuronal retina damage (A) 3D fluorescence images of the retina of a healthy $CX_3CR_1^{+/-}$ EGFP mouse acquired at days 21, 25, 28, 35, and 42 after gluing the positioning cap on the skull**. The time points correspond to days 7, 11, 14, 21, and 28 after immunization in EAU experiments, since the immunization is always performed 2 weeks (14 days after gluing the positioning cap). **(B)** 3D fluorescence images of the retina of a healthy CD4.eYFP mouse acquired at days 21, 25, 28, 35, and 42 after gluing the positioning cap on the skull. Scale bar = 200 μm. **(C)** Results of time-lapse imaging (20 min) of the FRET signal within the retina of a healthy CerTN L15 × LysM tdRFP mouse showing no changes in the neuronal calcium after five consecutive imaging sessions (days 21, 25, 28, 35, and 42 after gluing the positioning cap on the skull). **(D)** 3D fluorescence image within the same mouse at day 42 (after the last imaging session) shows intact neuronal processes and somata as well as no signs of infiltration with LysM tdRFP cells (mostly phagocytes). Scale bar = 200 μm.

FIGURE S3 | **TN L15 construct is expressed in the ganglion cells (GCL), in the retina of CerTN L15 mice**. Fluorescence image of the native, fixed retina (transversal section) of a healthy CerTN L15 mouse shows only in the GCL-specific citrine fluorescence (green). The other retinal layers as well as the eye lens are visible due to their autofluorescence (blue). Scale bar = 200 μm.

VIDEO S1 | ***In vivo* two-photon imaging of the vasculature of the mouse retina**. The 1,000 μm × 1,000 μm fluorescence images series of retinal blood vessels labeled by FITC dextrane acquired at tissue depths between 0 μm (retina surface) and 300 μm. z-step = 6 μm. The main blood vessels (veins and arteries) meet in the optic nerve head (ON head).

VIDEO S2 | **Longitudinal time-lapse intravital imaging of the retina of a CD4 EYFP mouse affected by experimental autoimmune uveoretinitis (EAU) 21 days after immunization with irpb peptide 1–20 (peak of disease)**. Three-dimensional 1,400 μm × 1,400 μm × 300 μm fluorescence images were acquired every minute, over 20 min in the retina of CD4 eYFP mice affected by EAU, at day 21. The CD4 T cells are depicted in green, whereas the autofluorescence of retinol especially from the retinal pigment epithelium is depicted in blue. z-step = 6 μm.

VIDEO S3 | **Longitudinal time-lapse intravital imaging of the retina of the same CD4 EYFP mouse affected by experimental autoimmune uveoretinitis (EAU) as in Video S2 in Supplementary Material, 28 days after immunization (peak of disease)**. Three-dimensional 1,400 μm × 1,400 μm × 300 μm fluorescence images were acquired every minute, over 20 min in the retina of CD4 eYFP mice affected by EAU, at day 28. The CD4 T cells are depicted in green, whereas the autofluorescence of the retinal pigment epithelium is depicted in blue. z-step = 6 μm.

VIDEO S4 | **Longitudinal time-lapse intravital imaging of the retina of a LYSM.TDRFP mouse affected by experimental autoimmune uveoretinitis (EAU), 21 days after immunization (peak of disease)**. Three-dimensional 1,400 μm × 1,400 μm × 300 μm fluorescence images were acquired every minute, over 20 min in the retina of LysM.tdRFP mice affected by EAU, at day 21. The LysM cells are depicted in red, whereas the autofluorescence of the retinal pigment epithelium is depicted in blue. z-step = 6 μm.

VIDEO S5 | **Longitudinal time-lapse intravital imaging of the retina of the same LYSM.TDRFP mouse affected by experimental autoimmune uveoretinitis (EAU), 28 days after immunization (peak of disease)**. Three-dimensional 1,400 μm × 1,400 μm × 300 μm fluorescence images were acquired every minute, over 20 min in the retina of LysM.tdRFP mice affected by EAU, at day 28. The LysM cells are depicted in red, whereas the autofluorescence of the retinal pigment epithelium is depicted in blue. z-step = 6 μm.

VIDEO S6 | **Longitudinal time-lapse intravital imaging of the retina of a $CX_3CR_1^{+/-}$ EGFP mouse affected by experimental autoimmune uveoretinitis (EAU) at day 7 after immunization with interphotoreceptor retinoid-binding protein PEPTIDE 1–20 (pre-onset of disease)**. Three-dimensional 1,400 μm × 1,400 μm × 300 μm fluorescence images were acquired every minute, over 20 min in the retina of $CX_3CR_1^{+/-}$ EGFP mice affected by EAU, at day 7, 11, 14, 21, and 28 after immunization. The $CX_3CR_1^{+/-}$ EGFP cells, microglia and macrophages, are depicted in green, whereas the vasculature labeled by rhodamine is depicted in red. z-step = 6 μm. The sessile cells with a high number of processes are resting microglia. Activated microglia and peripheral macrophages adopt an amoeboid morphology indicative for their shift towards an activated phenotype.

VIDEO S7 | **Longitudinal time-lapse intravital imaging of the retina of the same $CX_3CR_1^{+/-}$ EGFP mouse affected bY experimental autoimmune uveoretinitis (EAU) as in Video S4 in Supplementary Material, at day 14 after immunization (onset of disease)**. Three-dimensional 1,400 μm × 1,400 μm × 300 μm fluorescence images were acquired every minute, over 20 min in the retina of $CX_3CR_1^{+/-}$ EGFP mice affected by EAU. The $CX_3CR_1^{+/-}$ EGFP cells, microglia and macrophages, are depicted in green, whereas the vasculature labeled by rhodamine is depicted in red. z-step = 6 μm.

VIDEO S8 | **Longitudinal time-lapse intravital imaging of the retina of the same $CX_3CR_1^{+/-}$ EGFP mouse affected bY experimental autoimmune uveoretinitis (EAU) as in Videos S4 and S5 in Supplementary Material, at day 21 after immunization (peak of disease)**. Three-dimensional 1,400 μm × 1,400 μm × 300 μm fluorescence images were acquired every

minute, over 20 min in the retina of $CX_3CR_1^{+/-}$ EGFP mice affected by EAU. The $CX_3CR_1^{+/-}$ EGFP cells, microglia and macrophages, are depicted in green, whereas the vasculature labeled by rhodamine is depicted in red. *z*-step = 6 μm.

VIDEO S9 | Longitudinal time-lapse intravital imaging of the retina of the same $CX_3CR_1^{+/-}$ EGFP mouse affected by experimental autoimmune uveoretinitis (EAU) as in Videos S4–S6 in Supplementary Material, at day 28 after immunization (peak of disease). Three-dimensional 1,400 μm × 1,400 μm × 300 μm fluorescence images were acquired every minute, over 20 min in the retina of $CX_3CR_1^{+/-}$ EGFP mice affected by EAU. The $CX_3CR_1^{+/-}$ EGFP cells, microglia, and macrophages, are depicted in green, whereas the vasculature labeled by rhodamine is depicted in red. *z*-step = 6 μm.

VIDEO S10 | Time-lapse intravital imaging of the retina of a healthy CERTN L15 mouse reveals neuronal calcium and, hence, neuronal function is not disturbed by the laser beam during multiphoton microscopy. Three-dimensional 1,400 μm × 1,400 μm × 300 μm FRET ratio images were acquired every minute, over 20 min in the retina of healthy CerTN L15 mice. In this mouse strain, some neuronal subsets express the TN L15 genetically encoded Ca^{2+} biosensor. The TN L15 biosensor is a FRET-biosensor based on Troponin C, a calcium-sensitive protein. The FRET pair contains Cerulean (cyan fluorescence) as donor and Citrine (yellow fluorescence) as acceptor. We used a three channel-based ratiometric FRET evaluation method to calculate the FRET ratio in the neurons and to evaluate the sustained neuronal calcium concentration. *z*-step = 6 μm.

VIDEO S11 | Time-lapse intravital imaging of the retina of a CERTN L15 mouse affected by experimental autoimmune uveoretinitis (EAU), 21 days after immunization with interphotoreceptor retinoid-binding protein peptide 1–20 (peak of disease). Three-dimensional 1,400 μm × 1,400 μm × 300 μm FRET ratio images were acquired every minute, over 20 min in the retina of CerTN L15 mice affected by EAU at days 7, 11, 14, 21, and 28 after immunization. *z*-step = 6 μm.

VIDEO S12 | Time-lapse intravital imaging of the retina of the same CERTN L15 mouse affected by experimental autoimmune uveoretinitis (EAU) as in Video S9 in Supplementary Material, at day 28 after immunization (peak of disease). Three-dimensional 1,400 μm × 1,400 μm × 300 μm FRET ratio images were acquired every minute, over 20 min in the retina of CerTN L15 mice affected by EAU. z-step = 6 μm.

REFERENCES

1. Chen L, Gordon LK. Ocular manifestations of multiple sclerosis. *Curr Opin Ophthalmol* (2005) 16:315–20. doi:10.1097/01.icu.0000179804.49842.e2
2. Pérez-Rico C, Ayuso-Peralta L, Rubio-Pérez L, Roldán-Díaz I, Arévalo-Serrano J, Jiménez-Jurado D, et al. Evaluation of visual structural and functional factors that predict the development of multiple sclerosis in clinically isolated syndrome patients. *Invest Ophthalmol Vis Sci* (2014) 55:6127–31. doi:10.1167/iovs.14-14807
3. Sinnecker T, Oberwahrenbrock T, Metz I, Zimmermann H, Pfueller CF, Harms L, et al. Optic radiation damage in multiple sclerosis is associated with visual dysfunction and retinal thinning – an ultrahigh-field MR pilot study. *Eur Radiol* (2015) 25:122–31. doi:10.1007/s00330-014-3358-8
4. Jarius S, Wildemann B, Paul F. Neuromyelitis optica: clinical features, immunopathogenesis and treatment. *Clin Exp Immunol* (2014) 176(2):149–64. doi:10.1111/cei.12271
5. Schneider E, Zimmermann H, Oberwahrenbrock T, Kaufhold F, Kadas EM, Petzold A, et al. Optical coherence tomography reveals distinct patterns of retinal damage in neuromyelitis optica and multiple sclerosis. *PLoS One* (2013) 8:e66151. doi:10.1371/journal.pone.0066151
6. Metz I, Beißbarth T, Ellenberger D, Pache F, Stork L, Ringelstein M, et al. Serum peptide reactivities may distinguish neuromyelitis optica subgroups and multiple sclerosis. *Neurol Neuroimmunol Neuroinflamm* (2016) 3(2):e204. doi:10.1212/NXI.0000000000000204
7. Bock M, Brandt AU, Kuchenbecker J, Dörr J, Pfueller CF, Weinges-Evers N, et al. Impairment of contrast visual acuity as a functional correlate of retinal nerve fibre layer thinning and total macular volume reduction in multiple sclerosis. *Br J Ophtalmol* (2012) 96(1):62–7. doi:10.1136/bjo.2010.193581
8. Bennett JL, de Seze J, Lana-Peixoto M, Palace J, Waldman A, Schippling S, et al. Neuromyelitis optica and multiple sclerosis: seeing differences through optical coherence tomography. *Mult Scler* (2015) 21:678–88. doi:10.1177/1352458514567216
9. Caspi RR. Experimental autoimmune uveoretinitis in the rat and mouse. *Curr Protoc Immunol* (2003) Chapter 15:Unit 15.16. doi:10.1002/0471142735.im1506s53
10. Chen X, Kezic JM, Forrester JV, Goldberg GL, Wicks IP, Bernard CC, et al. In vivo multi-modal imaging of experimental autoimmune uveoretinitis in transgenic reporter mice reveals the dynamic nature of inflammatory changes during disease progression. *J Neuroinflammation* (2015) 12:17. doi:10.1186/s12974-015-0235-6
11. Kielczewski JL, Horai R, Jittayasothorn Y, Chan CC, Caspi RR. Tertiary lymphoid tissue forms in retinas of mice with spontaneous autoimmune uveitis and has consequences on visual function. *J Immunol* (2016) 196:1013–25. doi:10.4049/jimmunol.1501570
12. Borghuis BG, Marvin JS, Looger LL, Demb JB. Two-photon imaging of nonlinear glutamate release dynamics at bipolar cell synapses in the mouse retina. *J Neurosci* (2013) 33:10972–85. doi:10.1523/JNEUROSCI.1241-13.2013
13. He S, Ye C, Sun Q, Leung CK, Qu JY. Label-free nonlinear optical imaging of mouse retina. *Biomed Opt Express* (2015) 6:1055–66. doi:10.1364/BOE.6.001055
14. Newkirk GS, Hoon M, Wong RO, Detwiler PB. Response properties of a newly identified tristratified narrow field amacrine cell in the mouse retina. *PLoS One* (2015) 10:e0137702. doi:10.1371/journal.pone.0137702
15. Maeda A, Palczewska G, Golczak M, Kohno H, Dong Z, Maeda T, et al. Two-photon microscopy reveals early rod photoreceptor cell damage in light-exposed mutant mice. *Proc Natl Acad Sci U S A* (2014) 111:E1428–37. doi:10.1073/pnas.1317986111
16. Palczewska G, Dong Z, Golczak M, Hunter JJ, Williams DR, Alexander NS, et al. Noninvasive two-photon microscopy imaging of mouse retina and retinal pigment epithelium through the pupil of the eye. *Nat Med* (2014) 20:785–9. doi:10.1038/nm.3590
17. Sharma R, Yin L, Geng Y, Merigan WH, Palczewska G, Palczewski K, et al. In vivo two-photon imaging of the mouse retina. *Biomed Opt Express* (2013) 4:1285–93. doi:10.1364/BOE.4.001285
18. Stremplewski P, Komar K, Palczewski K, Wojtkowski M, Palczewska G. Periscope for noninvasive two-photon imaging of murine retina in vivo. *Biomed Opt Express* (2015) 6:3352–61. doi:10.1364/BOE.6.003352
19. Chen J, Qian H, Horai R, Chan CC, Caspi RR. Use of optical coherence tomography and electroretinography to evaluate retinal pathology in a mouse model of autoimmune uveitis. *PLoS One* (2013) 8:e63904. doi:10.1371/journal.pone.0063904
20. Chu CJ, Herrmann P, Carvalho LS, Liyanage SE, Bainbridge JW, Ali RR, et al. Assessment and in vivo scoring of murine experimental autoimmune uveoretinitis using optical coherence tomography. *PLoS One* (2013) 8:e63002. doi:10.1371/journal.pone.0063002
21. Gadjanski I, Williams SK, Hein K, Sättler MB, Bähr M, Diem R. Correlation of optical coherence tomography with clinical and histopathological findings in experimental autoimmune uveoretinitis. *Exp Eye Res* (2011) 93:82–90. doi:10.1016/j.exer.2011.04.012
22. Siffrin V, Radbruch H, Glumm R, Niesner R, Paterka M, Herz J, et al. In vivo imaging of partially reversible th17 cell-induced neuronal dysfunction in the course of encephalomyelitis. *Immunity* (2010) 33:424–36. doi:10.1016/j.immuni.2010.08.018
23. Xu H, Koch P, Chen M, Lau A, Reid DM, Forrester JV. A clinical grading system for retinal inflammation in the chronic model of experimental autoimmune uveoretinitis using digital fundus images. *Exp Eye Res* (2008) 87:319–26. doi:10.1016/j.exer.2008.06.012
24. Mossakowski AA, Pohlan J, Bremer D, Lindquist R, Millward JM, Bock M, et al. Tracking CNS and systemic sources of oxidative stress during the course of chronic neuroinflammation. *Acta Neuropathol* (2015) 130:799–814. doi:10.1007/s00401-015-1497-x
25. Schmucker C, Schaeffel F. A paraxial schematic eye model for the growing C57BL/6 mouse. *Vision Res* (2004) 44:1857–67. doi:10.1016/j.visres.2004.03.011

26. Siffrin V, Brandt AU, Radbruch H, Herz J, Boldakowa N, Leuenberger T, et al. Differential immune cell dynamics in the CNS cause CD4+ T cell compartmentalization. *Brain* (2009) 132:1247–58. doi:10.1093/brain/awn354
27. Rinnenthal JL, Börnchen C, Radbruch H, Andresen V, Mossakowski A, Siffrin V, et al. Parallelized TCSPC for dynamic intravital fluorescence lifetime imaging: quantifying neuronal dysfunction in neuroinflammation. *PLoS One* (2013) 8:e60100. doi:10.1371/journal.pone.0060100
28. Thyagarajan S, van Wyk M, Lehmann K, Löwel S, Feng G, Wässle H. Visual function in mice with photoreceptor degeneration and transgenic expression of channelrhodopsin 2 in ganglion cells. *J Neurosci* (2010) 30:8745–58. doi:10.1523/JNEUROSCI.4417-09.2010
29. Brandt AU, Oberwahrenbrock T, Ringelstein M, Young KL, Tiede M, Hartung HP, et al. Primary retinal pathology in multiple sclerosis as detected by optical coherence tomography. *Brain* (2011) 134:e193; author reply e194. doi:10.1093/brain/awr095
30. Friedl P, Weigelin B. Interstitial leukocyte migration and immune function. *Nat Immunol* (2008) 9:960–9. doi:10.1038/ni.f.212
31. Friedl P, Gilmour D. Collective cell migration in morphogenesis, regeneration and cancer. *Nat Rev Mol Cell Biol* (2009) 10:445–57. doi:10.1038/nrm2720
32. Matheu MP, Othy S, Greenberg ML, Dong TX, Schuijs M, Deswarte K, et al. Imaging regulatory T cell dynamics and CTLA4- mediated suppression of T cell priming. *Nat Commun* (2015) 6:6219. doi:10.1038/ncomms7219
33. Herz J, Paterka M, Niesner RA, Brandt AU, Siffrin V, Leuenberger T, et al. In vivo imaging of lymphocytes in the CNS reveals different behaviour of naive T cells in health and autoimmunity. *J Neuroinflammation* (2011) 8:131. doi:10.1186/1742-2094-8-131
34. Radbruch H, Bremer D, Guenther R, Cseresnyes Z, Lindquist R, Hauser AE, et al. Ongoing oxidative stress causes subclinical neuronal dysfunction in the recovery phase of EAE. *Front Immunol* (2016) 7:92. doi:10.3389/fimmu.2016.00092
35. Nikić I, Merkler D, Sorbara C, Brinkoetter M, Kreutzfeldt M, Bareyre FM, et al. A reversible form of axon damage in experimental autoimmune encephalomyelitis and multiple sclerosis. *Nat Med* (2011) 17:495–9. doi:10.1038/nm.2324
36. Bayerl SH, Niesner R, Cseresnyes Z, Radbruch H, Pohlan J, Brandenburg S, et al. Time lapse in vivo microscopy reveals distinct dynamics of microglia-tumor environment interactions – a new role for the tumor perivascular space as highway for trafficking microglia. *Glia* (2016) 64:1210–26. doi:10.1002/glia.22994
37. Heim N, Garaschuk O, Friedrich MW, Mank M, Milos RI, Kovalchuk Y, et al. Improved calcium imaging in transgenic mice expressing a troponin C-based biosensor. *Nat Methods* (2007) 4:127–9. doi:10.1038/nmeth1009
38. Breckwoldt MO, Pfister FM, Bradley PM, Marinković P, Williams PR, Brill MS, et al. Multiparametric optical analysis of mitochondrial redox signals during neuronal physiology and pathology in vivo. *Nat Med* (2014) 20:555–60. doi:10.1038/nm.3520
39. Madeira MH, Ambrosio AF, Santiago AR. Glia-mediated retinal neuroinflammation as a biomarker in Alzheimer's disease. *Ophthalmic Res* (2015) 54:204–11. doi:10.1159/000440887
40. Roth NM, Saidha S, Zimmermann H, Brandt AU, Oberwahrenbrock T, Maragakis NJ, et al. Optical coherence tomography does not support optic nerve involvement in amyotrophic lateral sclerosis. *Eur J Neurol* (2013) 20(8):1170–6. doi:10.1111/ene.12146
41. Sohn EH, van Dijk HW, Jiao C, Kok PH, Jeong W, Demirkaya N, et al. Retinal neurodegeneration may precede microvascular changes characteristic of diabetic retinopathy in diabetes mellitus. *Proc Natl Acad Sci U S A* (2016) 113:E2655–64. doi:10.1073/pnas.1522014113
42. Albrecht P, Blasberg C, Lukas S, Ringelstein M, Müller AK, Harmel J, et al. Retinal pathology in idiopathic moyamoya angiopathy detected by optical coherence tomography. *Neurology* (2015) 85(6):521–7. doi:10.1212/WNL.0000000000001832

Conflict of Interest Statement: VA (LaVision Biotec) and JH (Luigs & Neumann) declare competing financial interests. The water-immersion objective lens will be commercialized by LaVision Biotec, Bielefeld, Germany and the positioning system for retina imaging will be commercialized by Luigs & Neumann, Rattingen. The remaining authors declare that the research was conducted in the absence of any commercial or financial relationships that could be construed as a potential conflict of interest.

Copyright © 2016 Bremer, Pache, Günther, Hornow, Andresen, Leben, Mothes, Zimmermann, Brandt, Paul, Hauser, Radbruch and Niesner. This is an open-access article distributed under the terms of the Creative Commons Attribution License (CC BY). The use, distribution or reproduction in other forums is permitted, provided the original author(s) or licensor are credited and that the original publication in this journal is cited, in accordance with accepted academic practice. No use, distribution or reproduction is permitted which does not comply with these terms.

4 Lebenslauf

Mein Lebenslauf wird aus datenschutzrechtlichen Gründen in der elektronischen Version meiner Arbeit nicht veröffentlicht.

5 Komplette Publikationsliste

Intravital FRET: Probing Cellular and Tissue Function *in Vivo*

Helena Radbruch, **Daniel Bremer**, Ronja Mothes, Robert Günther, Jan Leo Rinnenthal, Julian Pohlan, Carolin Ulbricht, Anja E. Hauser, Raluca Niesner

International Journal of Molecular Sciences, 2015

Tracking CNS and systemic sources of oxidative stress during the course of chronic neuroinflammation

Agata A. Mossakowski, Julian Pohlan, **Daniel Bremer**, Randall Lindquist, Jason M. Millward, Markus Bock, Karolin Pollok, Ronja Mothes, Leonard Viohl, Moritz Radbruch, Jenny Gerhard, Judith Bellmann-Strobl, Janina Behrens, Carmen Infante-Duarte, Anja Mähler, Michael Boschmann, Jan Leo Rinnenthal, Martina Füchtemeier, Josephine Herz, Florence C. Pache, Markus Bardua, Josef Priller, Anja E. Hauser, Friedemann Paul, Raluca Niesner, Helena Radbruch

Acta Neuropathologica, 2015

Ongoing Oxidative Stress Causes Subclinical Neuronal Dysfunction in the Recovery Phase of EAE

Helena Radbruch, **Daniel Bremer**, Robert Guenther, Zoltan Cseresnyes, Randall Lindquist, Anja E. Hauser, Raluca Niesner

Frontiers in Immunology, 2016

Longitudinal Intravital Imaging of the Retina Reveals Long-term Dynamics of Immune Infiltration and Its Effects in the Glial Network in Experimental Autoimmune Uveoretinitis, without Evident Signs of Neuronal Dysfunction in the Ganglion Cell Layer

Daniel Bremer, Florence Pache, Robert Günther, Jürgen Hornow, Volker Andresen, Ruth Leben, Ronja Mothes, Hanna Zimmermann, Alexander U. Brandt, Friedemann Paul, Anja E. Hauser, Helena Radbruch and Raluca Niesner

Frontiers in Immunology, 2016

Method to Detect the Cellular Source of Over-Activated NADPH Oxidases Using NAD(P)H Fluorescence Lifetime Imaging

Daniel Bremer, Ruth Leben, Ronja Mothes, Helena Radbruch, Raluca Niesner

Current Protocols in Cytometry, 2017

Analyzing NADPH-oxidase dependent oxidative distress in aging and vascular amyloid pathology

Helena Radbruch, Ronja Mothes, **Daniel Bremer**, Stefanie Seifert, Ralf Köhler, Julian Pohlan, Lennard Ostendorf, Robert Guenther, Ruth Leben, Werner Stenzel, Raluca Aura Niesner, Anja Erika Hauser

Frontiers in Immunology, 2017

6 Danksagung

An dieser Stelle möchte ich allen danken, die an der Entstehung meiner Doktorarbeit beteiligt waren. In erster Linie möchte ich mich bei Hanna Zimmermann bedanken, die mich auf die freie Stelle im RETI-IM-Projekt aufmerksam gemacht hat. Dadurch konnten wir nicht nur im Studium, sondern auch während unserer Promotion weiterhin zusammenarbeiten.

Besonderer Dank gilt natürlich meinen trimagischen Chefinnen Raluca Niesner, Anja E. Hauser und Helena Radbruch für die tolle Betreuung, für die anregenden Diskussionen und wegweisenden Visionen in Bezug auf einzelne Fragestellungen und Probleme. Auf euch konnte man sich immer verlassen und ihr standet trotz vollem Terminkalender immer mit Rat und Tat zur Seite.

Bei Ronja Mothes möchte ich mich für die tolle Zusammenarbeit bei den zahlreichen FLIM-Messungen bis spät in die Nacht und die lustigen Gespräche beim Feierabendbier bedanken. Ganz herzlich möchte ich mich bei Robert Günther bedanken, mit dem ich den Umgang mit den Mäusen vertieft erlernen konnte und ohne dem das RETI-IM-Projekt nicht so ein Erfolg geworden wäre.

Dann möchte ich natürlich noch allen anderen Mitgliedern unserer quasi-fusionierten AG NieHau danken für die tolle Zeit und die super Arbeitsatmosphäre. Zu erwähnen wären da insbesondere Florence Pache für die gute Zusammenarbeit im RETI-IM-Projekt, Peggy Max für die Unterstützung bei der Zellisolierung, den Färbungen und Schnitten, Ralf Uecker für die Einweisung am LSM und Keyence und für die Hilfe bei den AK-Färbungen, Asylkhan Rakhymzhan für die Einweisung am Zweiphotonenmikroskop und Hilfe bei allen physikalischen und technischen Problemen, bei Zoltan Cseresnyes und Fabian Kriegel für die Hilfestellung beim Programmieren in ImageJ und Imaris.
Und bei meinen Büro-homies David Reismann, Jonathan Stefanowski, Ralf Köhler und Ruth Leben möchte ich mich für die tolle Büroatmosphäre, die lauschigen Abende und die gemeinsamen Aktivitäten ganz herzlich bedanken. Ich wünsche euch noch viel Erfolg bei euren Promotionen!

Zu guter Letzt bedanke ich mich bei meinen Eltern, Geschwistern und bei meiner zukünftigen Ehefrau, auf die ich mich immer verlassen kann und ohne die ich nicht der wäre der ich heute bin.